OXFORD

Journal of Petrology, 2024, **65**, egae087
https://doi.org/10.1093/petrology/egae087
ADVANCE ACCESS PUBLICATION DATE 12 AUGUST 2024
Original Manuscript

Destruction of the Lithosphere beneath the SW Margin of the São Francisco Craton Evidenced by Refertilized and Deformed Mantle Xenoliths

LUISA GOMES BRAGA [1,*], TIAGO JALOWITZKI[1], FERNANDA GERVASONI[2,3], RODRIGO FREITAS RODRIGUES[1,4], MAURIZIO MAZZUCCHELLI[5], TOMMASO GIOVANARDI[5], MARINA MARQUES DALLA COSTA[6], ROBERTO VENTURA SANTOS[1], MARCELO PERES ROCHA[1], REINHARDT ADOLFO FUCK[1], GEORGINA RUBIANO LORENZONI[7] and GUSTAVO WALTER BERTOTTO[7]

[1]Universidade de Brasília, Instituto de Geociências, Programa de Pós-graduação em Geologia, Brasília 70910-900, Brazil
[2]Centro de Engenharias, Universidade Federal de Pelotas, Pelotas 96010-450, Brazil
[3]Programa de Pós-graduação em Geociências, Universidade Federal do Rio Grande do Sul, Porto Alegre 91501-970, Brazil
[4]Research School of Earth Science, Australian National University, Canberra ACT 0200, Australia
[5]Dipartimento di Scienze Chimiche e Geologiche, Universitá di Modena e Reggio Emilia, Modena 41125, Italy
[6]Agência Nacional de Mineração, Brasília 70040-020, Brazil
[7]Instituto de Ciencias de la Tierra y Ambientales de La Pampa, CONICET-Universidad Nacional de La Pampa, Santa Rosa, Argentina

*Corresponding author. Telephone: +55 (65) 98115-9445. E-mail: luisagbraga@gmail.com

The destruction of the cratonic root has been documented for multiple cratons worldwide and is characterized by severe lithospheric thinning, extensive extensional deformation, and intense thermal activity. Here, we present detailed petrography accompanied by comprehensive geochemical and isotopic data for peridotites, pyroxenites, and eclogites from the SW margin of the São Francisco Craton that has also been severely thinned. The diamond-bearing Canastra-1 kimberlite represents a Cretaceous intrusion from the Alto Paranaíba Igneous Province and hosts garnet-bearing mantle xenoliths from different mantle sources, revealing a complex history of metasomatism/refertilization related to superimposed tectonic events since the cratonic consolidation.

Eclogites (T = 978–982°C; P ~ 4.0 GPa) and pargasite-bearing websterites (T = 875–926°C; P = 2.0–3.0 GPa) represent the shallower and colder cratonic lithosphere. Mantle-derived high-MgO eclogitic clinopyroxenes show a light rare earth element (LREE)-enriched pattern ($Ce/Yb_N = 60.90–93.63$) while both clinopyroxene and garnet present high $^{87}Sr/^{86}Sr$ ratios (0.70842–0.70912) and negative ϵNd values (−5.6 to −7.3). These features, supported by the reconstructed whole-rock composition, suggest a mafic protolith probably metasomatized by fluid/melt derived from the overlying sedimentary rocks. Pargasite websterites are cumulates from an evolved (SiO_2-rich) and hydrated basaltic andesitic magma. These xenoliths are characterized by high concentration of LREE relative to heavy-REE (HREE) in clinopyroxene ($Ce/Yb_N = 10.52–50.61$) and pargasite ($Ce/Yb_N = 10.26–57.06$), and by the presence of Al-rich orthopyroxene. As observed in eclogites, clinopyroxene and garnet from pargasite websterites display high $^{87}Sr/^{86}Sr$ ratios (0.70894–0.71094) and strong negative ϵNd values (−7.2 to −13.3). Trace elements (i.e. Zr, Ti, and Y) in garnets of both rock types indicate the role of a depleted component affected by a metasomatic agent. Although we were unable to date the formation of these rocks or the metasomatic events, we suggest a possible relationship with the consolidation of Gondwana during the Neoproterozoic.

Sheared lherzolites, clinopyroxenites, anhydrous websterites, and dunite are deeper fragments from the lithosphere-asthenosphere boundary (LAB: 1191–1290°C; 5.3–5.6 GPa). They have abundant kelyphitic rims around garnet grains, which indicate metasomatism promoted by the percolation of a high-temperature proto-kimberlite melt enriched in Ti, Zr, and Y. The presence of kelyphitic phlogopite with high-Ti-Cr contents reinforces this assumption. LREE-enriched clinopyroxenes ($Ce/Yb_N = 12.06–48.02$) confirm the enriched character of the silicate melt responsible for the refertilization process within the cratonic root. The proto-kimberlite metasomatism is further supported by the preferential enrichment of $^{87}Sr/^{86}Sr$ ratios (0.70560–0.70869) accompanied by positive ϵNd values (+1.8 to +10.10). Two-point clinopyroxene-garnet Sm–Nd isochrons yielded an average age of 120 ± 5 Ma, representing the kimberlite eruption/emplacement age of the host kimberlite. These deeper LAB xenoliths reveal intense lithospheric thinning triggered by percolation of a high-temperature proto-kimberlite melt since the early stages of Gondwana break-up during the Cretaceous, shortly before the kimberlite emplacement at 120 Ma. Therefore, they provide remarkable evidence of the destruction of the São Francisco Craton through thermal-mechanical erosion that triggered its rejuvenation.

Highlights
- Canastra-1 xenoliths show strong lithological, chemical, and isotopic heterogeneity.
- Rejuvenation and decratonization supported by sheared and refertilized lherzolites.
- Extensive lithospheric thinning corroborates the destruction of the São Francisco Craton.
- Lithospheric xenoliths (875–982°C; ~100–130 km) are subduction-related.
- Proto-kimberlite metasomatism affected the deeper LAB xenoliths (1191–1290°C; 174–186 km).

Key words: Mantle metasomatism; Mantle xenoliths; Mineral chemistry; Sr–Nd isotopes

RECEIVED JULY 18, 2023; **REVISED** JUNE 3, 2024; **ACCEPTED** AUGUST 6, 2024

INTRODUCTION

Although most Archean to Paleoproterozoic cratonic nuclei are believed to be tectonically stable, the base of the lithosphere in these terrains may have been reworked by episodic rejuvenation events associated to thermal anomalies promoted by mantle plumes, or even by small-scale convection (edge-driving convection) that generates lateral thermal erosion as a response to the upwelling of the hot asthenosphere (Menzies *et al.*, 1987; Foley, 1992, 2008; King & Anderson, 1998; King & Ritsema, 2000; Aulbach, 2018; Liu *et al.*, 2019, 2021). In addition, recycling of oceanic slabs may also contribute to mantle metasomatism (cryptic and/or modal), re-enriching the lithosphere through the percolation of melts and/or fluids derived from the slab melt or dehydration (Foley, 1992; Konzett *et al.*, 2000; Aulbach *et al.*, 2007). These mechanisms favor a succession of events such as rejuvenation, weakness, and erosion of the deep lithosphere at cratonic margins (Carlson *et al.*, 2004; Downes *et al.*, 2004; Tappe *et al.*, 2007; Foley, 2008; Tang *et al.*, 2013; Giuliani *et al.*, 2016; Liao *et al.*, 2017; Fitzpayne *et al.*, 2018, 2019, 2020; Liu & Li, 2018; Liu *et al.*, 2019; Dessai *et al.*, 2021; Carvalho *et al.*, 2022a).

Several mineralogical, chemical, and isotopic investigations on mantle xenoliths hosted by kimberlites from cratonic regions worldwide have demonstrated lithological and compositional heterogeneity in the upper mantle (Griffin *et al.*, 1999; Konzett *et al.*, 2000, 2013; Grégoire *et al.*, 2002; Carlson *et al.*, 2007; Ionov *et al.*, 2010; Agashev *et al.*, 2013; Aulbach *et al.*, 2013, 2020; Guo *et al.*, 2020; Fernandes *et al.*, 2021; Gervasoni *et al.*, 2022; Rodrigues *et al.*, 2023). Complementary temporal and spatial information provided by geochronological and geophysical studies also supports geochemical heterogeneity studies about the structure and evolution of the cratonic lithosphere (Aulbach, 2018). However, xenoliths from the São Francisco and Amazonian cratons, bearing some the most important Archean nuclei in Brazil, lack detailed geochemical and geophysical investigations. Besides the studies based on mineral xenocrysts (Read *et al.*, 2004; Hunt *et al.*, 2009; Donatti-Filho *et al.*, 2013; Guarino *et al.*, 2013; Coldebella *et al.*, 2020; Carvalho *et al.*, 2022a, 2022b), a few scientific contributions concerning mantle xenoliths have addressed the long-lived tectonic evolution of the lithospheric mantle beneath Brazilian cratons (Carvalho, 1997; Carlson *et al.*, 2007; Costa, 2008; Thomaz, 2009; Nannini, 2011, 2016; Costa, 2012; Almeida *et al.*, 2014, 2022; Fernandes *et al.*, 2021; Gervasoni *et al.*, 2022; Rodrigues *et al.*, 2023).

In this context, we present a comprehensive and detailed study based on petrography, mineral chemistry, and isotope geochemistry of fresh mantle xenoliths hosted by the Canastra-1 kimberlite. These xenoliths, which represent heterogeneous fragments from the cratonic mantle within the garnet stability field, include sheared lherzolites (n = 12), clinopyroxenites (n = 6), websterites (olivine-free anhydrous and hydrated xenoliths, n = 5), eclogites (n = 2), and dunite (n = 1). Here we propose the partial destruction of the SW margin of the São Francisco Craton registered for the first time by samples of the deep cratonic lithosphere. The discussion about this tectonic setting is based on the mineral chemistry mainly of clinopyroxene, garnet, phlogopite, orthopyroxene, and pargasite. Sr–Nd isotopic ratios and Sm–Nd isochrons of whole-rock, clinopyroxene, and garnet support these data.

GEOLOGICAL SETTING

The São Francisco Craton is one of the major cratonic areas of the South American platform, composed of Archean blocks accreted and reworked during Paleoproterozoic and Neoproterozoic orogenies (e.g. Almeida *et al.*, 1981; Ganade *et al.*, 2021; Neves, 2021). This craton, together with the Amazonian Craton and the Paranapanema Block, limit the Tocantins Province, the latter being entirely covered by the sedimentary successions of the Paraná Basin (Fig. 1) (Almeida *et al.*, 1981; Valeriano *et al.*, 2008).

In the context of the southern São Francisco Craton, segments of a Paleoproterozoic orogen are represented by the Mineiro Belt and the Quadrilátero Ferrífero mining district (Alkmim & Teixeira, 2017). Besides the Eastern Bahia orogenic domain (northern São Francisco Craton), these orogens record the collision between the Archean core of the São Francisco and Congo cratons during the transition between the Rhyacian and Orosirian periods (~2.0–1.9 Ga), which led to the consolidation of the São Francisco paleocontinent (Alkmim & Teixeira, 2017; Barbosa & Barbosa, 2017 and references therein).

The current outline of the São Francisco Craton was defined during the amalgamation of West Gondwana (Cordani *et al.*, 2013). In its southwestern and western margins, the Brasília Mobile Belt developed through a long succession of collisional events in which the final convergence and collision took place in the late Neoproterozoic, during the Brasiliano Orogeny (Fuck *et al.*, 2017). The Brasília Mobile Belt resulted from subduction of a wide oceanic lithosphere named Goiás-Pharusian Ocean, forming an oceanic island arc (~900–800 Ma), followed by the development of a continental arc (770–630 Ma) and the continental collision of the Amazonian, São Francisco, and Paranapanema paleocontinents (640–610 Ma) (Valeriano *et al.*, 2008; Fuck *et al.*, 2017; Frugis *et al.*, 2018).

In the Cretaceous, heterogeneous NW-SE oriented mafic potassic to ultrapotassic magmatism occurred in the Alto Paranaíba Igneous Province (APIP), extending from southwest Minas Gerais to the south of Goiás. The APIP mainly comprises kimberlites, lamproites, lamprophyres, kamafugites, and minor carbonatite intrusions (e.g. Gibson *et al.*, 1995; Guarino *et al.*, 2013; Azzone *et al.*, 2022; Carvalho *et al.*, 2022a, 2022b). The magmatism related to the APIP is widespread along the Brasília Mobile Belt that overthrusts the São Francisco Craton, between the SW margin of the craton and the NE margin of the Paraná Basin. Although placed within the Brasília Mobile Belt, previous studies of mantle xenoliths and xenocrysts associated with the APIP magmatism indicate that these rocks were likely sourced from the cratonic subcontinental lithospheric mantle (e.g. Carlson *et al.*, 2007; Fernandes *et al.*, 2021; Carvalho *et al.*, 2022a, 2022b). Additionally, gravimetric (Pereira & Fuck, 2005) and seismic tomographic (Rocha *et al.*, 2019a, 2019b) data suggest that the APIP belongs to the cratonic area. Therefore, the Canastra-1 kimberlite and its mantle xenoliths are inserted in the 'on-craton' context, representing the SW edge of the São Francisco Craton. Studies of the exotic magmatism of APIP have suggested that a heterogeneous and metasomatically enriched mantle source is needed to explain the genesis of these rocks in a single province (Gibson *et al.*, 1995; Araujo *et al.*, 2001; Guarino *et al.*, 2013; Woodhead *et al.*, 2019; Carvalho *et al.*, 2022a, 2022b).

In general, kimberlites and kamafugites from APIP are coeval with chronological ages mainly from ~90 to 80 Ma (e.g. Sgarbi *et al.*, 2004; Guarino *et al.*, 2013; Felgate, 2014; Carvalho *et al.*, 2022b). In contrast, the diamond-bearing Canastra-1 kimberlite, located in the SW of Minas Gerais, presents an older emplacement age of 120 Ma (Read *et al.*, 2004 after personal communication of Martin Doyle, De Beers). This kimberlite was emplaced at the SW margin of the São Francisco Craton and hosts the mantle xenoliths investigated here (Fig. 1). It is intrusive into Neoproterozoic metasedimentary rocks of the Brasília Mobile Belt (Canastra Group) and is part of a cluster with approximately 47 kimberlite

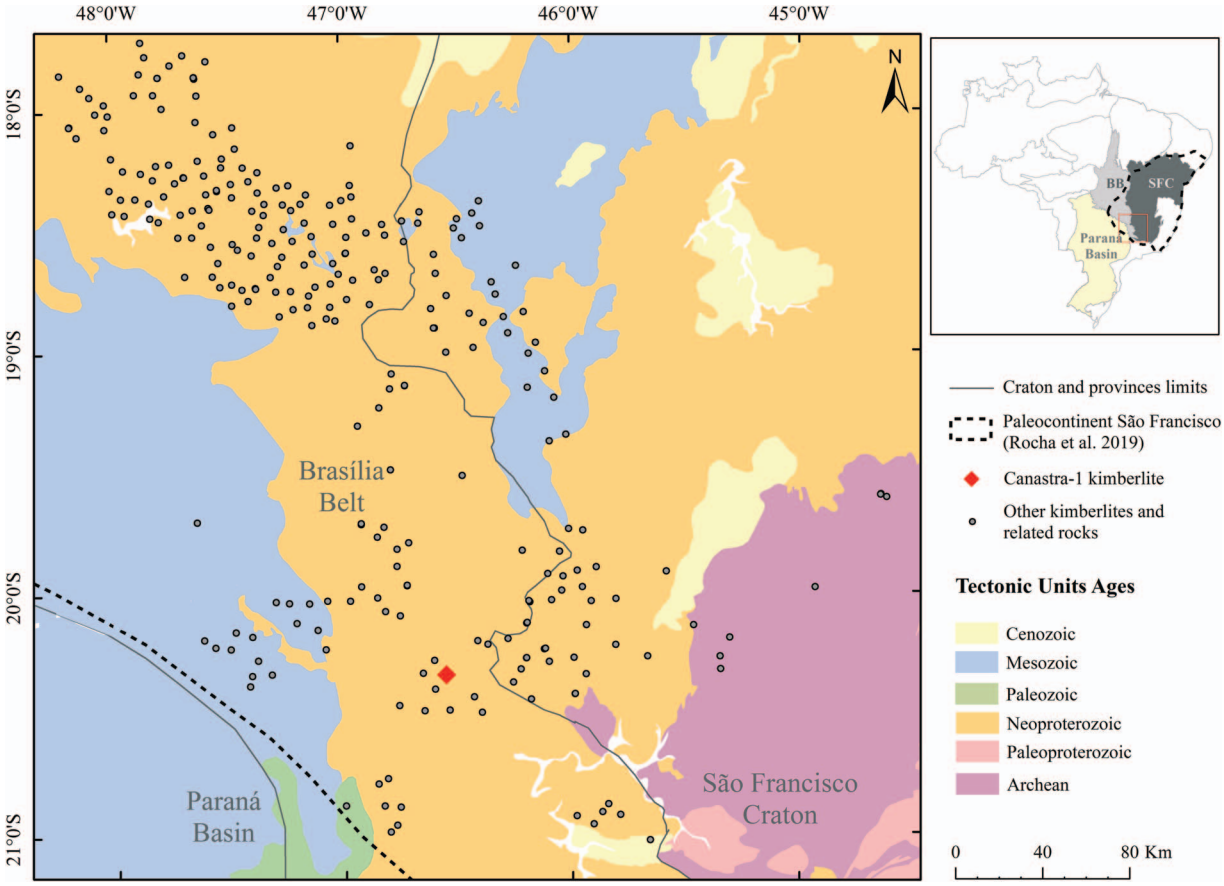

Fig. 1. Simplified geological map of the SW portion of the São Francisco Craton and surroundings with the location of Canastra-1 kimberlite. SFC: São Francisco Craton, BB: Brasília Belt. Delimitation of the São Francisco Paleocontinent after Rocha *et al.* (2019a) (dashed line).

intrusions that comprise the Serra da Canastra field (Cabral Neto *et al.*, 2017).

ANALYTICAL METHODS

The twenty-six mantle xenoliths analyzed to elaborate this paper were provided by De Beers Brazil Ltda. They represent a set of fresh (free of secondary alteration) xenoliths sampled as large drill-holes with no contact with the host kimberlite. Among these samples, twelve had their Electron Probe Microanalysis (EPMA) data obtained during the Master dissertation of Costa (2008) (Supplementary Tables S1–S2).

Electron probe microanalysis

Major element and compositional averages of mineral phases from Canastra-1 mantle xenoliths (olivine, orthopyroxene, clinopyroxene, garnet, pargasite, phlogopite, spinel, rutile, and ilmenite) were determined by wavelength-dispersive spectrometry (WDS) using a JEOL JXA-8230 Electron Probe Micro Analyzer (EPMA) at the Laboratório de Microssonda Eletrônica, Instituto de Geociências (IG), Universidade de Brasília (UnB), Brazil (Supplementary Tables S1–S3). The analyses were performed using an accelerating voltage of 15 kV, a beam current of 10 nA, and a beam diameter of 1 μm in the spot mode. For pargasite and phlogopite we employed the circle mode with 5 μm. Counting time on peak were 10 s per analyte peak and 5 s for the background. All results were reduced using an in-house ZAF correction program. The measurements were calibrated with the following mineral standards: andradite (CaO and FeO), albite (Na_2O), forsterite (MgO), microcline (K_2O, Al_2O_3 and SiO_2), pyrophanite (TiO_2 and MnO), chromium oxide (Cr_2O_3), nickel oxide (NiO), topaz (F), and vanadinite (Cl). To verify the data quality, we compared our new results for samples CAN1–88, CAN1–94, and CAN1–95 with those previously analyzed by Costa (2008). The detection limits are provided in the Supplementary Table S2.

Laser ablation inductively coupled plasma mass spectrometry

Most of the trace and rare earth elements (REE) were determined at the Laboratory of the Centro Interdipartimentale Grandi Strumenti (CIGS), the Università di Modena e Reggio Emilia, by Laser Ablation-Inductively Coupled Plasma Mass Spectrometry (LA-ICP-MS) (Supplementary Tables S1–S2). Additional measurements were conducted at the NAP Geoanalítica Laboratory of Geoscience Institute, University of São Paulo (USP) (Supplementary Tables S1–S2).

At CIGS, analyses were performed using a Thermo Fisher Scientific XSERIES 2 mass spectrometer coupled to a New Wave UP 213 laser ablation. Data reduction was performed with the Thermo Fisher Scientific PlasmaLab® software using NIST610, NIST612 and NIST614 as reference materials (Jochum *et al.*, 2005) (Supplementary Table S4). First, standard NIST612 was used to check the calibration with only NIST610 and NIST614, resulting in accuracy <10%. Then it was added to the sample calibration. The analysis conditions were laser spot 55 μm, an output 70% (on-sample fluency of 9 J/cm^2), a 10 Hz repetition rate, and a dwell

time 30 s. Prior to analyses, each spot surface was pre-ablated on a 65 μm laser spot size with an output of 45% and a 10 Hz repetition rate. ^{44}Ca was used as internal standard for clinopyroxene, garnet and pargasite.

At NAP, the trace elements were obtained using a New Wave 216 nm laser ablation system coupled to a Quadrupole ICP-MS PerkinElmer ELAN-6100 DRC (Dynamic Reaction Cell). ^{44}Ca was used as internal standard for clinopyroxene and garnet. The laser spot size varied between 20 and 40 μm and laser beam fluency was set at 20 J/cm^2. Prior to sample analyses, the system was tuned with the BCR-2G, BHVO-2G, and BIR-1G reference glasses (Supplementary Table S4) for maximum sensitivity, stability, and low oxide production rates ($^{232}Th^{16}O/^{232}Th < 0.1\%$). The detection limits are provided in the Supplementary Table S2.

$^{147}Sm/^{143}Nd$ systematics and $^{87}Sr/^{86}Sr$ isotopic ratios

The $^{147}Sm/^{143}Nd$, $^{143}Nd/^{144}Nd$ ($n = 32$), and $^{87}Sr/^{86}Sr$ isotopic ratios ($n = 25$) were determined for mineral separates (clinopyroxene and garnet) and whole-rock (with no Sr data) samples (Supplementary Table S5). Mantle xenoliths were wrapped in clean paper and plastic bags and then mechanically disaggregated into smaller pieces using a hammer. Afterwards clinopyroxene and garnet grains were carefully handpicked under a binocular microscope. The mineral and whole-rock powders were produced manually using an agate mortar and pestle. Individual aliquots of samples were used for Sm–Nd (0.1 g for Sm and 0.5 g for Nd with addition of mixed ^{149}Sm–^{150}Nd spike) and Sr (0.1 g; without addition of spike) isotope analysis. Sample digestion for both analyses followed the procedure described by Gioia & Pimentel (2000). Sm and Nd were separated in Teflon columns in two steps: cationic resin AG-50 W-X8 (200–400 mesh) to separate REE, anionic Eichrom LN Resin (100–150 μm) to separate Sm and Nd. Sr was separated using Eichrom SR-B100-S (100–150 μm) resin. Sm–Nd and Sr aliquots were loaded onto double Re filament assembly and the measurements were carried out by Thermal Ionization Mass Spectrometry (TIMS) using a Thermo-Finnigan Triton mass spectrometer at the Laboratório de Estudos Geodinâmicos, Geocronológicos e Ambientais (LEGGA), UnB, Brazil. The data were corrected for mass fractionation by normalizing to $^{146}Nd/^{144}Nd$ of 0.7219 and $^{88}Sr/^{86}Sr$ value of 8.3752. The analyses of BHVO-2 and NIST-SRM NBS-987 standards gave $^{143}Nd/^{144}Nd = 0.512962 \pm 0.000005$ ($n = 4$, 2σ) and $^{87}Sr/^{86}Sr = 0.71026 \pm 0.00001$ ($n = 2$, 4σ), respectively. These values are identical within uncertainty to the reference values of 0.512957 ± 0.000006 (Raczek *et al.*, 2003) and 0.71025 ± 0.00011 (Thirlwall, 1991). Blank values are lower than 50 pg.

RESULTS

Petrography

The collection of garnet-bearing xenoliths from drill cores of the Canastra-1 kimberlite includes twelve sheared lherzolites (from which nine samples were selected for petrography analyses), six clinopyroxenites, two websterites, three pargasite websterites, two eclogites, and one dunite (Supplementary Table S6 and Supplementary Fig. S1). Modal percentages of mineral phases were determined by digital point counting using the JMicroVision software (Roduit, 2007). For each thin section (each one with 37–43 x 21–25 mm) at least 3000 points were counted (Supplementary Table S6 and Supplementary Information).

Macroscopically, the xenoliths are ovoid in shape, they do not display interaction with the host kimberlite, and usually are <15 cm in diameter. Sheared lherzolites exhibit mosaic-porphyroclastic texture showing porphyroclasts of orthopyroxene, clinopyroxene, and garnet surrounded by fine-grained recrystallized neoblasts of olivine. Pyroxenites (websterites and clinopyroxenites) and eclogites show coarse texture, whereas the dunite displays granuloblastic texture (Harte, 1977). Clinopyroxenites and eclogites are petrographically similar, being differentiated only by mineral chemistry data.

Sheared garnet lherzolites are composed of olivine (52–72%), orthopyroxene (9–23%), clinopyroxene (8–23%), and garnet (5–18%). *Olivine* dominantly occurs as neoblasts (up to 0.5 mm in diameter, ~94% of total olivine) with subordinate porphyroclasts (1.0–2.8 mm in diameter). The former olivine exhibits polygonal habit, with straight grain boundaries and common 120° triple point junctions (Fig. 2a). The relict grains show signs of deformation such as undulose extinction and kink bands. Serpentine is developed along fractures in porphyroclasts and in the boundary of neoblasts. *Orthopyroxene* porphyroclasts (1.5–4.0 mm in diameter) tend to be rounded to elongated. They also display undulose extinction and recrystallization features along grain boundaries, such as tiny neoblast 'tails' stretching out from larger pyroxene porphyroclasts (Fig. 2b, c, f). Rarely, kink bands were observed in some grains. *Clinopyroxene* porphyroclasts (1.5–5.1 mm in diameter) show irregular to rounded shape, with smoothly curved grain boundaries. These porphyroclasts normally show thin exsolution of orthopyroxene (Fig. 2d). They display reaction features as spongy and cloudy margins (Fig. 2e). Subhedral rounded *garnet* (0.9–2.8 mm in diameter) occurs as porphyroclasts or as subrounded inclusions (~0.8 mm) within clino- and orthopyroxenes (Fig. 2b). Pyroxenes within garnet crystals is less frequent. In most instances, garnet crystals are systematically surrounded by kelyphitic coronae (reaction rims) of variable thickness (Fig. 2f). Lherzolitic samples represent a transition sequence from low to moderate deformation evidenced by non-fluidal to fluidal textures (Fig. 2g, h). None of the studied samples have high degree of deformation expressed by the presence of garnet neoblasts in disrupted textures (Harte, 1977).

Garnet clinopyroxenites are the coarsest-grained lithotype, exhibiting crystals with similar dimensions (Fig. 3a). Clinopyroxene (46–56%) and garnet (44–55%) have subrounded to subhedral habits. *Clinopyroxene* crystals vary from 1.7 to 5.0 mm in diameter, and rarely show exsolution lamellae of orthopyroxene. They commonly exhibit thick spongy rims (Fig. 3b). *Garnet* (2.2–5.5 mm in diameter) occurs as highly fractured grains, in which a thick kelyphite rim (corona) is ubiquitous in all samples (Fig. 3c). The poikilitic texture may be seen in some garnet with subrounded inclusions of clinopyroxene (Fig. 3d).

Garnet websterites may be anhydrous (2 samples) or hydrated (3 samples). The anhydrous websterites are medium- to coarse-grained and present variable modal abundance expressed by clinopyroxene (13–56%), orthopyroxene (25–78%), and garnet (9–19%). Crystals are intensely fractured and show triple point junctions and lobate contacts, typical of equilibrated mantle assemblages (Fig. 4a). *Clinopyroxene* occurs with bimodal distribution sizes (1.4–3.0 and 4.5–7.0 mm in diameter), usually exhibiting a turbid appearance, and shows fine exsolution lamellae of orthopyroxene (Fig. 4b). *Orthopyroxene* mainly appears as large (5.0–6.2 mm in diameter) and elongated crystals, but small and anhedral grains were also observed (1.2–2.8 mm in diameter) (Fig. 4c). *Garnet* (1.4–3.7 mm in diameter) occurs interstitially in aggregates as deformed crystals, with highly irregular shapes. Occasionally, crystals are completely resorbed by phlogopite and

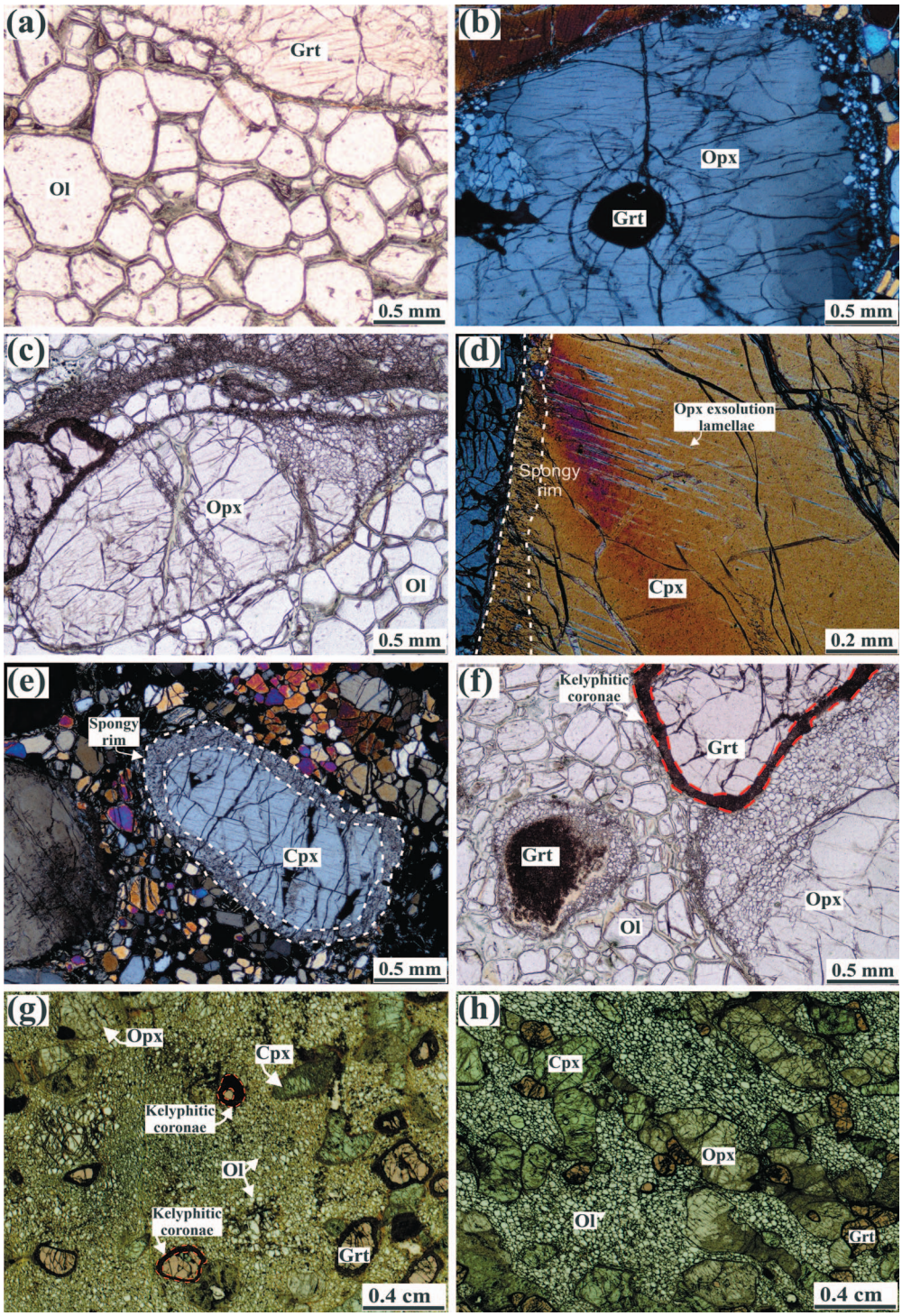

Fig. 2. Photomicrographs and scanned thin sections of garnet lherzolites from Canastra-1 kimberlite showing the main mineral assemblages and main textures. (a) Neoblasts of olivine (CAN1–101). (b) Recrystallization along orthopyroxene grain boundaries and (c) into tiny orthopyroxene neoblasts 'tails' stretching out from larger pyroxene porphyroclasts (CAN1–88). (d) Clinopyroxene with orthopyroxene exsolution lamellae (CAN1–107). (e) Well-developed clinopyroxene spongy rim (CAN1–86). (f) Garnets surrounded by kelyphitic coronae of variable thickness (CAN1–88). (g-h) Scanned images of thin sections showing the main aspects of lherzolitic xenoliths highlighting progressive deformation illustrated by the mineral orientation (CAN1–97 and CAN1–88). Plane- (a, c, f) and crossed- (b, d, e) polarized lights. Abbreviations: Cpx, clinopyroxene; Opx, orthopyroxene; Grt, garnet; Ol, olivine.

pyroxenes, forming kelyphitic rims. The hydrated (pargasite-bearing) garnet websterites are coarse-grained samples with clinopyroxene (33–42%), orthopyroxene (24–35%), garnet (12–29%), and pargasite (7–19%) (Fig. 4d). *Clinopyroxene* sizes vary from 0.8 to 3.8 mm in diameter; it has subhedral shapes, often displays undulose extinction, and exsolution lamellae of orthopyroxene. *Orthopyroxene* (0.7–3.0 mm in diameter) forms equant habits with curvilinear grain boundaries. *Garnet* (0.8–3.0 mm in diameter) has irregular shapes, but sometimes is slightly elongated. It is generally fresh, with only minor reaction

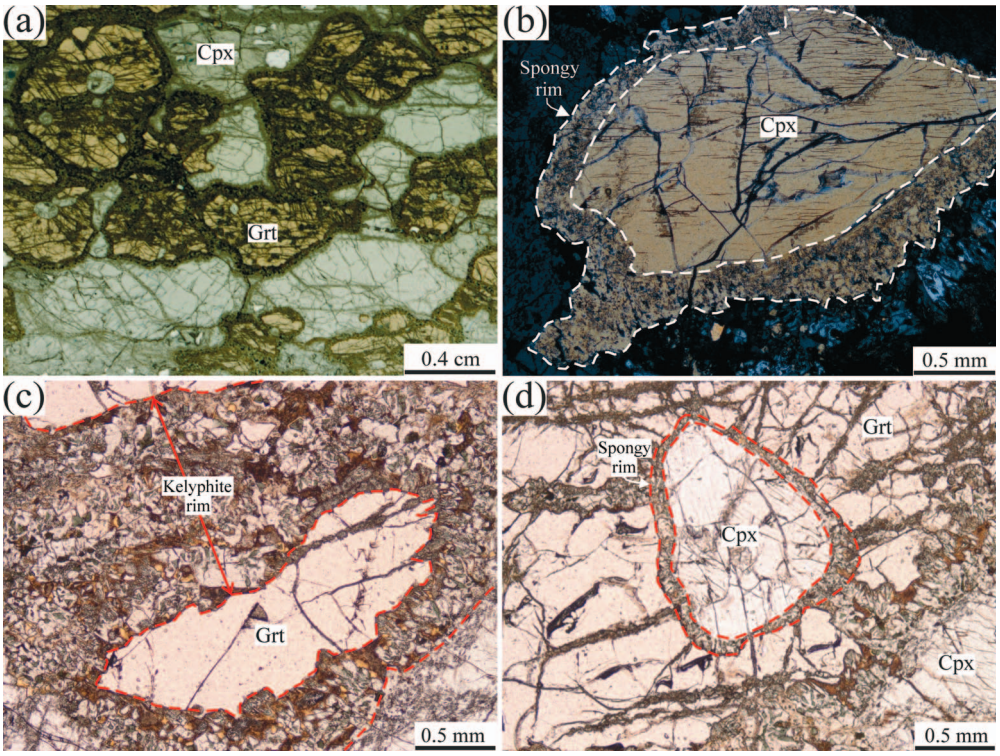

Fig. 3. Photomicrographs and scanned thin section of garnet clinopyroxenite xenoliths from Canastra-1 kimberlite showing the main mineral assemblages and texture. (a) Scanned image of the thin section CAN1–94. (b) Well-developed spongy rim in clinopyroxene (CAN1–126). (c) Fractured garnet with thick kelyphite rim (CAN1–142). (d) Poikilitic texture in garnet (CAN1–213). Plane (c, d) and crossed (b) polarized lights. Abbreviations: Cpx, clinopyroxene; Grt, garnet.

rims when in contact with pargasite (Fig. 4e). *Garnet* generally exhibits poikilitic texture, in which a single crystal may include both pyroxenes as inclusions. *Pasrgasite* occurs as brown to greenish-brown grains (Fig. 4d, e, f), which are typically interstitial (~1.3 mm in diameter), mainly in contact with garnet and orthopyroxene grains. Nevertheless, subhedral and larger grains are also identified (up to 2.2 mm in diameter).

Eclogites are essentially bimineralic samples composed of clinopyroxene (40–48%) and garnet (52–60%) (Fig. 5a), which is a common characteristic of this rock type (Jacob, 2004). *Clinopyroxene* (3.0–5.5 mm in diameter) appears to have been pervasively generated, as exemplified by its spongy (reacted) nature (Fig. 5b). Conversely, subhedral *garnet* (4.0–6.0 mm in diameter) has fresh cores, although commonly fractured. Comparatively, this mineral shows lighter colors than those observed in clinopyroxenites. Crystal rims exhibit kelyphitic texture with an assemblage of secondary minerals (orthopyroxene and clinopyroxene) that surrounds every grain (Fig. 5a).

The **dunite** sample displays complete recrystallization of *olivine* to a granuloblastic texture of small equant mosaic crystals (<0.6 mm in diameter; Fig. 5c) (Harte, 1977). *Garnet* (1.0–2.3 mm in diameter) occurs as porphyroclasts with 2% of modal abundance. These rounded fractured grains are rimmed and sometimes nearly completely replaced by kelyphitic intergrowths (Fig. 5d).

Late textures observed in Canastra-1 mantle xenoliths encompass secondary minerals and textures developed by reactions with metasomatic agents. In the studied samples, these textures are frequently associated with clinopyroxene and garnet (Fig. 6). Spongy clinopyroxene occurs in all rock types except in pargasite-bearing websterites. It typically occurs as variable thick coronae (<300 μm), and as cross-cutting veinlets or irregular patches and domains (Figs. 2e; 3b; 4d-f; 5a, b). The boundaries between spongy-textured clinopyroxenes and surrounding minerals are sharp and seem not to be controlled by cracks across the crystals. The spongy texture of clinopyroxenes is more pervasive in eclogites than in other rock types. In these samples, each grain is surrounded and crosscut by zones of spongy clinopyroxene, which dominate in up to 50% of the mineral volume (Fig. 5b). This process affects practically all the clinopyroxene grains observed in the studied rock types.

Other important reaction processes common to all xenoliths, except for pargasite-bearing websterites, are the kelyphitic rims around garnet crystals (Fig. 2f-h; 3a, c; 4a, c; 5a, d). In lherzolites and eclogites, this texture occurs as a brownish rim (50–500 μm) surrounding garnet, in which minerals are barely recognizable under cross-polarized light (Fig. 6a). However, the cores of these grains remain fresh. Garnet may be partially or entirely replaced by extremely fine-grained minerals in pargasite-free websterites and in the dunite (Fig. 6b). Clinopyroxenites exhibit the most notable fine-grained, fibrous intergrowth of multiple phases, with clear fibrous and radial structures (Fig. 6c).

The main secondary phases involved in these reactions consist of orthopyroxene, clinopyroxene, spinel, rutile, and ilmenite. Subhedral phlogopite occurs at the edges of the kelyphitic rims. Distinct structures and domains can only be confirmed through the backscattered electron images (BSE) (Fig. 6d).

The first domain adjacent to garnet is composed of large crystals of orthopyroxene that contain several small, irregularly shaped patches of clinopyroxene (Fig. 6e). These minerals enclose thin vermicular lamellae of spinel, forming a fine-scale pyroxene-spinel kelyphite (Fig. 6f). Therefore, the spinel habit gives rise to the fibrous appearance of kelyphites recognized under an optical-microscope transmitted light (Obata & Ozawa, 2011). Very fine-grained opaque minerals are distributed in this zone. Nodular

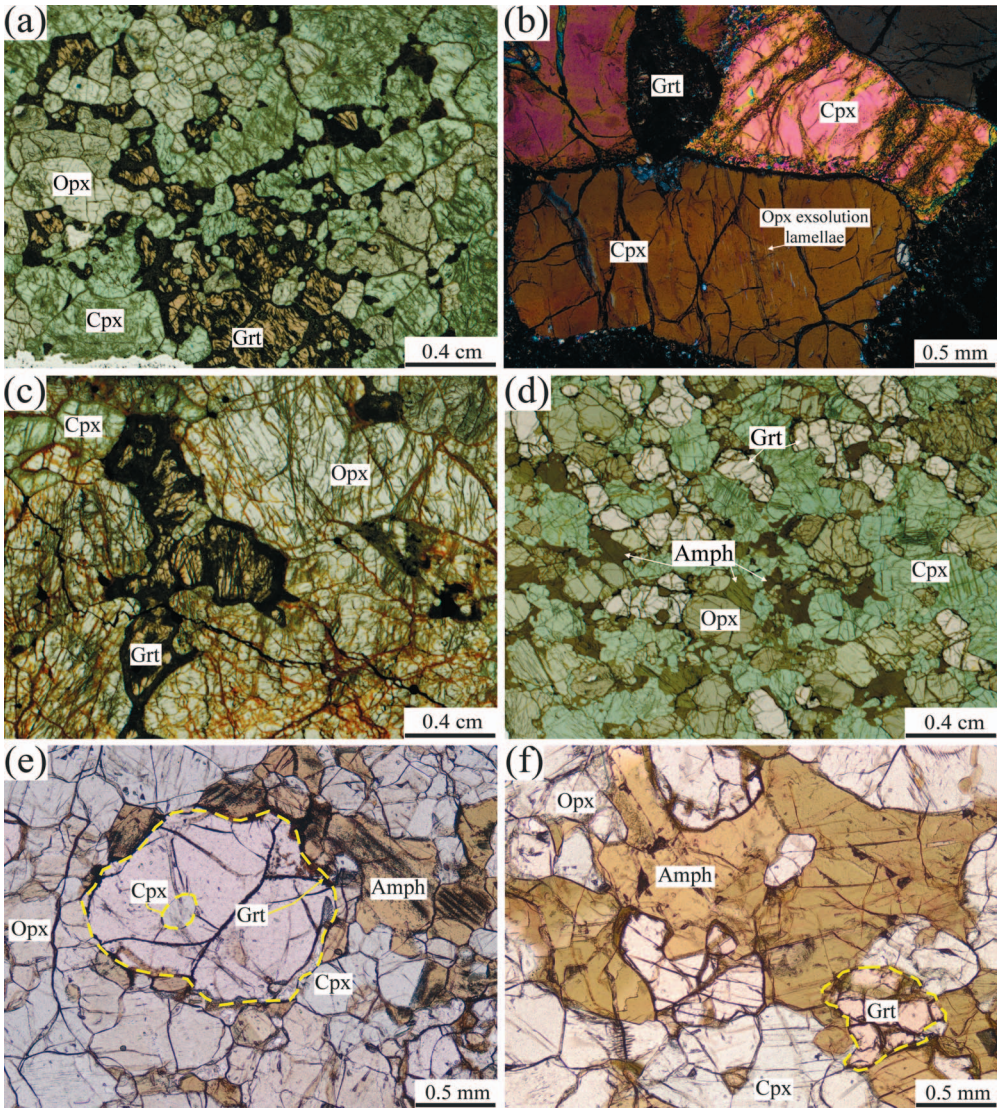

Fig. 4. Photomicrographs and scanned thin sections of anhydrous (a-c) and hydrated (d-f) olivine-free websterites from Canastra-1 kimberlite. (a) Triple point junctions and lobate contacts (CAN1–182). (b) Clinopyroxene shows turbid appearance and discreet exsolution lamellae of orthopyroxene (CAN1–182). (c) Large and extremely fractured orthopyroxene crystals with serpentine filling the spaces (CAN1–209). (d) Representative mineral assemblage and texture of hydrated websterites (CAN1–95). (e) Fresh garnet grains with minor reaction rims when in contact with pargasite (CAN1–143). (f) Pargasite crystals (CAN1–95). Plane- (e, f) and crossed- (b) polarized lights and scanned thin sections (a, b, d). Abbreviations: Cpx, clinopyroxene; Opx, orthopyroxene; Grt, garnet; Amph, amphibole (pargasite).

green spinels occur at or around the boundaries of the first domain (Fig. 6g). In lherzolites, the kelyphite is surrounded by a thin rim of coarser orthopyroxene and clinopyroxene, separating the kelyphitic coronae from the surrounding neoblasts of olivine. Phlogopite (90–300 μm) surrounds the garnet grains. In clinopyroxenites, rutile occurs associated with phlogopite (Fig. 6a, h). These grains have rounded to subangular interstitial habit and exhibit exsolution of ~15% ilmenite as lamellae and rims (Fig. 6h).

Major and trace elements

Supplementary Tables S1 and S2 present individual measurements of primary mineral phases (olivine, type 1 orthopyroxene, type 1 clinopyroxene, garnet, and pargasite), as well as their representative (average) compositions. Since no core-rim differences of main oxides (<0.5%) were observed in primary mineral phases, the average compositions were plotted in the major element diagrams. In addition, secondary phases related to kelyphitic rims (phlogopite, type 2 orthopyroxene, type 2 clinopyroxene, spinel, rutile, and ilmenite) had their major element compositions determined (Supplementary Table S3).

The occurrence of **olivine** is restricted to lherzolites and dunite. It has homogeneous and typical mantle forsterite composition ($Fo_{0.88–0.91}$), Mg# (0.89–0.91; Mg# = Mg/(Fe + Mg) molar), NiO (0.33–0.40 wt %), and CaO (<0.10 wt %) in both porphyroclasts and neoblasts. Trace elements were not determined for olivine.

Primary **orthopyroxenes** (type 1) occur in lherzolites and websterites (both anhydrous and hydrated), whereas in clinopyroxenite, eclogite, and anhydrous websterite they are products of reaction (type 2) related to kelyphitic rims. Type 1 orthopyroxenes from lherzolites and anhydrous websterites contain strong enstatite endmember ($En_{0.88–0.90}$ $Fs_{0.08–0.10}$ $Wo_{0.02–0.03}$), while hydrated websterites comprise enstatite enriched in the ferrosilite component ($En_{0.73–0.78}$ $Fs_{0.21–0.26}$ $Wo_{0.00–0.01}$). Similarly, enstatites from lherzolites (90–92) and anhydrous websterites (90) have higher Mg# than those from hydrated websterites (74–78) (Supplementary Tab. S1). Hydrated websterites show higher Al_2O_3

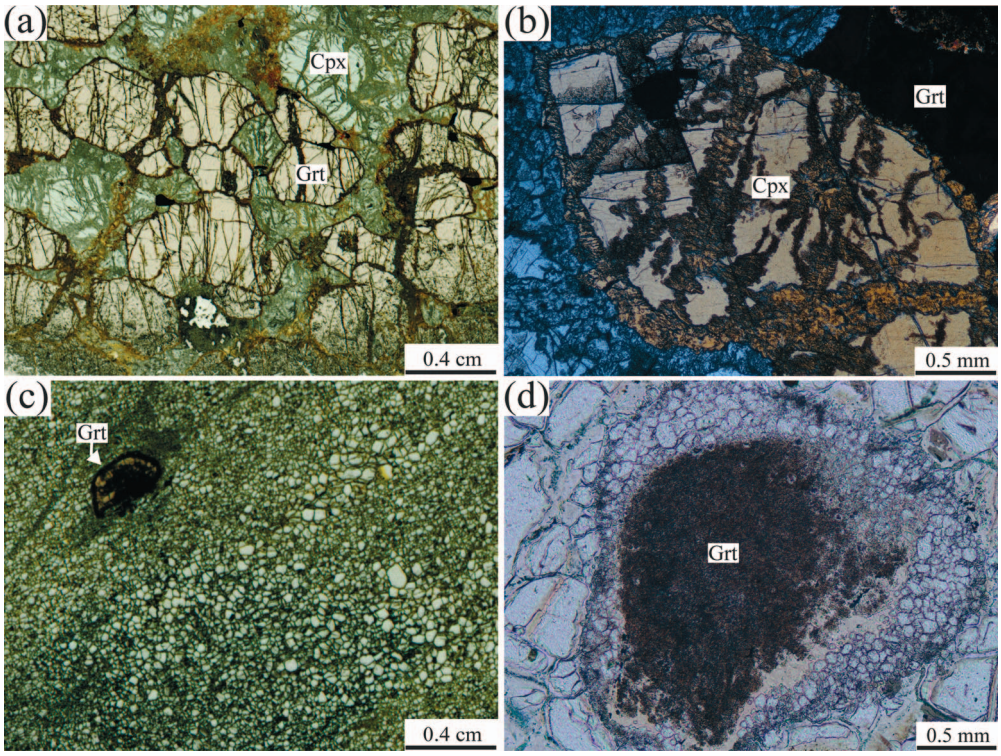

Fig. 5. Scanned thin sections and photomicrograph of eclogite (a,b) and dunite (c,d) xenoliths from Canastra-1 kimberlite. (a) Scanned thin section and photomicrograph in crossed-polarized light showing the representative mineral assemblage and texture (b) of eclogite xenolith (CAN1–206). Scanned images of thin section from dunite xenolith (CAN1–180) showing the texture with equant olivine neoblasts (d) and garnet porphyroclasts surrounded by kelyphitic coronae (e). Abbreviations: Cpx, clinopyroxene omphacite; Grt, garnet.

(3.55–4.34 wt %) coupled with lower CaO (0.23–0.50 wt %) contents compared to lherzolites and anhydrous websterites (1.00–1.15 wt %; and 1.13–1.34 wt %, respectively) (Supplementary Tab. S1). Trace elements were not determined for orthopyroxenes.

Augite occurs in lherzolites ($En_{56.2–58.7}$ $Wo_{34.9–37.3}$ $Fs_{5.7–7.1}$), clinopyroxenites ($En_{56.3}$ $Wo_{36.6–36.7}$ $Fs_{7.0–7.2}$), and anhydrous websterites ($En_{50.6–54.6}$ $Wo_{37.9–43.4}$ $Fs_{5.4–8.5}$), while diopside occurs in hydrated websterites ($En_{39.7–40.9}$ $Wo_{48.0–39.5}$ $Fs_{10.1–11.1}$). In contrast, clinopyroxenes ($En_{46.6}$ $Wo_{46.6–47.6}$ $Fs_{5.8–6.8}$) from eclogite are omphacite with high Na_2O (>3.5 wt %; Fig. 7a) and jadeite endmember (0.25–0.26). Most clinopyroxenes show intermediate to high Mg# (lherzolites = 0.89–0.90, clinopyroxenites = 0.86–0.91, anhydrous websterites = 0.89, and eclogite = 0.87–0.89) with hydrated websterites containing the lowest values (0.78–0.80) (Fig. 7). In general, lherzolites (CaO = 16.53–17.60 wt %, Al_2O_3 = 1.74–2.03 wt %), clinopyroxenites (CaO = 17.92–20.88 wt %, Al_2O_3 = 1.66–2.22 wt %), and anhydrous websterites (CaO = 17.17–17.22 wt %, Al_2O_3 = 1.86–1.90 wt %) display lower CaO and Al_2O_3 contents than hydrated websterites (CaO = 20.99–21.90 wt.%, Al_2O_3 = 5.59–6.39 wt %) and eclogites (CaO = 18.32–18.34 wt %, Al_2O_3 = 6.23–5.46 wt %). In the same way, lherzolites (9.67–12.91), clinopyroxenites (8.57–13.22), and anhydrous websterites (8.41–8.57) have higher Ca/Al (molar) compared to hydrated websterites (5.06–8.49) and eclogites (2.90–3.07) (Supplementary Tables S1–S2). In Fig. 7, the Mg# decreases accompanied by Na_2O (a) content while CaO (b) and TiO_2 (c) increase from lherzolites to clinopyroxenites and anhydrous websterites.

In the primitive mantle (PM, Sun & McDonough, 1989) normalized diagram, clinopyroxenes from Canastra-1 mantle xenoliths show variable enrichment in light-REE (LREE) compared to heavy-REE (HREE) (i.e. Ce/Yb_N = 10.52–93.63, where N = normalized values) (Fig. 8a, c, e, g). In general, hydrated websterites (Ce/Yb_N = 10.52–50.61, usually >41) and eclogites (Ce/Yb_N = 60.90–93.63) are even more enriched in LREE over HREE than lherzolites (Ce/Yb_N = 12.06–29.44), clinopyroxenites (Ce/Yb_N = 24.32–48.02), and anhydrous websterites (Ce/Yb_N = 13.41–18.67) (Fig. 8 a, c, e, g). Clinopyroxenes have convex-upward LREE patterns caused by strong fractionation between LREE and HREE (Ce/Yb_N = 10.52–93.63) with a relatively flat slope from La to Nd (La/Sm_N = 0.57–2.74, average of 1.24) (Fig. 8). In variable extents, all rock types have positive anomalies of U (except for clinopyroxenites), La-Ce, and Sr (except for hydrated websterites) coupled with negative anomalies of Nb-Ta-Ti, Pb and Zr-Hf in the PM-normalized multielement diagram (Fig. 8 b, d, f, h).

Garnets from the Canastra-1 mantle xenoliths are mainly pyrope, in which this endmember decreases from dunite ($Py_{72.2–77.3}$) toward lherzolites ($Py_{70.9–75.6}$), anhydrous websterites ($Py_{70.5–72.4}$), clinopyroxenites ($Py_{62.3–68.5}$), eclogites ($Py_{49.3–56.5}$), and hydrated websterites ($Py_{42.0–49.7}$). Eclogites ($Alm_{25.6–27.9}$) and hydrated websterites ($Alm_{34.3–41.7}$) have strong almandine endmember compared to dunite ($Alm_{8.2–13.3}$), lherzolites ($Alm_{11.7–16.2}$), clinopyroxenites ($Alm_{12.6–20.2}$) and anhydrous websterites ($Alm_{15.1–16.7}$). Regarding the grossular endmember, eclogite garnets have the highest grossular content ($Gros_{16.6–24.4}$), whereas the other mantle xenoliths contain uniform composition ($Gros_{10.8–17.7}$). Dunite (Mg# = 0.87), lherzolites (Mg# = 0.83), anhydrous websterites (Mg# = 0.82), and clinopyroxenites (Mg# = 0.79) show higher Mg# than eclogites (Mg# = 0.66) and hydrated websterites (Mg# = 0.54). The Al_2O_3 contents are relatively uniform among all rock types (20.16–22.96 wt %) while Cr_2O_3 contents are higher in dunite (3.23 wt %), lherzolites (2.69 wt %) and anhydrous websterites (2.12 wt %) compared to clinopyroxenites (0.39 wt %), hydrated websterites (0.22 wt %), and eclogites (0.10 wt

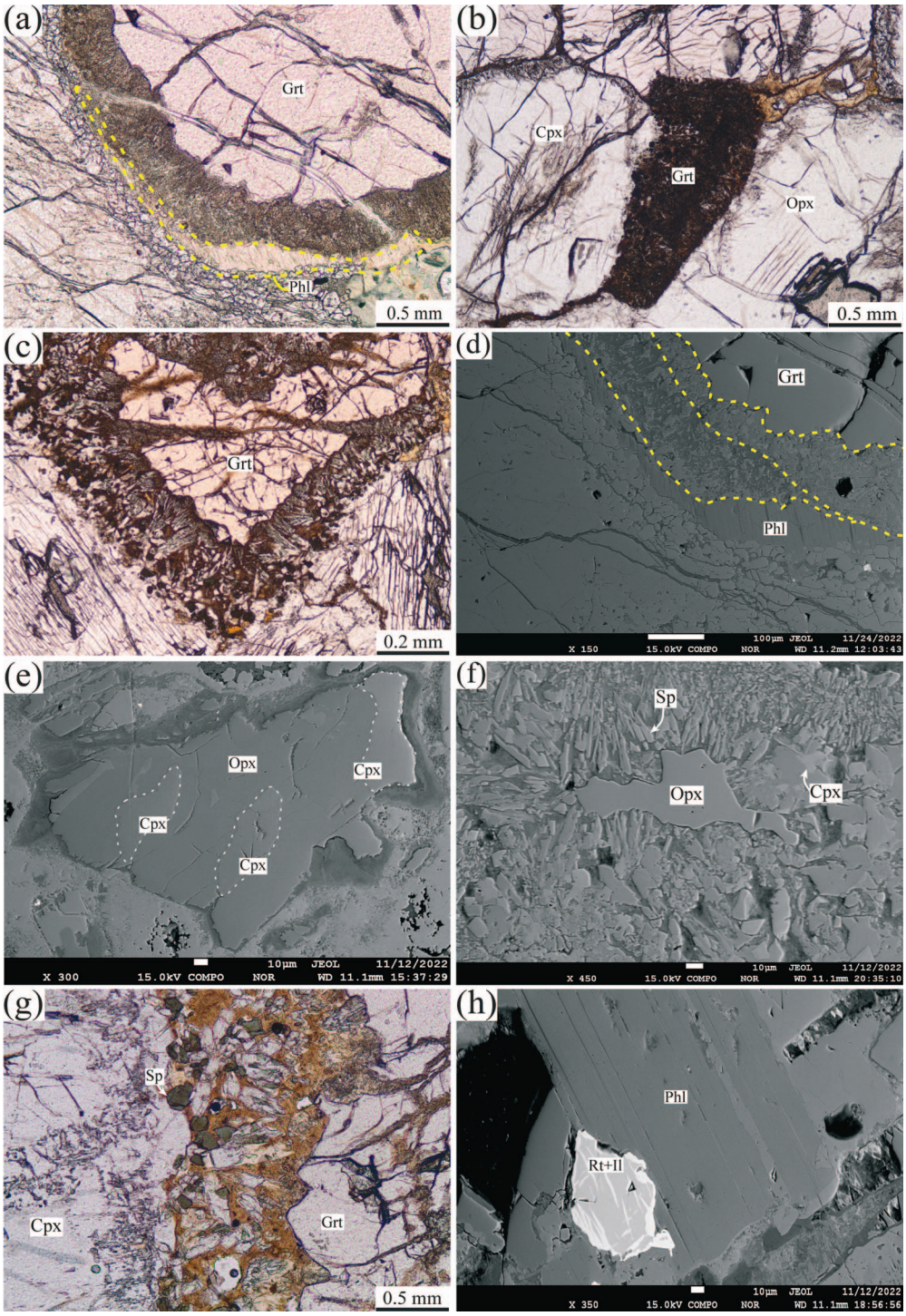

Fig. 6. Thin sections and backscatter electron (BSE) images of late textures observed in Canastra-1 kimberlite mantle xenoliths. (a) Garnet crystal with kelyphitic rim and phlogopite along its boundaries (CAN1–86: lherzolite). (b) Garnet completely replaced by extremely fine-grained minerals (CAN1–182: anhydrous websterite). (c) Garnet exhibiting the largest kelyphitic rims among studied xenoliths (CAN1–213: clinopyroxenite). (d) Distinct domains with phlogopite along kelyphitic boundaries (CAN1–86: lherzolite). (e) Large crystal of orthopyroxene with several small, irregularly shaped patches of clinopyroxene (CAN1–94: clinopyroxenite). (f) Vermicular lamellae of spinel forming a fine-scale pyroxene-spinel symplectite (CAN1–209: anhydrous websterite). (g) Nodular spinel (CAN1–142: clinopyroxenite). (h) rutile with exsolution of ilmenite as lamellae and rims associated with phlogopite (CAN1–174: clinopyroxenite). BSE images (d, e, f, h) and plane-polarized light (a, b, c, g). Abbreviations: Phl, phlogopite; Cpx, clinopyroxene; Opx, orthopyroxene; Grt, garnet; Sp, spinel; Rt, rutile; Il, ilmenite.

%). According to their CaO and Cr_2O_3 contents, garnets from Canastra-1 are classified as lherzolitic (G9: lherzolites, anhydrous websterites, and dunite), pyroxenitic (G4: most clinopyroxenites and hydrated websterites), and eclogitic (G3: eclogites and two clinopyroxenites) (Fig. 9). Note that although lherzolites, anhydrous websterites, and dunite plot within the G5 pyroxenitic field, these samples are classified as belonging to the G9 due to their high Mg# (>0.7; Grütter *et al.*, 2004).

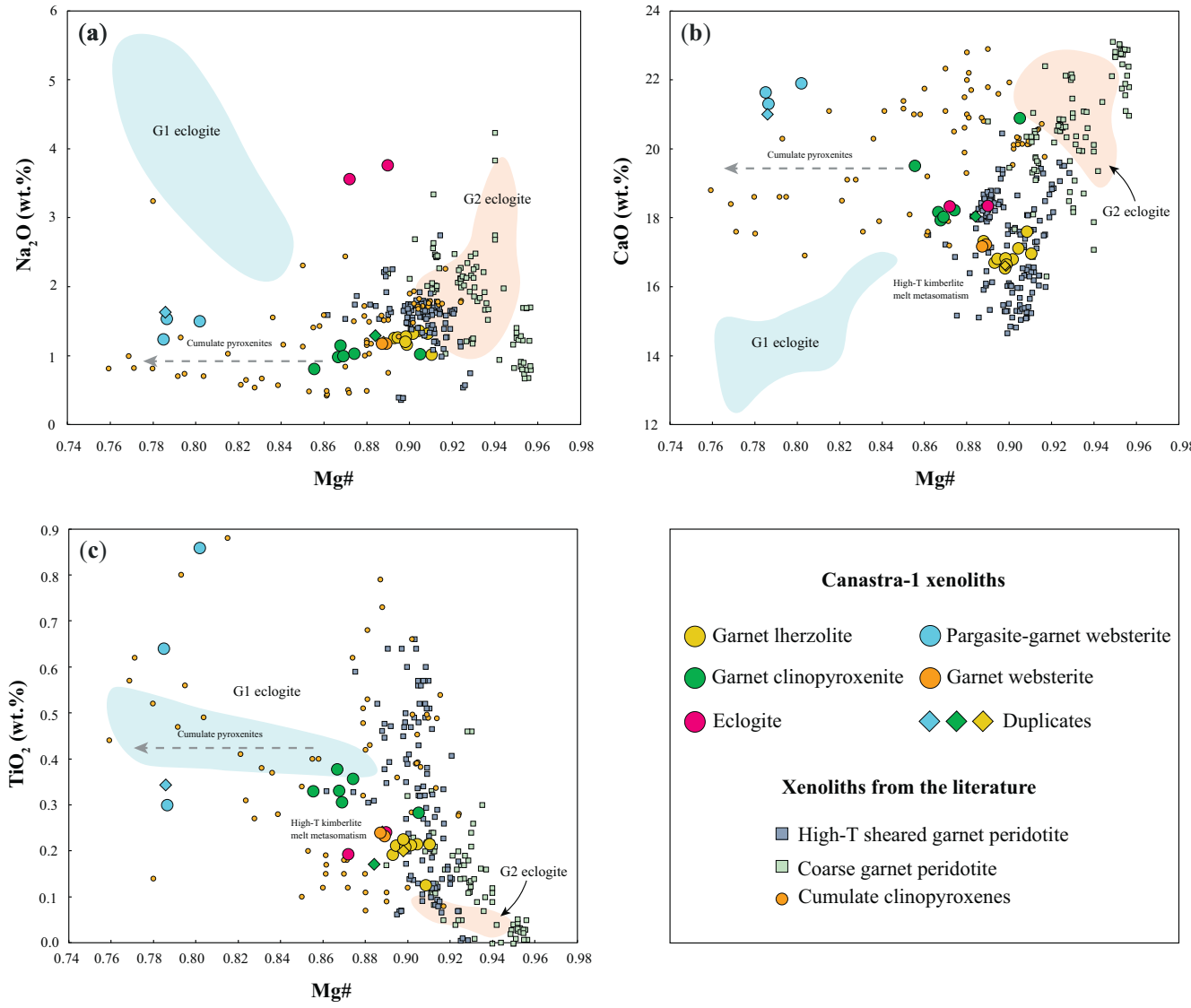

Fig. 7. Clinopyroxene major element compositions from Canastra-1 kimberlite mantle xenoliths. Eclogites plot between Group I and Group II eclogites (Viljoen *et al.*, 2005), whereas sheared lherzolites, anhydrous websterites, and clinopyroxenites show strong affinity with high-T sheared peridotites (Viljoen *et al.*, 2009; Ionov *et al.*, 2010; Baptiste *et al.*, 2012; Agashev *et al.*, 2013; Kargin *et al.*, 2017; Tappe *et al.*, 2021). Although clinopyroxenites are compositionally similar to sheared lherzolites, they have lower Mg#. Low-T coarse-grained peridotites were plotted for comparison (Viljoen *et al.*, 2009; Ionov *et al.*, 2010; Baptiste *et al.*, 2012; Kargin *et al.*, 2016; Fitzpayne *et al.*, 2020). Pargasite websterites show compositional affinity with cumulate pyroxenites from Cascade Cordillera (Müntener *et al.*, 2001), Southeastern Australia (Lu *et al.*, 2018), Sierra Nevada (Lee *et al.*, 2006), and Cameroon Volcanic Line (Puziewicz *et al.*, 2023).

In the REE diagram, in contrast to clinopyroxenes that are enriched in LREE/HREE, all garnets display normal 'depleted' pattern characterized by LREE<HREE ($Ce/Yb_N < 0.32$, Fig. 10a, c, e, g). In the PM-normalized multielement diagram (Fig. 10b, d, f, h), garnets from all rock types show incipient enrichment in U accompanied by depletion of LREE (i.e. La-Ce) and Sr (pronounced). Lherzolites, clinopyroxenites, and hydrated websterites show positive anomalies of Pb (pronounced in lherzolites). In different extents, lherzolites, anhydrous websterites, and clinopyroxenites are characterized by positive Zr-Hf anomalies. Controversially, clinopyroxenites show concomitant enrichment and depletion of Zr-Hf. Except for clinopyroxenites, garnets from other rock types have negative anomalies of Ti.

The occurrence of **pargasite** is restricted to the hydrated websterites. It is classified as pargasite with average Mg# = 0.80, TiO_2 = 2.03 wt %, Al_2O_3 = 14.38 wt %, Na_2O = 2.38 wt %, and CaO = 11.28 wt %. Pargasite is characterized by the same convex-upward REE pattern observed in the coexisting clinopyroxene with fractionated LREE/HREE (Ce/Yb_N = 10.26–57.06) and almost flat slope from La to Nd (La/Sm_N = 0.61–1.35, average of 0.98) (Fig. S2a). In the PM-normalized multielement diagram (Fig. S2b), these samples present positive anomalies of Nb as well as negative anomalies of Th-U, Ta, Sr, and Zr-Hf.

The mineral phases identified in kelyphitic rims around garnets from Canastra-1 xenoliths are type 2 orthopyroxene, type 2 clinopyroxene, phlogopite, spinel, rutile, and ilmenite (Supplementary Table S3). Due to the small size of these minerals, only measurements carried out on garnets with well-developed kelyphitic rims were achieved. Thus, these minerals are from lherzolite (CAN1–86), clinopyroxenites (CAN1–94 and CAN1–174), and anhydrous websterites (CAN1–182 and CAN1–209). **Phlogopite** laths present in garnet kelyphitic rims from lherzolite (CAN1–86: TiO_2 = 1.29–2.47 wt % and Cr_2O_3 = 0.91–1.71 wt %), clinopyroxenite (CAN1–174: TiO_2 = 2.64–4.63 wt % and

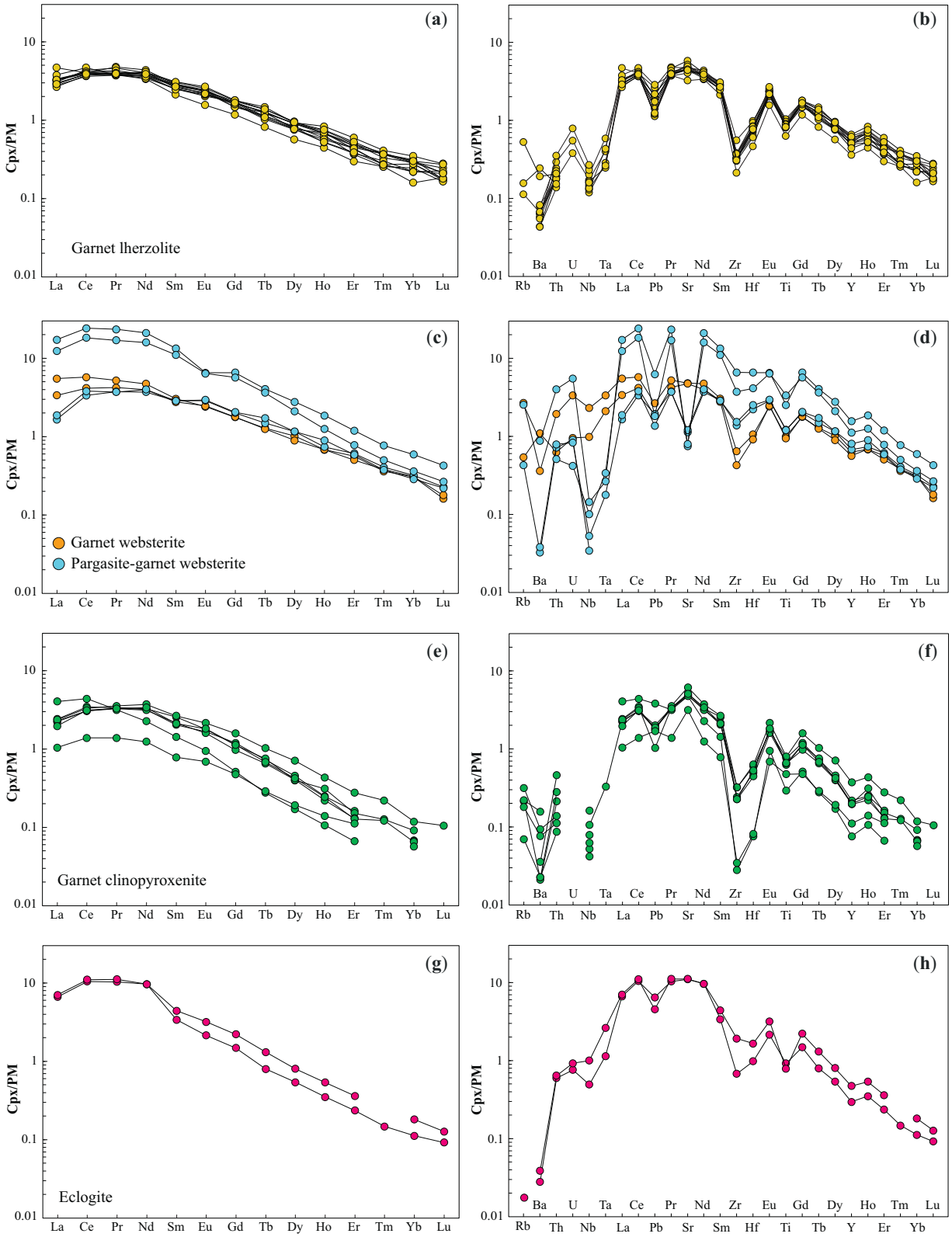

Fig. 8. Primitive mantle (PM; Sun & McDonough, 1989) (a) normalized rare earth and (b) multielement diagrams of clinopyroxenes from Canastra-1 mantle xenoliths.

Cr_2O_3 = 0.80–1.34 wt %), and anhydrous websterite (CAN1–209: TiO_2 = 2.04–3.78 wt % and Cr_2O_3 = 0.93–1.91 wt %) show high-TiO_2 (high-Ti) and high-Cr_2O_3 (high-Cr) contents (Giuliani *et al.*, 2014, 2016; Kargin *et al.*, 2019) (Fig. 11 and Supplementary Table S3). Phlogopite crystals from these three rock types have similar average variation of K_2O (8.10–10.39 wt %), Al_2O_3 (12.78–15.97 wt %), and FeO (5.05–7.05 wt %), as well as relatively low Mg# (0.83–0.90 wt %) (Fig. 11 and Supplementary Table S3). Type 2 orthopyroxene averages from garnet kelyphitic rims of samples CAN-86, CAN1–182, and CAN1–209 are enriched in TiO_2

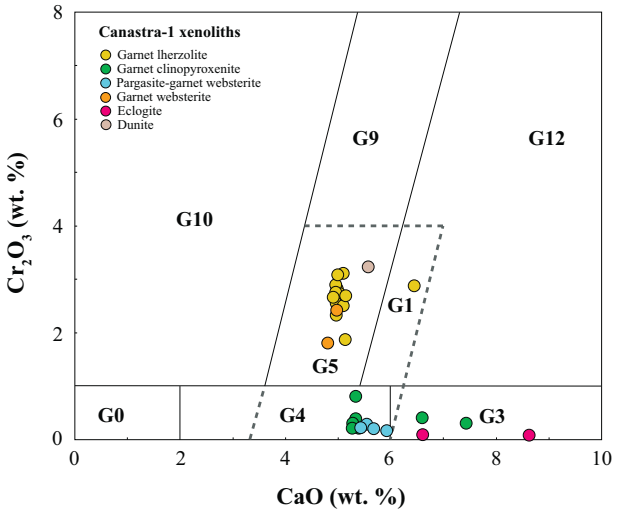

Fig. 9. Classification diagram of garnet considering CaO and Cr_2O_3 contents (Grütter *et al.*, 2004). Garnets from sheared lherzolites, anhydrous websterites, and sheared dunite are classified as lherzolitic (G9) due to their high Mg# (>0.7). Most clinopyroxenites and hydrated websterites are classified as pyroxenitic (G4), whereas eclogites and two clinopyroxenites are classified as eclogitic (G3).

(0.47–0.67 wt %), Cr_2O_3 (0.33–0.55 wt %), Al_2O_3 (10.72–11.93 wt %), and CaO (1.34–1.79 wt %) contents but depleted in Na_2O (<0.06 wt %) and Mg# (0.82–0.84) compared to type 1 orthopyroxenes (TiO_2 = 0.22–0.23 wt %, Cr_2O_3 = 0.17–0.20 wt %, Al_2O_3 = 1.00–1.04 wt %, CaO = 1.22–1.28; Na_2O = 0.17–0.19 wt %, and Mg# = 0.90) (Supplementary Tables S1–S3). Except for lherzolite CAN1–86, the composition of type 2 clinopyroxenes (from garnet kelyphitic rims) for the other xenoliths was obtained (CAN1–94, CAN1–174, CAN1–182, and CAN1–209). These secondary clinopyroxenes have higher contents of TiO_2 (1.50–1.72 wt %), Al_2O_3 (11.55–13.77 wt %), and CaO (19.29–20.09 wt %), with lower Na_2O (0.21–0.53 wt %) and Mg# (0.78–0.83) compared to those from type 1 (TiO_2 = 0.26–0.36 wt %, Al_2O_3 = 1.83–1.90 wt %, CaO = 17.17–18.22 wt %, Na_2O = 0.99–1.17 wt %, and Mg# = 0.87–0.89) (Supplementary Tables S1–S3). **Spinel** averages are Al_2O_3-rich (54.53–58.11 wt %) with low TiO_2 (<0.35 wt %), and variable MgO (18.58–20.49 wt %), Cr_2O_3 (1.52–9.70 wt %) and FeO (15.21–17.36 wt %) contents. **Rutile** (TiO_2 = 96.47–97.42 wt %) and Mg-rich **ilmenite** (picroilmenite: TiO_2 = 53.90–54.35 wt %, FeO = 32.57–32.94, MgO = 9.85–10.28 wt %, and Cr_2O_3 = 0.70–0.98 wt %) were identified and analyzed only in the clinopyroxenite sample CAN1–174. Comparatively, ilmenites from garnet kelyphitic rims have similar composition to those from kimberlites (Mitchell, 1995; Wyatt *et al.*, 2004).

Pressure and temperature estimates

The positive correlation between Al_2O_3 and Mg# accompanied by negative correlation of CaO shown by two pyroxenes indicates the equilibrium between these mineral phases (Fig. S3). This equilibrium is corroborated by the well-defined positive correlations between the Mg# of olivine vs. orthopyroxene (r^2 = 0.69) and clinopyroxene (r^2 = 0.89) (not shown). Equilibrium temperature and pressure estimates were calculated assuming 4.0 GPa (garnet-facies) using several reliable geothermobarometers from the PTEXL Excel spreadsheet (created by T. Köhler in the 1990s and modified and updated by T. Stachel in 2024 at the University of Alberta, Canada: https://doi.org/10.5683/SP3/IMYNCL) (Supplementary Table S7). For this study, we used geothermometers based on two-pyroxenes (Krogh, 1988; Brey & Koehler, 1990; Taylor, 1998), garnet-clinopyroxene equilibrium (Sudholz *et al.*, 2022), Ca in orthopyroxene (Brey & Koehler, 1990), and single-clinopyroxene (Mercier, 1980; Nimis & Taylor, 2000). Selected geobarometers are based on garnet-orthopyroxene (Nickel & Green, 1985; Brey & Koehler, 1990; Taylor, 1998), single-pyroxene equilibrium (Nimis & Taylor, 2000; Nimis *et al.*, 2020), and Cr-in-clinopyroxene (Sudholz *et al.*, 2021). We additionally applied the REE-in-garnet-clinopyroxene thermometer for eclogites and garnet peridotites proposed by Sun & Liang (2015).

Note that the thermobarometry proposed for single-pyroxene could only be apply to orthopyroxene-bearing mantle xenoliths (e.g. Nimis & Taylor, 2000; Nimis *et al.*, 2020). For this reason, we have decided to avoid the results obtained from these works for clinopyroxenites and eclogites. It is well-documented that accurate and precise pressure estimates for these xenoliths are generally not possible due to the absence of suitable coexisting minerals (i.e. orthopyroxene coexisting with garnet or clinopyroxene) (e.g. Viljoen *et al.*, 2005; Beyer *et al.*, 2015; Aulbach *et al.*, 2020).

Canastra-1 sheared lherzolites have high and uniform temperature (high-T) averages (1212–1290°C), which are in the same range defined for anhydrous websterites (1239–1248°C) and clinopyroxenites (1191–1237°C) (Fig. 12a). Conversely, eclogites (978–982°C) show the lowest temperatures (lower-T), which are slightly lower than those from hydrated websterites (875–926°C) (Fig. 12a). Consistent pressure estimates are restricted to lherzolites (5.3–5.6 GPa) and anhydrous websterites (5.4–5.5 GPa) (Fig. 12a). These pressure estimates correspond to depth ranges of 174–186 km (Fig. 12a). Pressure and temperature estimates constrained by lherzolites and anhydrous websterites correspond to the geotherm of 40 mW/m^2 (Fig. 12a). Thus, pressure estimates were extrapolated for clinopyroxenites (~5.3–5.5 GPa), eclogites (~4.0 GPa), and hydrous websterites (~3.4–3.8 GPa) based on their temperatures projected on the conductive geotherm of 40 mW/m^2 (Hasterok & Chapman, 2011) (Fig. 12a). It should be noted that although the temperature estimates of hydrated websterites are compatible with those obtained for eclogites, the geothermobarometers employed in this study were calibrated for anhydrous conditions. Considering the stability field defined for pargasite, in which temperature reaches around 1100 ± 50°C at pressures from 1 to 3 GPa (Green, 2015), our pressure estimates (~3.4–3.8 GPa) are overestimated. Therefore, we can infer a maximum pressure estimate for our hydrated websterites at around ~3 GPa (probably between 2–3 GPa). In Fig. 12b, eclogites plot within the geotherm of 40 mW/m^2 while pargasite websterites in the stability field defined for pargasite (Green, 2015). These samples plot along with the tentative Archean subduction path, in which pargasite websterites plot close to the field defined for modern blueschists and eclogites (Aulbach & Smart, 2023 and references therein) (Fig. 12c).

Sm–Nd systematics and Sr–Nd isotopic ratios

Supplementary Table S5 displays the Sr–Nd isotopic ratios of lherzolites (n = 10), pargasite websterites (n = 2), clinopyroxenite (n = 1), and eclogite (n = 1). Selected clinopyroxene (n = 13) and garnet (n = 8) mineral separates had their Sr–Nd isotopic ratios determined, whereas the whole-rock samples have only Nd data (n = 10).

Lherzolites have clinopyroxenes ($^{143}Nd/^{144}Nd$ = 0.51273–0.51293, ϵNd = +1.8 to +5.7, $^{87}Sr/^{86}Sr$ = 0.70560–0.70770; where $\epsilon Nd = (^{143}Nd/^{144}Nd_{sample}/^{143}Nd/^{144}Nd_{CHUR} - 1) \times 10\,000$) and garnets ($^{143}Nd/^{144}Nd$ = 0.51287–0.51315, ϵNd = +4.5 to +10.1, $^{87}Sr/^{86}Sr$ = 0.70704–0.70869) with intermediate to high $^{143}Nd/^{144}Nd$ coupled with

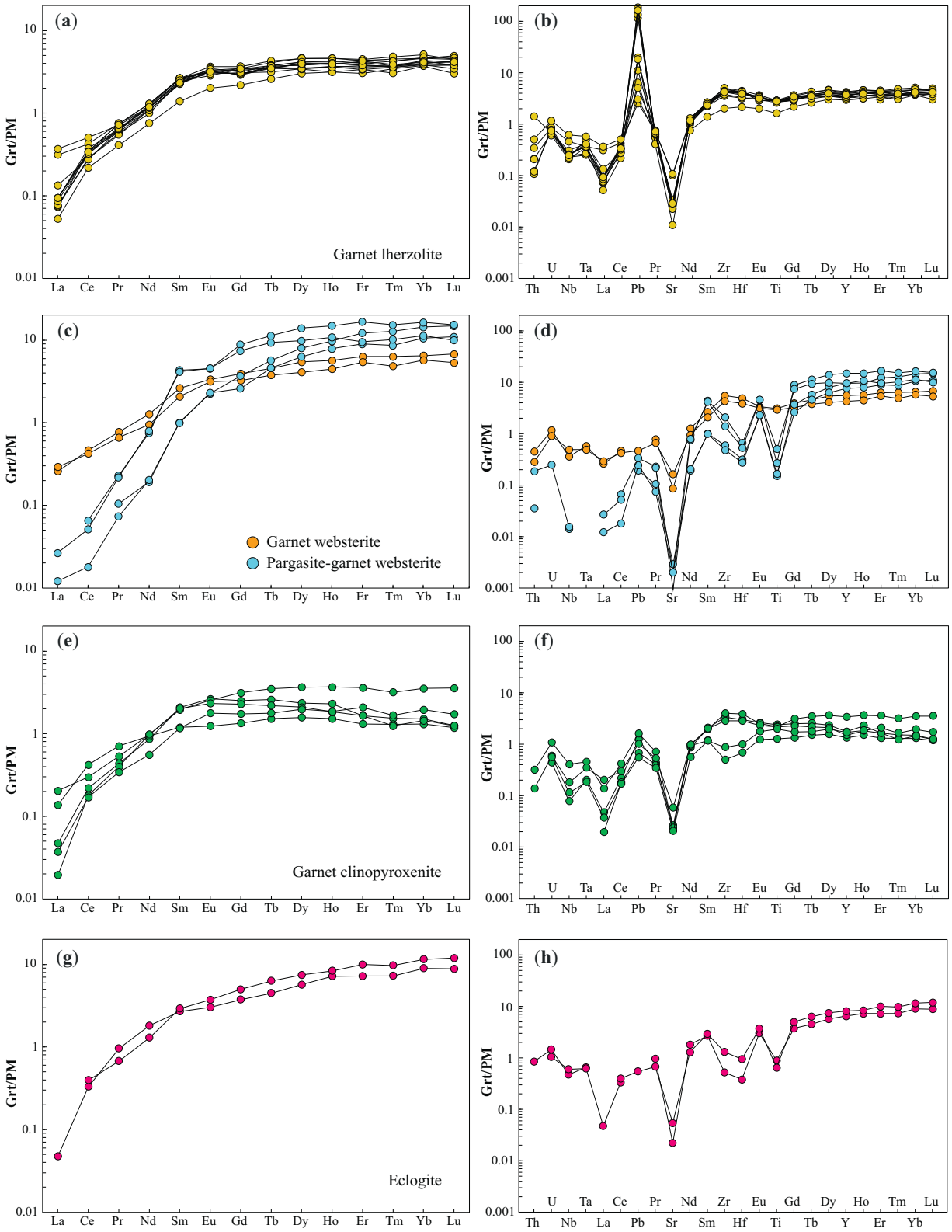

Fig. 10. Primitive mantle (PM; Sun & McDonough, 1989) (a) normalized rare earth and (b) multielement diagrams of garnets from Canastra-1 mantle xenoliths.

enriched $^{87}Sr/^{86}Sr$ isotopic ratios (Fig. 13 and Supplementary Table S5). In general, garnets show higher Sr and Nd isotopic ratios than clinopyroxenes (Fig. 13 and Supplementary Table S5). Whole-rock lherzolites have similar $^{143}Nd/^{144}Nd$ ratios (0.51277–0.51292) and ϵNd (+2.5 to +5.6) compared to their clinopyroxene separates. The clinopyroxenite sample has the same pattern observed in the lherzolites (Fig. 13 and Supplementary Table S5) considering clinopyroxene ($^{143}Nd/^{144}Nd = 0.51292$, $\epsilon Nd = +5.5$, $^{87}Sr/^{86}Sr = 0.70753$), garnet ($^{143}Nd/^{144}Nd = 0.51303$, $\epsilon Nd = +7.6$, $^{87}Sr/^{86}Sr = 0.70831$) and whole-rock ($^{143}Nd/^{144}Nd = 0.51292$, $\epsilon Nd =$

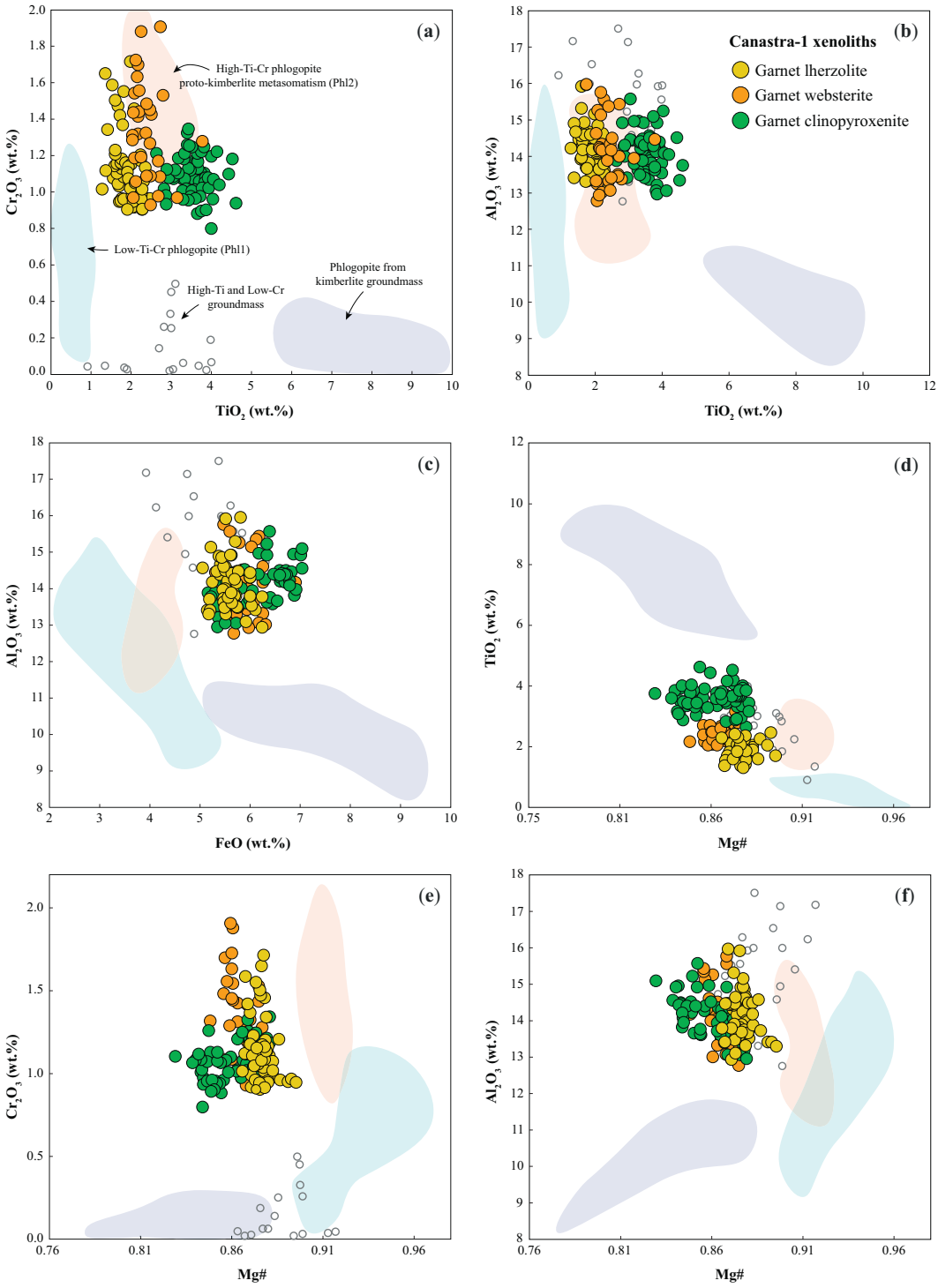

Fig. 11. Bivariate plots for major and minor elements of phlogopite from Canastra-1 mantle xenoliths. High-Ti-Cr phlogopite from mantle xenoliths (Giuliani *et al.*, 2016); type 1 phlogopites (Phl1) from mantle xenoliths and kimberlite xenocrysts (Giuliani *et al.*, 2014, 2016; Kargin *et al.*, 2019); type 2 phlogopites (Phl2) (Kargin *et al.*, 2019); high-Ti and low-Cr groundmass phlogopites (Giuliani *et al.*, 2016; Kargin *et al.*, 2019); kimberlite phlogopites from the groundmass (Fritschle *et al.*, 2013).

+5.4) isotopic compositions. The Sr–Nd distribution pattern defined by the lherzolitic and clinopyroxenite samples is scattered and near-horizontal with depleted (high) Nd at a given enriched (high) Sr isotopic ratio compared to the array formed by kimberlites (Fig. 13).

Pargasite websterites had only clinopyroxenes ($^{143}Nd/^{144}Nd$ = 0.51196–0.51198, $\epsilon Nd = -12.9$ to -13.3, $^{87}Sr/^{86}Sr$ = 0.70894–0.71003) and whole-rocks ($^{143}Nd/^{144}Nd$ = 0.51196–0.51227, $\epsilon Nd = -7.2$ to -13.2) successfully analyzed (Fig. 13 and Supplementary Table S5). They represent the most enriched samples among all rock types with the lowest Nd and the highest Sr isotopic ratios (Fig. 13 and Supplementary Table S5). Likewise, clinopyroxene ($^{143}Nd/^{144}Nd = 0.51232$, $\epsilon Nd = -6.3$, $^{87}Sr/^{86}Sr = 0.70912$) and garnet ($^{143}Nd/^{144}Nd = 0.51226$, $\epsilon Nd = -7.3$, $^{87}Sr/^{86}Sr = 0.70842$) separates,

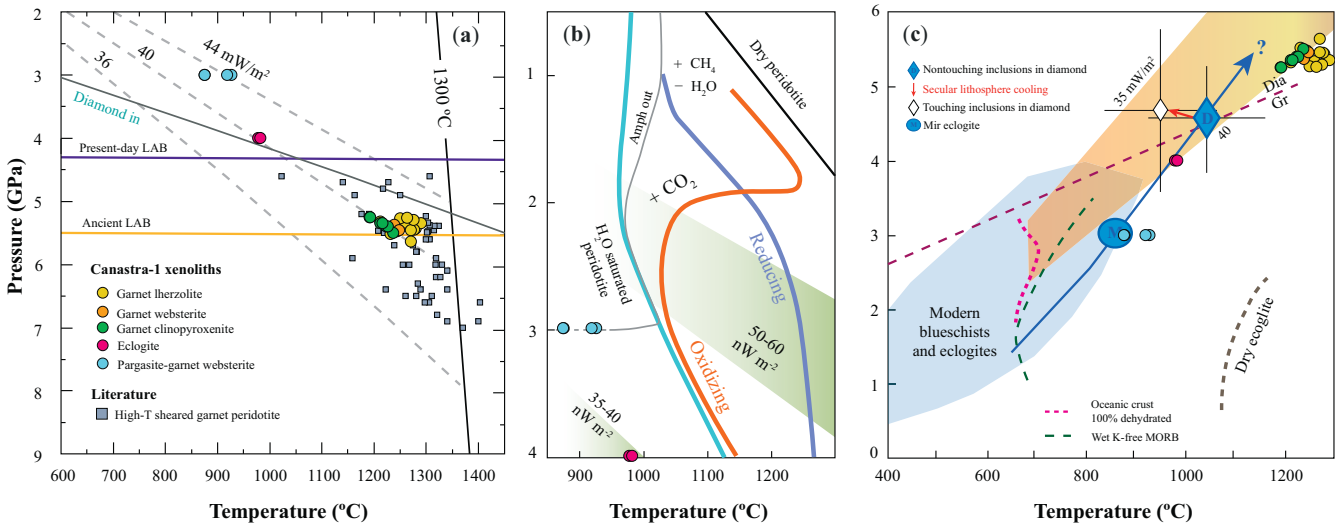

Fig. 12. (a) Pressure versus temperature diagram after Giuliani *et al.* (2023) containing the conductive model geotherms from Hasterok & Chapman (2011). Sheared lherzolites and anhydrous websterites from Canastra-1 show reliable geothermobarometers and plot within the geotherm of 40 mW/m^2 in the ancient lithosphere-asthenosphere boundary (LAB = 174–186 km). The present-day LAB occurs at 143 km depth (Ciardelli *et al.*, 2022), indicating extensive lithospheric thinning in the last 120 Ma. Due to the lack of precise pressure estimates for clinopyroxenites and eclogites, the temperature estimates of these samples were extrapolated to the geotherm of 40 mW/m^2 (Hasterok & Chapman, 2011), which represents that defined by lherzolites and anhydrous websterites. Pressure estimate for pargasite websterites is assumed as 3.0 GPa (Green, 2015). Sheared lherzolites, anhydrous websterites, and clinopyroxenites overlap the field defined by high-T sheared peridotites from the Kaapval and Siberian cratons (Ionov *et al.*, 2010; Baptiste *et al.*, 2012; Agashev *et al.*, 2013; Tappe *et al.*, 2021). (b) Pressure versus temperature diagram after Green (2015) and Aulbach (2018). According to the pressure and temperature estimates of pargasite websterites, they plot within the amphibole stability field while eclogites plot within the geotherm of 40 mW/m^2. Shown for comparison are the nominally dry peridotite solidus (water undersaturated) and water-saturated peridotite solidus coupled with the effect of oxidizing versus reducing conditions (Green, 2015; Aulbach, 2018). (c) Pressure versus temperature diagram showing that sheared lherzolites, anhydrous websterites, and clinopyroxenites plot within the geotherm of 40 mW/m^2 (after Stachel *et al.*, 2022 and Aulbach & Smart, 2023). Pargasite websterites and eclogites plot within the tentative Archean subduction path (blue arrow). For comparison, modern blueschists and eclogites are plotted. Touching inclusions in diamonds record lower average temperatures, indicative of secular lithosphere cooling (orange arrow). Also shown are the solidus (dotted line) for dry (gray) and for K-free wet mid-ocean ridge basalt (MORB)-like eclogite (green); a curve (purple) for 100% dehydration of oceanic crust.

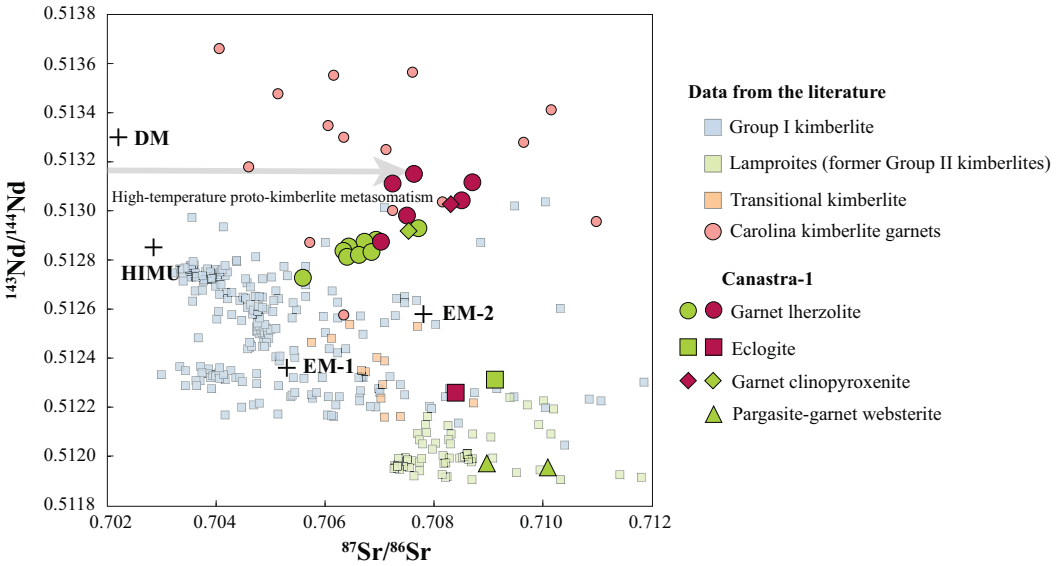

Fig. 13. Sr–Nd isotopic composition of clinopyroxene (green symbols) and garnet (purple symbols) from Canastra-1 xenoliths. For comparison, the depleted mantle (DM), HIMU, enriched mantle 1 (EM1) and enriched mantle 2 (EM2) mantle end-members (Hart *et al.*, 1992), worldwide kimberlites from Group 1, Group 2 (orangeites) and Transitional kimberlites (Nowell *et al.*, 2004; Becker & le Roex, 2006; Becker *et al.*, 2007; Coe *et al.*, 2008; Tappe *et al.*, 2017, 2020, 2022, 2023 and references therein), and Carolina kimberlite garnets (Gervasoni *et al.*, 2022) are plotted.

as well as the whole-rock (^{143}Nd/^{144}Nd = 0.51235, ϵNd = −5.6) from the eclogite sample are slightly less enriched compared to the hydrated websterites (Fig. 13 and Supplementary Table S5). Thus, as observed in the mineral chemistry data, these xenoliths are considerably enriched with respect to the lherzolites, clinopyroxenites, and anhydrous websterites. Note that in this case, the term enriched consists in low-Nd and high-Sr isotopic ratios. For comparison, in Fig. 13 were plotted the worldwide Group I or archetypal kimberlites (Nowell *et al.*, 2004; Becker & le Roex, 2006; Becker *et al.*, 2007; Tappe *et al.*, 2017, 2020 and

references therein), transitional kimberlites (Nowell *et al.*, 2004; Becker *et al.*, 2007), and lamproites (former micaceous Group II kimberlites or orangeites; Nowell *et al.*, 2004; Becker & le Roex, 2006; Coe *et al.*, 2008; Tappe *et al.*, 2022, 2023), as well as the garnet xenocrysts from the Carolina kimberlite (Gervasoni *et al.*, 2022).

Based on the ^{147}Sm–^{143}Nd systematics, consistent isochron ages were calculated based on sheared lherzolites and clinopyroxenite isotopic compositions (Fig. S4 and Supplementary Table S5). In contrast, coherent ages for eclogites and pargasite websterites were not achieved. Thus, four ages were determined using (1) clinopyroxene, garnet and whole-rock of lherzolite xenoliths [$n = 21$; 146.1 ± 8.2 Ma, initial $^{143}Nd/^{144}Nd = 0.51273$, MSWD = 5.8] (Fig. S4a), (2) clinopyroxene and garnet of lherzolite xenoliths [$n = 14$; 149.6 ± 9.4 Ma, initial $^{143}Nd/^{144}Nd = 0.51272$, MSWD = 7.7] (Supplementary Fig. S4b), (3) clinopyroxene, garnet and whole-rock for lherzolite and clinopyroxenite xenoliths [$n = 24$; 139.8 ± 7.9 Ma, initial $^{143}Nd/^{144}Nd = 0.51274$, MSWD = 6.5] (Fig. S4c), and (4) clinopyroxene and garnet for lherzolite and clinopyroxenite xenoliths [$n = 16$; 143.2 ± 9.0 Ma, initial $^{143}Nd/^{144}Nd = 0.51273$, MSWD = 8.6] (Fig. S4d). These Cretaceous ages are slightly older than the age proposed for the emplacement of the host kimberlite (120 Ma; Read *et al.*, 2004 after personal communication of Martin Doyle, De Beers). It is important to consider that the mentioned report does not detail essential information regarding radiogenic dating, such as what material was used, and the analytical method applied.

However, aiming to avoid the compositional influence of the host kimberlite in the whole-rock Sm/Nd isochrons, we plotted two-point clinopyroxene-garnet isochrons (Shu *et al.*, 2014) considering the measured $^{143}Nd/^{144}Nd$ isotopic ratios (Supplementary Tab. S5) while the $^{147}Sm/^{144}Nd$ ratios were calculated using the Sm and Nd concentrations (in ppm) of clinopyroxene and garnet (Supplementary Tab. S1). Based on the available results, six two-point isochrons were constructed for high-T sheared lherzolites (samples CAN1–89, 96, 97, 99, 100, and 101). Three of them (CAN1–96 = 121 ± 39 Ma, CAN1–99 = 115 ± 26 Ma, and CAN1–101 = 125 ± 17 Ma) present ages resembling the kimberlite emplacement age (120 Ma) (Fig. 14). Conversely, sample CAN1–100 shows an older age (195 ± 31 Ma) while the others have younger results relative to 120 Ma. The initial $^{143}Nd/^{144}Nd$ isotopic ratios for samples CAN1–96, CAN1–99, and CAN1–101 are, respectively, 0.51271, 0.51284, and 0.51278. Remarkably, the two-point isochrons from high-T sheared lherzolites (Fig. 14) reflect either cooling ages or emplacement of the kimberlite magma (Shu *et al.*, 2014). Considering the whole-rock, the obtained age is slightly older (average of 145 ± 4 Ma) than that of the clinopyroxene-garnet two-point isochron age (average of 120 ± 5 Ma). Hence, for further discussion, we will adopt the two-point isochron age as representative of the kimberlite emplacement and probably the proto-kimberlite metasomatism (see details below).

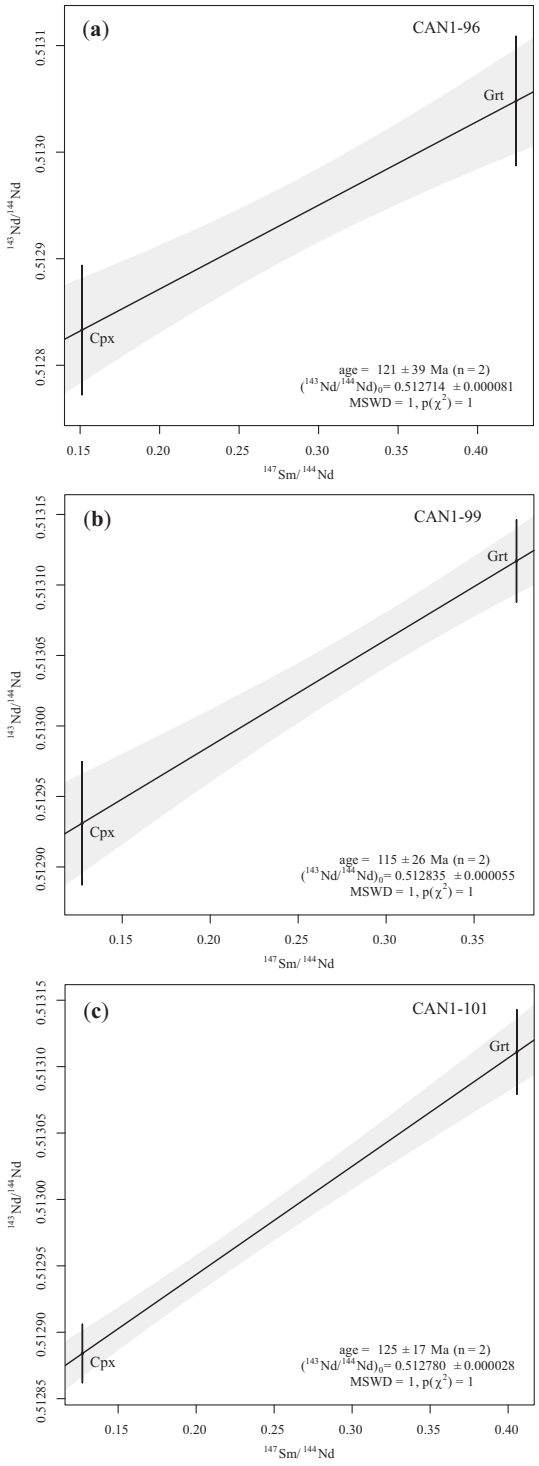

Fig. 14. Two-point clinopyroxene-garnet Sm–Nd isochron ages for sheared lherzolites from Canastra-1 kimberlite, representing the emplacement age of the host kimberlite, which is coeval with the proto-kimberlite metasomatism. The ages are 121 ± 39 Ma (CAN1–96), 115 ± 26 Ma (CAN1–99), and 125 ± 17 Ma (CAN1–101), with average of 120 ± 5 Ma.

DISCUSSION

The subcontinental lithospheric mantle underneath Canastra-1 kimberlite exhibits a complex geological history that may still be recovered based on petrography, mineral chemistry, and geochemistry. Based on the petrographic and chemical evidence, mantle xenoliths from Canastra-1 record cryptic and modal metasomatism (refertilization) (Dawson, 1984). Cryptic metasomatism involves enrichment in incompatible elements with no generation of new phases. In contrast, modal metasomatism leads to the change of the modal mineralogy (and composition) by the growth of new phases (e.g. clinopyroxene, amphibole, and phlogopite). Therefore, the mechanisms responsible for triggering the enrichment of the upper mantle beneath the SW margin of the São Francisco Craton, and their temporal relationship, are discussed below.

Constraining the refertilization in the lithosphere beneath the SW margin of the São Francisco craton

The identification of mantle **eclogites** within Canastra-1 kimberlite represents undoubtable evidence of recycling and metamorphism of an ancient oceanic crust beneath the SW margin of the São Francisco Craton. Eclogites are high-pressure bimineralic rocks, essentially composed of garnet (usually 55%) and omphacite (45%) in subequal proportions, with rutile and ilmenite as the main accessory phases (Jacob, 2004; le Roex *et al.*, 2020). Two origins have been ascribed to eclogite xenoliths hosted by kimberlites in Archean cratonic regions (e.g. Jacob, 2004; Viljoen *et al.*, 2005; Aulbach & Smart, 2023). The first, defined as Group I eclogites, is formed of prograde metamorphism of recycled oceanic crust (basalt or gabbro), with a heterogeneous protolith related to dehydration and partial melting of a mixed subducted oceanic slab with basaltic composition and seafloor sediments. Conversely, Group II eclogites are derived from the crystallization of a small volume of primary mantle melt at high pressure within conduits in old, enriched subcontinental lithosphere. Although eclogite usually has mid-ocean ridge basalt (MORB) protolith, which would confer on its depleted geochemical and isotopic characters, several later metasomatic agents may overprint its original composition (Viljoen *et al.*, 2005). The selected major element diagrams (Mg# vs. Na_2O, CaO, and TiO_2) of clinopyroxenes from Canastra-1 eclogites demonstrate their transitional affinity compared to Groups I and II eclogites from the Kaalvallei Kimberlite, South Africa (Viljoen *et al.*, 2005) (Fig. 7).

Based on the garnet composition, the Canastra-1 eclogites are classified as high-Mg (garnet Mg# = 0.64–0.69) and low-Ca (Ca# = 0.17–0.22, where $Ca\# = Ca/Ca + Mg + Mn + Fe^{+2}$ molar), indicating a less differentiated crustal protolith (Aulbach & Jacob, 2016;Aulbach *et al.*, 2020; Aulbach & Smart, 2023) (Supplementary Fig. S5). According to the Mg# (0.87–0.89) and Na# (0.26–0.27, where Na# = Na/Na + Ca molar) (Fig. S5), clinopyroxenes are defined as eclogitic (Aulbach *et al.*, 2020). These minerals show remarkable cryptic metasomatism during their residence in the cratonic lithospheric mantle, which is evidenced by the pronounced LREE-enrichment (Ce/Yb_N = 60.90–93.63). In contrast, the REE pattern of garnets defines smooth positive slopes from LREE to middle-REE (MREE) ($La/Eu_N < 0.02$) accompanied by less fractionated MREE/HREE ratios (Dy/Lu_N = 0.62–0.64) (Fig. 10g). Hence, clinopyroxene represents the main carrier of the metasomatic signature in Canastra-1 eclogites while garnet maintained its original and unmetasomatized composition (Aulbach *et al.*, 2020).

Based on the modal percentages of the eclogites, the whole-rock compositions for samples CAN1–147 (garnet = 40% and clinopyroxene = 60%) and CAN1–206 (garnet = 48% and clinopyroxene = 52%) were reconstructed. The spoon-like REE pattern of the eclogite whole-rock (La/Sm_N = 1.60–2.06, Dy/Yb_N = 0.71) reinforces the metasomatism ascertained by clinopyroxenes (Fig. S6). The REE pattern of Canastra-1 eclogites is incompatible with undisturbed mantle-derived mafic magmas (i.e. depleted MORB-like composition). Garnets are characterized by 'normal' REE pattern (Fig. 10) but the clinopyroxenes are enriched (Fig. 8), defining an unusual whole-rock composition (Fig. S6). This unexpected REE patterns would be related to the clinopyroxene, which apparently was pervasively generated, as indicated by its spongy (reacted) nature. Although inclusion-rich spongy margins are a common feature observed in all rock types of this study, this texture is more pervasive in eclogites, covering up to 50% of the mineral (Fig. 5b). This texture has been interpreted as evidence for incipient partial melting near to the LAB in the North Atlantic Craton (Kopylova *et al.*, 2019) and Kaapvaal Craton (Tappe *et al.*, 2021).

As the reconstructed whole-rock composition was achieved considering only clinopyroxene and garnet, the negative anomalies of high field strength elements (HFSE) such as Nb-Ta-Ti and Zr-Hf in the PM-normalized multielement diagram are expected, reflecting the absence of rutile and/or ilmenite as a part of the considered mineral assemblage (Aulbach *et al.*, 2007; Aulbach & Stachel, 2022) (Supplementary Fig. S6). In this context, rutile significantly contributes to the Zr (and Hf) budget in eclogites (up to 35%) and controls that of Nb (and Ta) (95–100%). This implies that whole-rock reconstruction without accounting rutile leads to minimum concentrations of these elements and that this deficit is highest at low temperatures where the highest rutile modes are expected (Aulbach *et al.*, 2011; Aulbach, 2020).

The high-Mg (Mg# = 0.46–0.54, MgO = 13.23–14.41 wt %), **Σ**REE (Tb-Lu), and the lack of positive Eu anomalies ($Eu/Eu* = 0.92–0.95$, where $Eu/Eu* = Eu_N/(Sm_N \times Gd_N)^{1/2}$) (Fig. S5) of the Canastra-1 eclogites indicate a more primitive, olivine-rich basaltic protolith ('non-gabbroic'; Aulbach *et al.*, 2007, 2020). In addition, these features, accompanied by the enrichment of LREE and Cr_2O_3 in the reconstructed whole-rocks may suggest the addition of a small volume of a kimberlite-like melt (Aulbach *et al.*, 2020). However, their low concentration of strong mobile elements (i.e. U, and Pb) relative to the ocean crust protolith (White & Klein, 2014), suggest that these elements may have been lost during prograde metamorphism in subduction zones (Fig. S6). An enriched component is further supported by the Sr–Nd isotope compositions of the mineral phases (clinopyroxene and garnet) and whole-rock of eclogites, as indicated by high $^{87}Sr/^{86}Sr$ ratios (clinopyroxene = 0.70842, garnet = 0.70912) and negative ϵNd values (−5.6 to −7.3). Therefore, we suggest that the high-Mg eclogites from Canastra-1 could originate from subducted oceanic crust, which was metasomatized later by fluids/melts liberated from the underlying oceanic mantle (fresh or serpentinized) and overlying sediments (Aulbach et al., 2020; Aulbach & Smart, 2023).

The origin of the olivine-free **hydrated (pargasite-bearing) websterites** from Canastra-1 kimberlite is strongly linked to the high-pressure (>2–3 GPa) cumulates from an evolved (SiO_2-rich) and hydrated basaltic andesitic magma. The reconstructed whole-rock compositions of pargasite websterites were determined using mineral data and point-counted modes (Supplementary Tabs. S1–S6). Compared to the trend defined by the experimental pyroxenite cumulates from hydrous basalt and basaltic andesite (Müntener *et al.*, 2001), our samples plot within the endmembers defined for the higher contents of CaO (>10 wt %), Al_2O_3 (>10 wt %), FeO (>11 wt %), Na_2O (>0.7 wt %), and TiO_2 (>0.4 wt %) at a given MgO content (>15 wt %) (Fig. 15). In general, these major element compositions are similar to those of high-MgO pyroxenite cumulates from Cascades Cordillera (Müntener *et al.*, 2001), NE Tibet (Xiong *et al.*, 2014), Sierra Nevada (Lee *et al.*, 2006), and Southeastern Australia (Lu *et al.*, 2018), which are interpreted as cumulates from mantle wedge-derived hydrous basalt or basaltic andesite (Fig. 15). Comparatively, cumulate pyroxenites from the Cameroon Volcanic Line (Puziewicz *et al.*, 2023) show distinctive composition marked by their higher MgO coupled with lower FeO contents (Fig. 15). Although the pargasite websterites from Canastra-1 would be defined as high-MgO cumulates, their Mg# is low (51–58) due to the enrichment of FeO.

We also have estimated the trace element compositions of melts in equilibrium with the clinopyroxene (Fig. S7). The partition

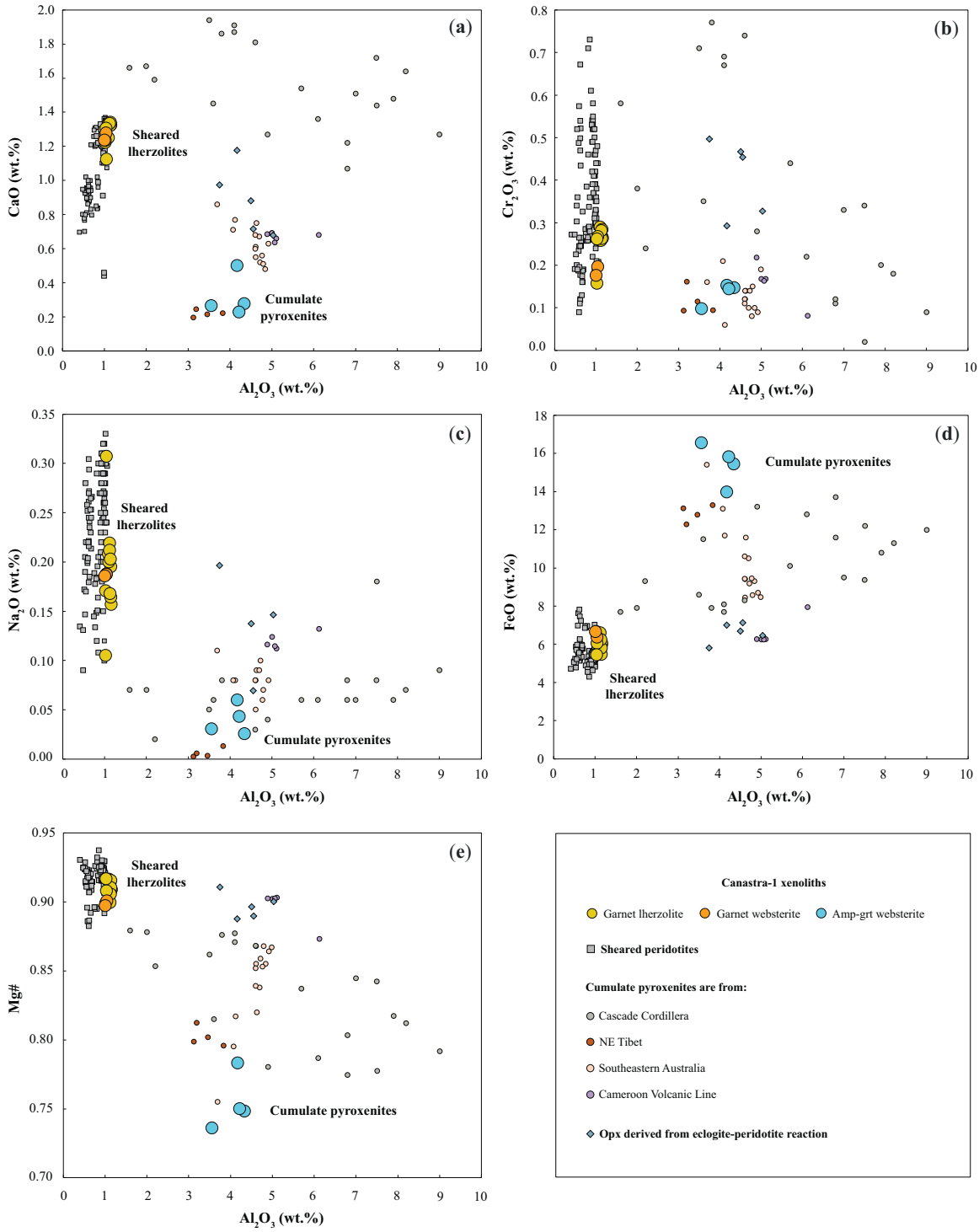

Fig. 15. Selected major elements (CaO, Al_2O_3, FeO, Na_2O, TiO_2, and SiO_2) versus MgO (wt %) showing the compositional affinity of the reconstructed whole-rock pargasite websterites from Canastra-1 with cumulate pyroxenites. For comparison, cumulate pyroxenites from Cascade Cordillera (Müntener *et al.*, 2001), NE Tibet (Xiong *et al.*, 2014), Southeastern Australia (Lu *et al.*, 2018), Cameroon Volcanic Line (Puziewicz *et al.*, 2023), and Sierra Nevada continental arc (Lee *et al.*, 2006) are plotted. High-T sheared peridotites were plotted for comparison (Viljoen *et al.*, 2009; Ionov *et al.*, 2010; Baptiste *et al.*, 2012; Agashev *et al.*, 2013; Kargin *et al.*, 2017; Tappe *et al.*, 2021). The gray line represents the fractional crystallization trend defined by experimentally derived pyroxenite cumulates from hydrous basaltic andesite at 1.2 GPa (Müntener *et al.*, 2001). Fields of pyroxenites from metamorphosed oceanic crust and melt-rock reaction are from Xiong *et al.* (2014).

coefficients used in the calculations are taken from Ionov *et al.* (2002). Calculated melts show trace element pattern typical of arc-related lavas, with strong enrichment of LREE over HREE (i.e. $Ce/Yb_N = 53–253$), and prominent depletion of Nb-Ta-Ti (Fig. S7). The radiogenic isotopes of clinopyroxenes support these results, with pargasite websterites showing enriched $^{87}Sr/^{86}Sr$ (0.70894–0.71003) ratios coupled with negative ϵNd (−12.9 to −13.3) (Fig. 13).

This assumption is supported by the occurrence of Al_2O_3-rich orthopyroxene (~4 wt %), which is considerably higher than those observed in lherzolites and anhydrous websterites (both ~1 wt

%) (Fig. 16). This Al_2O_3-rich orthopyroxene demonstrates strong compositional similarities especially with cumulate pyroxenes from NE Tibet (Xiong *et al.*, 2014) and Southeastern Australia (Lu *et al.*, 2018) (Fig. 16). Clinopyroxenes from pargasite websterites are also enriched in Al_2O_3 (>5 wt %) and CaO (>21 wt %) compared to other Canastra-1 xenoliths (~2 wt % Al_2O_3 and CaO dominantly <18 wt %), corroborating the role of an Al_2O_3-rich melt as the metasomatic agent. Based on the discussion above, we conclude that the pargasite websterites studied here are cumulates from a hydrous basaltic andesite.

In an alternative scenario, the origin of the pargasite websterites from Canastra-1 would be related to mantle hybridization promoted by melt-rock interaction, in which a peridotitic mantle reacted with a hydrous Al- and Si-rich melt potentially formed by melting of eclogites, either in subduction zones or from relicts of subducted crust buried in the mantle. Experimental studies of melt-rock reactions simulating metasomatism of the mantle wedge caused by partial melting of subducted slab have shown that hydrous Al- and Si-rich melts react with peridotite and form a new assemblage composed of orthopyroxene and amphibole. The metasomatic assemblage follows the reaction: $ol + cpx + opx_{(1)} + sp + melt = amp + opx_{(2)}$ (Sen & Dunn, 1994; Rapp *et al.*, 1999; Gervasoni *et al.*, 2017). These studies were conducted at pressures (~2–3 GPa) and temperatures (~900°C), like those assumed here for the pargasite websterites.

However, pyroxenites generated by this process usually inherit the chemical and isotopic compositions from low-P protolith (e.g. depleted gabbro and MORB). Clearly, based on the calculated melt in equilibrium (Fig. S7) and Sr–Nd isotopic results (Supplementary Tab. S5), this is not the case. In general, pyroxenites generated by melt-rock interaction would have higher SiO_2, FeO and TiO_2 but lower Al_2O_3, CaO, and Na_2O contents than those from metamorphosed oceanic crust, which overlap most of the worldwide ('Global') database of pyroxenite cumulates (Lu *et al.*, 2018). Comparatively, pargasite websterites from Canastra-1 display strong affinity with cumulate pyroxenites in terms of CaO, Na_2O, TiO_2, and SiO_2, but with higher FeO and lower Al_2O_3 contents (Fig. 15). Clinopyroxenes and garnets of pargasite websterites from Canastra-1 do not record the 'ghost' effect (positive Eu and Sr anomalies) promoted by a protolith containing plagioclase (Lu *et al.*, 2018 and references therein) (Figs. 8c-d and 10c-d). Besides whole-rock inference, the orthopyroxenes of Canastra-1 pargasite websterites show different compositions than pyroxenites formed by melt-rock reaction. For instance, our orthopyroxenes are characterized by distinctive lower contents of CaO, Cr_2O_3, Na_2O, and Mg# coupled with higher FeO compared to experimental orthopyroxenes product of partial melting from eclogite-peridotite (Gervasoni *et al.*, 2017). Therefore, we preclude the origin of pargasite websterite as related to the melt-rock reaction products. Instead, they are defined as cumulate pyroxenites.

Garnets from eclogites and pargasite websterites plot within the fields defined for mica-amphibole-rutile-ilmenite-diopside (MARID) metasomatism in the Zr–Y diagram (in ppm), that is, related with a hydrated metasomatic agent (Fig. 17a). On the other hand, these garnets show strong affinity with depleted samples in the Ti–Zr diagram (in ppm) (Fig. 17b). Moreover, based on classical diagrams (Ti/Eu vs. La/Yb_N and Sm/Er_N) (Griffin *et al.*, 1999), the compositional distribution of these garnets indicates the interaction of these xenoliths with silicate melt metasomatism, precluding any influence of carbonatite or CO_2-rich metasomatism (Fig. 17c, d). Here it is important to consider that the composition of eclogitic garnet alone cannot reliably constrain the nature of the metasomatic melt. This is because the partitioning of incompatible elements (i.e. LREE) into garnet strongly depends on temperature and grossular content (Aulbach *et al.*, 2020). These authors clearly demonstrate that the decreasing of Ca contents (or Ca#) in garnet is accompanied by the partitioning of LREE into clinopyroxene (see Fig. 2b and d of Aulbach *et al.*, 2020). Regarding our eclogitic garnets, their Ca# is low (0.17–0.22), indicating that these minerals are more susceptible to LREE partitioning. For this reason, LREE-enriched eclogites are characterized by garnets with few, or even non-trace element differences compared to depleted samples. Thus, it is evident that clinopyroxene is the main carrier of the metasomatic signature in LREE-enriched eclogites. This behavior is well-illustrated by enriched clinopyroxenes (Ce/Yb_N = 61–94) and depleted garnets of eclogites from Canastra-1 (Ce/Yb_N = 0.03–0.04). In the same way, Ti and, therefore, Zr concentrations reflect the temperature-dependent solubility of rutile into garnet (Aulbach, 2020). Considering that low-temperature eclogites should contain higher volumes of accessory rutile than high-temperature eclogites, a moderate temperature-dependent Ti solubility in garnet and clinopyroxene is expected for Canastra-1 eclogites (T = 978–982°C). Hence, the deficiency of Nb-Ta-Ti and Zr-Hf observed in the eclogites from Canastra-1 is justified (Supplementary Fig. S6).

Decratonization of the São Francisco Craton caused by lithospheric thinning triggered by high-temperature refertilization at the LAB

The decratonization of the São Francisco Craton was previously discussed based on the rifting mechanism that promoted the orogenic reworking of the limit between the north São Francisco Craton and the Borborema Province, which is a late Neoproterozoic orogen mosaic formed during the amalgamation of Gondwana during the Brasiliano/Pan-African Orogeny (Ganade *et al.*, 2021). These authors combined radiometric data (U–Pb and Sm–Nd model ages) to conclude that the Borborema Province consists of ancient and strongly sheared crustal rocks related to the São Francisco Craton, being separated by major transcurrent shear zones, with small amount of juvenile material during the Neoproterozoic orogeny. Similarly, Neves (2021) discussed an intense process of decratonization and crustal reworking in the Borborema Province during the Brasiliano-Pan-African Orogeny. This author indicates that the recurrent late Paleoproterozoic to early Neoproterozoic extension-related magmatism in the São Francisco Craton differs from the worldwide occurrence of orogenic episodes. In this work, the author suggests that the São Francisco Craton did not participate to the amalgamation of the Columbia supercontinent, its fragmentation, and the Rodinia consolidation. Additional discussion concerning the decratonization of the lithospheric mantle of the São Francisco Craton was given by Caxito & Alkmim (2023), who related this process to the opening (rifting) of V-shaped oceanic basins in the São Francisco-Congo Craton. They also support the hypothesis that this cratonic nucleus represents a single landmass isolated from the Rodinia Supercontinent. Recently, Rodrigues *et al.* (2023) discussed for the first time the effect of pervasive metasomatism/refertilization in a wide mantle column (spinel and garnet facies) beneath Catalão, SW margin of the São Francisco Craton, which resulted in cratonic rejuvenation.

Available geophysical data demonstrate that the São Francisco Craton extends further in depth than its geological boundaries at surface with the neighboring Neoproterozoic Brasília Belt (Pinto *et al.*, 2010; Assumpção *et al.*, 2017; Rocha *et al.*, 2019a, 2019b) (Fig. 1 and Fig. S8). For instance, the Canastra-1 mantle xenoliths have cratonic nature (on-craton) despite the kimberlite being

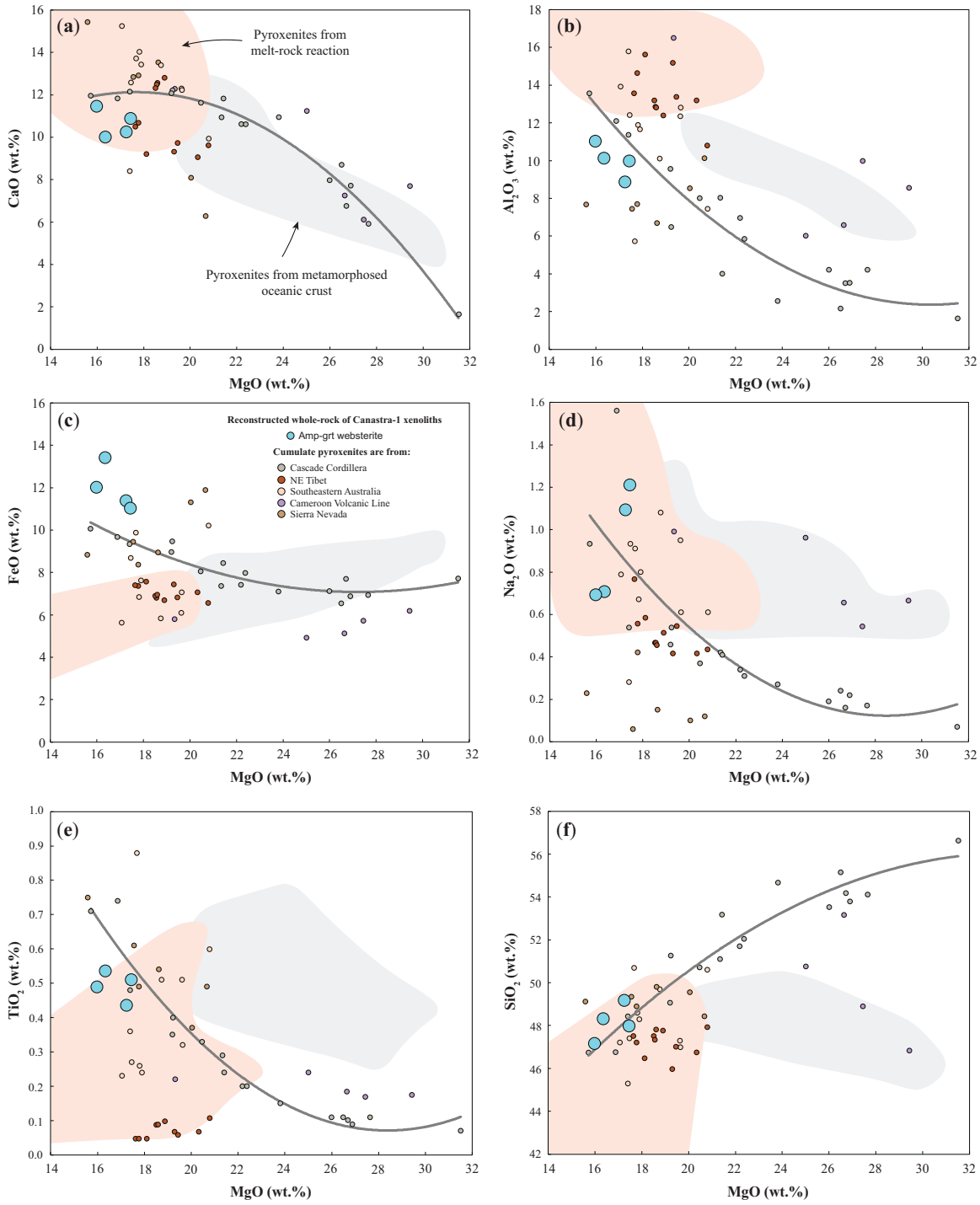

Fig. 16. Selected major elements (CaO, Cr_2O_3, Na_2O, FeO) and Mg# versus Al_2O_3 of orthopyroxenes from Canastra-1 mantle xenoliths. For comparison, orthopyroxenes from cumulate pyroxenites from Cascade Cordillera (Müntener *et al.*, 2001), NE Tibet (Xiong *et al.*, 2014), Southeastern Australia (Lu *et al.*, 2018), and Cameroon Volcanic Line (Puziewicz *et al.*, 2023) are plotted. Experimental orthopyroxenes from peridotite-eclogite reaction also are plotted (Gervasoni *et al.*, 2017).

emplaced in rocks of a Neoproterozoic belt. This feature is commonly observed in the edge of Archean cratons, where the ancient SCLM underlies younger collisional belts demonstrating contemporaneity and a possible genetic link (Lin *et al.*, 2022). Furthermore, geophysical studies indicate that a strong low-velocity seismic anomaly occurs within the lithospheric to asthenospheric mantle from ~100 to 250 km depth (Rocha *et al.*, 2019a, 2019b) (Fig. S8). However, this result needs to be carefully interpreted due to the limited number of seismographic stations in the studied area. Based on the S-wave propagation (Vs), a significant reduction of velocity is recognized at ~150 km depth (Assumpção *et al.*, 2013), which coincides with the current LAB (143 km, Ciardelli *et al.*, 2022). In this region, the Vs is 3.73 km/s (Assumpção *et al.*, 2013), implying a reduction of 17.2% compared to the reference value of 4.75 km/s (Rader *et al.*, 2015). This anomaly appears to be the result of hot asthenospheric upwelling toward the shallower lithospheric mantle in the SW margin of the São Francisco Craton. This process allows the thermo-mechanical erosion of

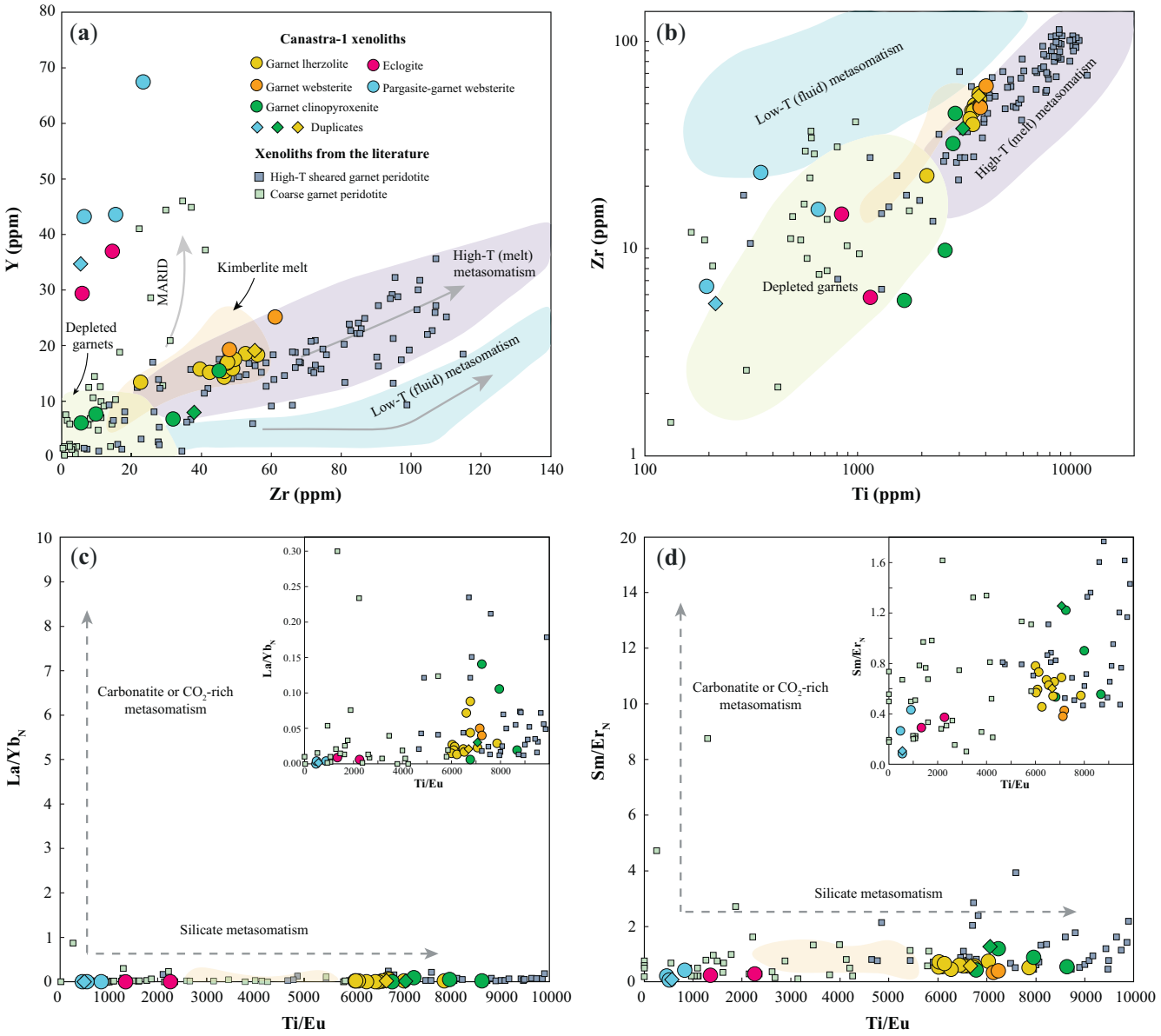

Fig. 17. Variation diagrams of trace elements. (a) Plots of Y versus Zr (ppm); (b) Zr versus Ti (ppm), (c) La/Yb_N (N = PM-normalized) versus Ti/Eu, and (d) Sm/Er_N (N = PM-normalized) versus Ti/Eu of garnets from Canastra-1 kimberlite mantle xenoliths. For comparison, high-T sheared peridotites (Viljoen *et al.*, 2009; Ionov *et al.*, 2010; Agashev *et al.*, 2013; Tappe *et al.*, 2021) and low-T coarse peridotites (Viljoen *et al.*, 2009;Ionov *et al.*, 2010; Kargin *et al.*, 2016; Fitzpayne *et al.*, 2020) from the Siberian, Kaapvaal, and East European cratons were plotted.

the LAB at the base of the cratonic lithosphere through small-scale mantle convections (edge-driven convection) (King & Anderson, 1998; King & Ritsema, 2000; Foley *et al.*, 2008). However, the thermal influence of the Tristan da Cunha mantle plume cannot be excluded, especially due to the two-point Sm–Nd isochron ages (120 ± 5 Ma) obtained for Canastra-1 sheared lherzolites (see details below). In any case, the deformation observed in the sheared lherzolites, anhydrous websterites (and dunite) might have been caused by the intense heating due to Gondwana break-up and the consequent opening of the Atlantic Ocean. Because of such erosion, the lithospheric mantle in the SW limit between the São Francisco Craton and the Paranapanema Block has been rejuvenated by refertilization at least since the Neoproterozoic (Brasiliano Orogeny).

The heating source for the generation of alkaline lavas from the Alto Paranaíba Igneous Province (i.e. kimberlite and kamafugite) has been linked to lithospheric extension and incipient rifting during opening of the South Atlantic Ocean (e.g. Gibson *et al.*, 1995; Read *et al.*, 2004). The relationship between the rift systems and the formation of sheared peridotites is well-documented by sheared garnet-bearing lherzolites from the East African Rift (Henjes-Kunst & Altherr, 1992; Kaeser *et al.*, 2006; Baptiste *et al.*, 2015). These sheared peridotites are associated to deep-seated shear zones near to the LAB, which coincides with the presence of anomalously low-velocity material related to a rift zone. The origin of the high-T sheared garnet-peridotites hosted by kimberlites and equilibrated at pressures ranging from 4.5 to >6.5 GPa was also discussed by Grégoire *et al.* (2006). These authors suggested that although cratonic mantle xenoliths are assumed as lithospheric (O'Reilly & Griffin, 2010), their plastic state when they were captured by the kimberlite magmas suggests that they do not belong to the 'typical' lithospheric mantle but to the underlying 'asthenosphere'. Here it is important to consider that porphyroclastic and mosaic-porphyroclastic

textures cannot be preserved for long periods in the LAB, keeping stable for a short period before the entrainment of xenoliths in the host kimberlite (e.g. Grégoire *et al.*, 2006 and references therein). For this reason, it was defined that sheared peridotites result from plastic deformation at the top of melt pockets due to the high-pressure condition imposed in this tectonic context. Thus, the hot geotherm (40 mW/m^2) defined by sheared lherzolites from Canastra-1 results from strain heating. This heating occurred during the plastic deformation in the early stages of the South Atlantic Ocean opening, shortly predating kimberlite emplacement. This assumption is supported when we compare this geotherm with the intact thick cratonic lithosphere characterized by geotherms corresponding to 35 to 38 mW/m^2 surface heat flow. Further evidence of the effective replacement of the cratonic mantle is the absence of high-Cr_2O_3 coupled with CaO-undersaturated garnets (harzburgitic - G10 garnets, Grütter *et al.*, 2004), as typically observed in intact cratons. It is well-demonstrated in the plot of CaO vs. Cr_2O_3 (in wt %) (Fig. 9, Grütter *et al.*, 2004), which confirms the classification of Canastra-1 mantle xenoliths accordingly.

Advected heat, likely related to kimberlite magmatism (proto-kimberlite melt), generates high-T refertilization and is especially common at the base of the continental lithosphere (Grütter, 2009). Proto-kimberlite melt metasomatism consists of interaction between fluid of kimberlitic affinity with mantle wall rocks at different depths in cratonic regions and that takes place immediately prior to kimberlite entrainment (Giuliani *et al.*, 2013). Therefore, this rejuvenation may be confirmed due to the shallow present-day LAB observed beneath Canastra-1 kimberlite (143 km; Ciardelli *et al.*, 2022). The difference in depth between current and ancient (174–186 km) LABs represents strict evidence of lithospheric thinning produced by the refertilization caused by proto-kimberlite melts from the asthenospheric upwelling (Fig. 12). For this reason, the occurrence of abundant sheared peridotites, anhydrous websterites (and a completely recrystallized dunite) in the LAB beneath Canastra-1 indicates that they are former 'normal' coarse-granular peridotites. It further indicates that these rocks underwent extensive dynamic and static recrystallization, resulting in a bimodal grain size with large porphyroclasts immersed in a fine-grained, strongly deformed neoblastic matrix partially or totally recrystallized (e.g. Boyd & Nixon, 1975; Harte, 1977; Nixon *et al.*, 1981; Baptiste *et al.*, 2012; Agashev *et al.*, 2013; Tappe *et al.*, 2021). In the literature, it is widely accepted that these types of xenoliths are characterized by mosaic-porphyroclastic texture (Harte, 1977) and by high equilibration temperatures (usually between 1000°C and 1300°C) and pressures (usually >4.5 GPa) (i.e. 40–45 mW/m^2 geotherms) (e.g. Harte, 1977; Nixon *et al.*, 1981; Baptiste *et al.*, 2012; Tappe *et al.*, 2021). In general, these deformed rocks have fertile compositions associated with the melt-related metasomatism at the LAB shortly before the kimberlite eruption (e.g. Boyd & Nixon, 1975; Nixon *et al.*, 1981; Kennedy *et al.*, 2002; Grégoire *et al.*, 2006; O'Reilly & Griffin, 2010).

The development of garnet crystals surrounded by kelyphitic rims is a common feature of these xenoliths (Figs. 2f-h; 3a, c; 4a, c; 5a, d; 6b–i), usually containing small crystals of phlogopite, secondary ortho- and clinopyroxenes (types 1 and 2), spinel, rutile, ilmenite, and Fe-Ni sulfides (with absence of olivine or low-pressure phases). Minerals product of alteration, such as serpentine, chlorite, carbonates, or even amphibole and sodalite, were not identified in kelyphitic rims from Canastra-1. Two main mechanisms have been proposed to decipher the origin of kelyphites, which are related to the conditions under which the kelyphite minerals were formed (Sharygin *et al.*, 2023). They are: (1) during xenolith transport to the surface, involving solid-state reaction between garnet and olivine during decompression, or reaction between garnet and kimberlite melt or fluid, and (2) mantle metasomatism promoted under the mantle residence P–T conditions of lherzolite before its entrainment into the ascending kimberlite magma. As reported for the Udachnaya pipe (Siberian Craton) mantle xenoliths (Sharygin *et al.*, 2023), those from Canastra-1 are also fresh (free of secondary alteration). Our mantle xenoliths were sampled from large drill-holes, and they are not in contact with the host kimberlite.

Considering the first scenario, solid-state reaction between garnet and olivine during decompression seems to be improbable due to the lack of compositional zonation among mineral phases within the rock-forming or kelyphitic rims, as well as there is no compositional variation between grains within kelyphite from Canastra-1 (i.e. they are in equilibrium). It is important to note that low-pressure minerals, such as sodalite and amphibole (as reported by Sharygin *et al.*, 2023) were not identified in Canastra-1 mantle xenoliths, precluding the formation of kelyphitic rims through magma ascent. Based on the pressure and temperature estimates of our deeper samples (5.3–5.6 GPa and 1191–1290°C), they plot within the stability field defined for phlogopite instead of amphibole (see Fig. 16a of Sharygin *et al.*, 2023), supporting our interpretation. We also discard the reaction between garnet and kimberlite melt during their ascent to the surface because garnets from Canastra-1 do not show veinlets crosscutting these minerals or contain chemical zonation. In addition, we do not find kelyphite shells covering garnet grains either near the contact with kimberlite or even near the xenolith core, as well as there is no clear evidence of the effective role of a CO_2-rich melt (or carbonatite melt) in the mineral chemistry of garnet. Thus, after comparing our results with those reported by Sharygin *et al.* (2023), we are convinced that kelyphitic rims were formed by metasomatism (high-T proto-kimberlite) at the LAB before xenolith entrainment into the ascending kimberlite magma, as it is no possible to keep this type of texture for a long time in such conditions.

Additional evidence that the kelyphitization process has been triggered under the mantle residence P–T conditions is provided by the lack of significant garnet breakdown based on the occurrence of very fine-grained spinel + orthopyroxene + clinopyroxene symplectites. It is important to note that among all studied samples from Canastra-1, vermicular lamellae of spinel forming a fine-scale pyroxene-spinel symplectite was only observed in sample CAN1–209 (anhydrous websterite). This feature was invoked to exemplify the effective decompression and cooling event and the consequent lithospheric thinning recorded by mantle peridotites of the garnet-spinel transition zone from the Marsabit Volcanic Field (Northern Kenya) (Kaeser *et al.*, 2006). These authors also reported significant chemical zonation that indicates the changing of P–T conditions, deformation, and variable styles of metasomatism, which was not revealed by mantle xenoliths from Canastra-1.

Phlogopites in kelyphitic rims from lherzolite (CAN1–86), clinopyroxenite (CAN1–174), and anhydrous websterite (CAN1–209) are classified as high-Ti-Cr (TiO_2 = 1.29–4.63 wt % and Cr_2O_3 = 0.80–1.91 wt %) due to their close affinity with type 2 phlogopites (Phl2) from proto-kimberlite metasomatism (Kargin *et al.*, 2019) (Fig. 11). However, the analyzed phlogopites show enrichment in FeO implying lower Mg# compared to Phl2 (Fig. 11c-f). According to the relation between TiO_2 and Cr_2O_3 (Fig. 11a), the studied crystals do not have any influence of type 1 phlogopites (Phl1) from mantle xenoliths and kimberlite

xenocrysts (Giuliani *et al.*, 2014, 2016; Kargin *et al.*, 2019) or even of typical kimberlite phlogopites from the groundmass (Fritschle *et al.*, 2013) (Fig. 11). However, except for Cr_2O_3 contents, the xenolithic phlogopites from Canastra-1 and the high-Ti and low-Cr groundmass phlogopites have similar composition (Giuliani *et al.*, 2016; Kargin *et al.*, 2019) (Fig. 11). In this case, it is important to consider the peculiar and complex origin of these high-Ti and low-Cr groundmass phlogopites as they are interpreted as a mixing between magmatic minerals (with high-Ti and low-Cr) and xenocrystic material, including mantle-derived antecrysts (with high-Ti-Cr) (Giuliani *et al.*, 2016; Kargin *et al.*, 2019).

Compared with primary pyroxenes (type 1), both type 2 orthopyroxene and clinopyroxene (secondary) from the kelyphitic rims demonstrate selective enrichment in TiO_2, Cr_2O_3, CaO, and Al_2O_3 accompanied by depletion in Na_2O and Mg# (Supplementary Tables S1–S3). This suggests the role of a common metasomatic agent (proto-kimberlite melt) reacting with the garnet xenocrysts from Canastra-1, which favored the development of kelyphitic rims. In addition, spinel crystals with kimberlite affinity were identified in these kelyphitic rims, as well as rutile and ilmenite that are typical mineral phases found in kimberlites. Therefore, the presence of well-developed kelyphitic halos around garnets from the deep cratonic samples of Canastra-1, with hydrated silicate and oxide minerals rich in Ti and Cr, indicates the interaction of these xenocrysts with the proto-kimberlite melt at mantle depths (e.g. Giuliani *et al.*, 2014, 2016; Bussweiler *et al.*, 2016; Kargin *et al.*, 2019).

The textures of peridotites usually show correlation with the estimated depth of origin and can be grouped into low- and high-temperature peridotites (Boyd & Nixon, 1975). The low-temperature suite is coarse-grained and has depleted composition, whereas the high-temperature peridotites (>1000°C) have deeper origin, a fertile composition, and are deformed in varying degrees from coarse to porphyroclastic and fluidal mosaic textures (Boyd & Nixon, 1975, 1978). The high-T estimates (1191–1290°C) of Canastra-1 xenoliths provide additional evidence of their interaction with a proto-kimberlite melt, reinforced by garnet crystals containing elevated Ti, Zr, and Y concentrations that indicate high-T melt metasomatism (Fig. 17a, b). In these plots (Zr vs. Ti and Y; Fig. 17), they show strong affinity with garnets from high-T sheared peridotites (~1000–1400°C; Fig. 12) from the Siberian, Kaapvaal, and East European cratons (Viljoen *et al.*, 2009; Ionov *et al.*, 2010; Agashev *et al.*, 2013; Tappe *et al.*, 2021). Conversely, low-T coarse-grained peridotites from the cratonic areas mentioned above (Viljoen *et al.*, 2009;Ionov *et al.*, 2010; Kargin *et al.*, 2016; Fitzpayne *et al.*, 2020) clearly show different distribution patterns than Canastra-1 lherzolites, clinopyroxenites, and anhydrous websterites (Fig. 17). In addition, according to the Ti/Eu vs. La/Yb_N and Sm/Er_N diagrams, the garnets from these Canastra-1 xenoliths interacted with a high-T silicate melt, as they fall within the high-T sheared peridotites (Fig. 17c, d).

Clinopyroxenes endorse the dominance of a high-T silicate melt (proto-kimberlite) at the LAB beneath the SW margin of the São Francisco Craton through the Ti/Eu vs. La/Yb_N and Sr, and by Zr/Hf vs. Ti/Nb (Fig. S9). Besides all clinopyroxenes plotting close to the typical enrichment trend proposed for silicate melt, they have strong affinity with clinopyroxenes of high-T sheared peridotites (Ionov *et al.*, 2010; Agashev *et al.*, 2013; Kargin *et al.*, 2017; Tappe *et al.*, 2021). It is interesting that, in general, the typical compositional trends proposed for silicate and carbonatite melts coincide, respectively, with the high-T sheared and low-T coarse-grained peridotites (Ionov *et al.*, 2010; Kargin *et al.*, 2016; Fitzpayne *et al.*, 2020) (Fig. S9a, b). It is important to emphasize that although lherzolites, anhydrous websterites, and clinopyroxenites have high Ca/Al ratios (7.56–10.69) (Supplementary Tables S1 and S2), which would be indicative of carbonatite metasomatism, the diagrams above exclude any evidence of this type of metasomatism (Fig. S9). In the Mg# vs. Na_2O, CaO, and TiO_2 diagrams (Fig. 7), clinopyroxenes from lherzolites and anhydrous websterites fall within the compositional field of high-T sheared peridotites similar to those from the Siberian (Ionov *et al.*, 2010; Agashev *et al.*, 2013), Kaapvaal (Viljoen *et al.*, 2009; Baptiste *et al.*, 2012; Fitzpayne *et al.*, 2020; Tappe *et al.*, 2021), and East European (Kargin *et al.*, 2017) cratons.

Regarding the anhydrous websterites, their SiO_2-rich composition is defined by the large modal content of pyroxenes (ortho- and clinopyroxenes). For this reason, the genesis of this rock type cannot be explained by crystallization from kimberlite or silica-poor melts (Rehfeldt *et al.*, 2008). Thus, they are formed by reaction between peridotite and silica-rich melt (>60 wt % SiO_2) derived by partial melting of eclogite, which implies the conversion of olivine into orthopyroxene (Rehfeldt *et al.*, 2008). Alternatively, the origin of olivine-free anhydrous websterites can be attributed to the interaction between mantle xenoliths with a H_2O-poor, alkaline silicate melt that triggered the formation of orthopyroxene at the expense of clinopyroxene (Koornneef *et al.*, 2009). Considering the context of the cratonic LAB beneath Canastra-1, we propose that the infiltration of a proto-kimberlite melt (~120 Ma) would favor the localized partial melting of an eclogitized subducted oceanic crust that induces the formation of orthopyroxene-rich lithologies (Kelemen *et al.*, 1992; Rehfeldt *et al.*, 2008; Koornneef *et al.*, 2009). Rudnick *et al.* (1994) proposed a similar process to explain the orthopyroxene enrichment in Kaapvaal peridotites. In our set of samples, CAN1–209 is a good example of this reaction process with 78% orthopyroxene (Supplementary Tab. S6).

The Canastra-1 clinopyroxenites appear to represent a mafic eclogite protolith that was destabilized at the base of the cratonic lithosphere through the interaction with proto-kimberlite melt in a system containing insufficient Na_2O (i.e. low modal plagioclase) to allow the formation of omphacitic pyroxene (le Roex *et al.*, 2020).

Considering the Sr–Nd isotopic ratios of clinopyroxenes and garnets from lherzolites and clinopyroxenites, these samples show selective enrichment of Sr ($^{87}Sr/^{86}Sr = 0.70560–0.70869$) at intermediate to high Nd isotopic ratios ($^{143}Nd/^{144}Nd = 0.51273–0.51315$; $\epsilon Nd = +1.8$ to $+10.10$) (Fig. 13). The Nd results of whole-rocks ($^{143}Nd/^{144}Nd = 0.51277–0.51292$, $\epsilon Nd = +2.5$ to $+5.6$) are consistent with those from their minerals. Although less scattered and with slightly lower Nd ratios, this distribution pattern is similar to that observed in the garnet xenocrysts from the Carolina kimberlite, Amazonian Craton (Gervasoni *et al.*, 2022) (Fig. 13). This behavior is explained by the high incompatibility (and mobility) of Sr compared to Nd, which confer a sensitive character to Sr isotopic ratios, susceptible to perturbation that increases $^{87}Sr/^{86}Sr$ values while $^{143}Nd/^{144}Nd$ isotopic ratios remain constant.

Although there are no details about the method and material employed to determine the emplacement age of the Canastra-1 kimberlite, the only available age is Cretaceous (120 Ma, Read *et al.*, 2004). Therefore, based on the Sr–Nd isotopic compositions, as well as on the Sm–Nd isochron ages (average of 120 ± 5 Ma), it is assumed that lherzolites, clinopyroxenites, and anhydrous websterites (although there are no isotopic data for the latter) record the isotopic equilibrium at the time of the proto-kimberlite melt percolation and refertilization at the LAB beneath the São Francisco Craton, which precedes the subsequent eruption of the

Canastra-1 host kimberlite. It is important to observe that this premise is plausible due to the higher equilibrium temperatures of these xenoliths (1191–1290°C) compared to the closure temperature for the Sm–Nd system in clinopyroxene (1000–1150°C) and garnet (750–900°C) (Ganguly & Tirone, 1999; Van Orman *et al.*, 2001, 2002). Hence, the two-point Sm–Nd isochrons constructed based on clinopyroxenes and garnets from sheared lherzolites (Fig. 14) represent cooling/emplacement ages that are product of proto-kimberlite melt metasomatism, as similarly proposed by Gervasoni *et al.* (2022) for Carolina mantle xenoliths.

CONCLUSION

Mantle xenoliths hosted by the Canastra-1 kimberlite, exposed in the SW edge of the São Francisco Craton, are equilibrated within the garnet stability field. Sheared lherzolites, granuloblastic dunite, coarse clinopyroxenites and anhydrous websterites are deeper xenoliths from the lithosphere-asthenosphere boundary. On the other hand, eclogites and pargasite websterites are representative of the shallower cratonic lithosphere.

The deeper xenoliths are characterized by high-T estimates (1191–1290°C) and were affected by metasomatism near the LAB shortly before the eruption of the host kimberlite (174–186 km). The high-T proto-kimberlite melt metasomatism is corroborated by strong compositional affinity with high-T sheared peridotites from other cratons worldwide (i.e. Siberian, North Atlantic, Kaapvaal, and East European). This metasomatism is exemplified by high Ti, Zr, and Y concentrations in garnets, as well as by clinopyroxene selected major (e.g. Mg# vs. Na_2O, CaO, and TiO_2) and trace elements (e.g. Ti/Eu vs. La/Yb_N and Sr; $Ce/Yb_N = 12.06–48.02$). Well-developed kelyphitic rims reinforce the interaction between garnet and proto-kimberlite metasomatic agent. Isotopically, they display selective enrichment of $^{87}Sr/^{86}Sr$ (0.70560–0.70869) coupled with intermediate to high Nd isotopic ratios ($\epsilon Nd = +1.8$ to $+10.10$). The two-point Sm–Nd isochron age average obtained considering clinopyroxene and garnet from sheared lherzolites is 120 ± 5 Ma, which records the percolation of a proto-kimberlite melt into the LAB beneath the São Francisco Craton immediately before the eruption of the Canastra-1 kimberlite. This refertilization event is coeval with the early stages of the Gondwana breakup and the opening of the Atlantic Ocean. In this tectonic context, lithospheric thinning, extensive extensional deformation, and intense thermal activity are common.

Eclogites are classified as high-Mg (garnet Mg# = 0.64–0.69) and low-Ca (garnet Ca# = 0.17–0.22), and demonstrate transitional affinity between Groups I and II eclogites. These xenoliths represent a more primitive, olivine-rich basaltic protolith within the shallower cratonic lithosphere beneath Canastra-1 (~130 km). Eclogitic clinopyroxene shows cryptic metasomatism ($Ce/Yb_N = 60.90–93.63$), reinforced by the spoon-like REE pattern of reconstructed whole-rock. On the other hand, eclogitic garnet maintained its depleted character based on REEs ($Ce/Yb_N < 0.32$). The Sr–Nd isotope composition of eclogite suggests the role of an enriched component ($^{87}Sr/^{86}Sr$ clinopyroxene = 0.70842, garnet = 0.70912; $\epsilon Nd = -5.6$ to -7.3).

The partial melting of ancient oceanic slab fragments, which generates SiO_2- and Al_2O_3-rich hydrous melts, favored the formation of pyroxenite cumulates exemplified by olivine-free pargasite websterites. This is mainly corroborated by the Al-rich orthopyroxene and reconstructed whole-rock compositions ($Al_2O_3 = 3.55–4.34$ and 8.88–11.03 wt %, respectively), low Mg# of orthopyroxene and reconstructed whole-rock (0.74–0.78 and 0.51–0.58, respectively), and the formation of pargasite. These samples also evidence cryptic metasomatism as shown by LREE-enriched clinopyroxenes ($Ce/Yb_N = 10.52–50.61$), as well as by high-Sr isotopic ratios ($^{87}Sr/^{86}Sr$ clinopyroxene = 0.70894–0.71003) and pronounced negative ϵNd values (-12.9 to -13.3). Although we do not achieved chronological ages for eclogites and pargasite websterites, we attribute their formations to the Gondwana amalgamation in the Neoproterozoic (Brasiliano Orogeny).

Supplementary Data

Supplementary data are available at Journal of Petrology online.

Acknowledgements

We thank Débora Araujo for sharing unpublished data and Giuliana Costa for providing additional rock samples. R.A.F. thanks CNPq for the research fellowship. INCT Estudos Tectônicos (CNPq, CAPES, FAPDF) is acknowledged for financial support. T.G. and M.M. thank FAR Dipartimentale 2023 of the Università di Modena e Reggio Emilia. We are grateful for the significant and valuable contributions provided by the reviewers, Prof. Sonja Aulbach, Prof. Michel Grégoire, and Prof. Sebastian Tappe.

Funding

This study was financed in part by the Coordenação de Aperfeiçoamento de Pessoal de Nível Superior - Brasil (CAPES) - Finance Code 001 and by the Serrapilheira Institute research project [grant number Serra-1709-18152]. CAPES also supported this research through the PhD scholarship [grant number 88887.479521/2020-00 to L.G.B.].

Data Availability

The data underlying this article are available in the article and in its online supplementary material.

REFERENCES

Affonso, G. M. P. C., Rocha, M. P., Costa, I. S. L., Assumpção, M., Fuck, R. A., Albuquerque, D. F., Portner, D. E., Rodríguez, E. E. & Beck, S. L. (2021). Lithospheric architecture of the Paranapanema block and adjacent nuclei using multiple-frequency P-wave seismic tomography. *Journal of Geophysical Research: Solid Earth* **126**(4), 1–19. https://doi.org/10.1029/2020JB021183.

Agashev, A. M., Ionov, D. A., Pokhilenko, N. P., Golovin, A. V., Cherepanova, Y. & Sharygin, I. S. (2013). Metasomatism in lithospheric mantle roots: constraints from whole-rock and mineral chemical composition of deformed peridotite xenoliths from kimberlite pipe Udachnaya. *Lithos* **160-161**, 201–215. https://doi.org/10.1016/j.lithos.2012.11.014.

Alkmim, F. F. & Teixeira, W. (2017) The Paleoproterozoic Mineiro Belt and the Quadrilátero Ferrífero. In: Heilbron M., Cordani U. & Alkmim F. (eds) *São Francisco Craton, Eastern Brazil*. Springer, Cham: Regional Geology Reviews, pp.71–94.

Almeida, F. F. M., Hasui, Y., Brito Neves, B. B. & Fuck, R. A. (1981). Brazilian structural provinces: an introduction. *Earth-Science Reviews* **17**, 1–29. https://doi.org/10.1016/0012-8252(81)90003-9.

Almeida, V. V., Janasi, V. A., Svisero, D. P. & Nannini, F. (2014). Mathiasite–loveringite and priderite in mantle xenoliths from the alto Paranaíba Igneous Province, Brazil: genesis and constraints on mantle metasomatism. *Central European Journal of Geosciences* **6**, 614–632. https://doi.org/10.2478/s13533-012-0197-5.

Almeida, V. V., Rodrigues, J. B., Cabral Neto, I., Silveira, F. V. & Silva, H. B. (2022). Composition and P-T conditions of the lithospheric mantle beneath the Azimuth 125° lineament, Northern and Southeastern Brazil: constraints from peridotite xenoliths enclosed in diamond-bearing kimberlites. *Journal of the Geological Survey of Brazil* **5**(3), 177–203. https://doi.org/10.29396/jgsb.2022.v5.n3.2.

Araujo, A. L. N., Carlson, R. W., Gaspar, J. C. & Bizzi, L. A. (2001). Petrology of kamafugites and kimberlites from the alto Paranaíba Alkaline Province, Minas Gerais, Brazil. *Contributions to Mineralogy and Petrology* **142**, 163–177. https://doi.org/10.1007/s004100100280.

Assumpção, M., Feng, M., Tassara, A. & Julià, J. (2013). Models of crustal thickness for South America from seismic refraction, receiver functions and surface wave tomography. *Tectonophysics* **609**, 82–96. https://doi.org/10.1016/j.tecto.2012.11.014.

Assumpção, M., Azevedo, P. A., Rocha, M. P. & Bianchi, M. B. (2017) Lithospheric Features of the São Francisco Craton. Tectonic genealogy of a miniature continent. In: Heilbron, M., Cordani, U., Alkmim, F. (eds) *São Francisco Craton, Eastern Brazil*. Regional Geology Reviews. New York: Springer Berlin Heidelberg, Cham. pp.15–25.

Aulbach, S. (2018) Cratonic Lithosphere Discontinuities: Dynamics of Small-Volume Melting, Metacratonization, and a Possible Role for Brines. In: Yuan H. & Romanowicz B. (eds) *Lithospheric Discontinuities, Geophysical Monograph Series, 239*. Hoboken: John Wiley & Sons; Washington: American Geophysical Union, pp.177–203.

Aulbach, S. (2020). Temperature-dependent rutile solubility in garnet and clinopyroxene from mantle Eclogite: implications for continental crust formation and V-based oxybarometry. *Journal of Petrology* **61**(6), egaa065. https://doi.org/10.1093/petrology/egaa065.

Aulbach, S. & Jacob, D. E. (2016). Major- and trace-elements in cratonic mantle eclogites and pyroxenites reveal heterogeneous sources and metamorphic processing of low-pressure protoliths. *Lithos* **262**, 586–605. https://doi.org/10.1016/j.lithos.2016.07.026.

Aulbach, S. & Smart, K. A. (2023). Petrogenesis and geodynamic significance of Xenolithic Eclogites. *Annual Review of Earth and Planetary Sciences* **51**, 521–549. https://doi.org/10.1146/annurev-earth-031621-112904.

Aulbach, S. & Stachel, T. (2022). Evidence for oxygen-conserving diamond formation in redox-buffered subducted oceanic crust sampled as eclogite. *Nature Communications* **13**, 1924. https://doi.org/10.1038/s41467-022-29567-z.

Aulbach, S., Pearson, N. J., Reilly, S. Y. O. & Doyle, B. J. (2007). Origins of xenolithic eclogites and pyroxenites from the central Slave Craton, Canada. *Journal of Petrology* **48**, 1843–1873. https://doi.org/10.1093/petrology/egm041.

Aulbach, S., O'Reilly, S. Y. & Pearson, G. (2011). Constraints from eclogite and MARID xenoliths on origins of mantle Zr/Hf–Nb/Ta variability. *Contributions to Mineralogy and Petrology* **162**, 1047–1062. https://doi.org/10.1007/s00410-011-0639-y.

Aulbach, S., Griffin, W. L., Pearson, N. J. & O'Reilly, S. Y. (2013). Nature and timing of metasomatism in the stratified mantle lithosphere beneath the central Slave Craton (Canada). *Chemical Geology* **352**, 153–169. https://doi.org/10.1016/j.chemgeo.2013.05.037.

Aulbach, S., Massuyeau, M., Garber, J. M., Gerdes, A., Heaman, L. M. & Viljoen, K. S. (2020). Ultramafic carbonated melt- and auto-metasomatism in mantle eclogites: compositional effects and geophysical consequences. *Geochemistry, Geophysics, Geosystems* **21**, e2019GC008774. https://doi.org/10.1029/2019GC008774.

Azzone, R. G., Pearson, D. G., Sarkar, C., Chmyz, L., Shibata, C. S. V., Luo, Y. & Ruberti, E. (2022). Tracking crustal assimilation processes in kimberlites from the Alto Paranaíba Igneous Province, Brazil: petrographic and geochemical controls and the role of perovskites. *Lithos*, 432–433. https://doi.org/10.1016/j.lithos.2022.106888.

Baptiste, V., Tommasi, A. & Demouchy, S. (2012). Deformation and hydration of the lithospheric mantle beneath the Kaapvaal craton, South Africa. *Lithos* **149**, 31–50. https://doi.org/10.1016/j.lithos.2012.05.001.

Baptiste, V., Tommasi, A., Vauchez, A., Demouchy, S. & Rudnick, R. L. (2015). Deformation, hydration, and anisotropy of the lithospheric mantle in an active rift: constraints from mantle xenoliths from the North Tanzanian Divergence of the East African Rift. *Tectonophysics* **639**, 34–55. https://doi.org/10.1016/j.tecto.2014.11.011.

Barbosa, J. S. F. & Barbosa, R. G. (2017) The Paleoproterozoic Eastern Bahia Orogenic Domain. In: Heilbron M., Cordani U. & Alkmim F. (eds) *São Francisco Craton, Eastern Brazil: Tectonic Genealogy of a Miniature Continent*. Cham: Springer International Publishing, pp. 57–69.

Becker, M. & le Roex, A. P. (2006). Geochemistry of South African on- and off- craton, Group I and Group II kimberlites: petrogenesis and source region evolution. *Journal of Petrology* **47**(4), 673–703. https://doi.org/10.1093/petrology/egi089.

Becker, M., le Roex, A. P. & Class, C. (2007). Geochemistry and petrogenesis of South African transitional kimberlites located on and off the Kaapvaal Craton. *South African Journal of Geology* **110**(4), 631–646. https://doi.org/10.2113/gssajg.110.4.631.

Beyer, C., Frost, D. J. & Miyajima, N. (2015). Experimental calibration of a garnet–clinopyroxene geobarometer for mantle eclogites. *Contributions to Mineralogy and Petrology* **169**, 18. https://doi.org/10.1007/s00410-015-1113-z.

Boyd, F. R. & Nixon, P. H. (1975). Origins of the ultramafc nodules from some kimberlites of northern Lesotho and the Monastery mine, South Africa. *Physics and Chemistry of the Earth* , 431–454. https://doi.org/10.1016/B978-0-08-018017-5.50035-3.

Boyd, F. R. & Nixon, P. H. (1978). Ultramafc nodules from the Kimberley pipes, South Africa. *Geochimica et Cosmochimica Acta* **42**(9), 1367–1382. https://doi.org/10.1016/0016-7037(78)90042-X.

Brey, G. P. & Koehler, T. (1990). Geothermobarometry in four-phase lherzolites II. New thermobarometers, and practical assessment of existing thermobarometers. *Journal of Petrology* **31**(6), 1353–1378. https://doi.org/10.1093/petrology/31.6.1353.

Bussweiler, Y., Stone, R. S., Pearson, D. G., Luth, R. W., Stachel, T., Kjarsgaard, B. A. & Menzies, A. (2016). The evolution of calcite-bearing kimberlites by melt-rock reaction: evidence from polymineralic inclusions within clinopyroxene and garnet megacrysts from lac de Gras kimberlites, Canada. *Canada Contributions to Mineralogy and Petrology* **171**, 65. https://doi.org/10.1007/s00410-016-1275-3.

Cabral Neto, I., Nannini, F., Silveira, F. V. & Cunha, L. M. (2017) *Áreas kimberlíticas e diamantíferas do Estado de Minas Gerais: Informe de Recursos Minerais Complementar ao Mapa das áreas Kimberlíticas e Diamantíferas do Estado de Minas Gerais e Regiões Adjacentes*. Brasília: Serviço Geológico do Brasil, p.230.

Carlson, R. W., Irving, A. J., Schulze, D. J. & Hearn, B. C., Jr. (2004). Timing of Precambrian melt depletion and Phanerozoic refertilization events in the lithospheric mantle of the Wyoming Craton and adjacent Central Plains Orogen. *Lithos* **77**, 453–472. https://doi.org/10.1016/j.lithos.2004.03.030.

Carlson, R. W., Araújo, A. L. N., Junqueira-Brod, T. C., Gaspar, J. C., Brod, J. A., Petrinovic, I. A., Hollanda, M. H. B. M., Pimentel, M. M. & Sichel, S. (2007). Chemical and isotopic relationships between peridotite xenoliths and mafic–ultrapotassic rocks from Southern Brazil. *Chemical Geology* **242**, 415–434. https://doi.org/10.1016/j.chemgeo.2007.04.009.

Carvalho, J. B. (1997) *Petrologia dos xenólitos mantélicos da Província do Alto Paranaíba*PhD thesis. Brazil: Universidade de Brasília, p.395 in Portuguese.

Carvalho, L. D. V., Stachel, T., Pearson, D. G., Fuck, R. A., Jalowitzki, T., Timmermann, S., Steale-Macinnis, M., Gonçalves, G. O., Pereira, R. S. & Scholz, R. (2022a). Diamond formation beneath the Coromandel area, southwestern São Francisco Craton—the role of refertilization and subduction. *Lithos* **430-431**, 106856. https://doi.org/10.1016/j.lithos.2022.106856.

Carvalho, L. D. V., Jalowitzki, T., Scholz, R., Gonçalves, G. O., Rocha, M. P., Pereira, R. S., Lana, C., Castro, M. P., Queiroga, G. & Fuck, R. A. (2022b). An exotic cretaceous kimberlite linked to metasomatized lithospheric mantle beneath the southwestern margin of the São Francisco Craton, Brazil. *Geoscience Frontiers* **13**, 101281. https://doi.org/10.1016/j.gsf.2021.101281.

Caxito, F. A. & Alkmim, F. F. (2023). The role of V-shaped oceans and ribbon continents in the Brasiliano/PanAfrican assembly of western Gondwana. *Scientific Reports* **13**, 1568. https://doi.org/10.1038/s41598-023-28717-7.

Ciardelli, C., Assumpção, M., Bozdağ, E. & Van der Lee, S. (2022). Adjoint waveform tomography of South America. *Journal of Geophysical Research: Solid Earth* **127**(2). https://doi.org/10.1029/2021JB022575.

Coe, N., le Roex, A., Gurney, J., Graham Pearson, D. & Nowell, G. (2008). Petrogenesis of the Swartruggens and Star Group II kimberlite dyke swarms, South Africa: constraints from whole rock geochemistry. *Contributions to Mineralogy and Petrology* **156**, 627–652. https://doi.org/10.1007/s00410-008-0305-1.

Coldebella, B., Azzone, R. G., Chmyz, L., Ruberti, E. & Svisero, D. P. (2020). Oxygen fugacity of Alto Paranaíba kimberlites and diamond instability: Três Ranchos IV and Limeira I intrusions. *Brazilian Journal of Geology* **50**(1), 1–15. https://doi.org/10.1590/2317-4889202020190087.

Cordani, U. G., Pimentel, M. M., de Araújo, C. E. G. & Fuck, R. A. (2013). The significance of the Transbrasiliano-Kandi tectonic corridor for the amalgamation of West Gondwana. *Brazilian Journal of Geology* **43**(3), 583–597. https://doi.org/10.5327/Z2317-48892013000300012.

Costa, G. V. (2008) *Química mineral e geotermobarometria de xenólitos mantélicos do kimberlito Canastra-01*Master thesis. Brazil: Universidade de Brasília, p.137 (in Portuguese).

Costa, M. M. (2012) *Petrografia e geoquímica isotópica de Sm–Nd em xenólitos mantélicos do kimberlito Canastra-01*Master thesis. Brazil: Universidade de Brasília, p.125 (in Portuguese).

Dawson, J. B. (1984) Contrasting types of upper mantle metasomatism. In: Kornprobst J. (ed) *Kimberlites II: the Mantle and Crust-Mantle Relationships*. Amsterdam: Elsevier, pp.289–294.

Dessai, A. G., Viegas, A. & Griffin, W. L. (2021). Thermal architecture of cratonic India and implications for decratonization of the Western Dharwar Craton: evidence from mantle xenoliths in the Deccan Traps. *Lithos* **382–383**, 105927. https://doi.org/10.1016/j.lithos.2020.105927.

Donatti-Filho, J. P., Tappe, S., Oliveira, E. P. & Heaman, L. M. (2013). Age and origin of the Neoproterozoic Brauna kimberlites: melt generation within the metasomatized base of the São Francisco Craton, Brazil. *Chemical Geology* **353**, 19–35. https://doi.org/10.1016/j.chemgeo.2012.06.004.

Downes, H., MacDonald, R., Upton, B. G. J., Cox, K. G., Bodinier, J.-L., Mason, P. R. D., James, D., Hill, P. G. & Hearn, B. C., Jr. (2004). Ultramafic xenoliths from the Bearpaw Mountains, Montana, USA: evidence for multiple metasomatic events in the lithospheric mantle beneath the Wyoming Craton. *Journal of Petrology* **45**(8), 1631–1662. https://doi.org/10.1093/petrology/egh027.

Felgate, M. R. (2014) *The Petrogenesis of Brazilian kimberlites and kamafugites intruded along the 125° lineament: improved geochemical and geochronological constraints on magmatism in Rondonia and the Alto Paranaiba Igneous Province*PhD thesis. Australia: The University of Melbourne, p.275.

Fernandes, P. R., Tommasi, A., Vauchez, A., Neves, S. P. & Nannini, F. (2021). The São Francisco cratonic root beneath the Neoproterozoic Brasilia belt (Brazil): petrophysical data from kimberlite xenoliths. *Tectonophysics* **816**, 229011. https://doi.org/10.1016/j.tecto.2021.229011.

Fitzpayne, A., Giuliani, A., Phillips, D., Hergt, J., Woodhead, J. D., Farquhar, J., Fiorentini, M. L., Drysdale, R. N. & Wu, N. (2018). Kimberlite-related metasomatism recorded in MARID and PIC mantle xenoliths. *Mineralogy and Petrology* **112**, 71–84. https://doi.org/10.1007/s00710-018-0573-z.

Fitzpayne, A., Giuliani, A., Maas, R., Hergt, J., Janney, P. & Phillips, D. (2019). Progressive metasomatism of the mantle by kimberlite melts: Sr–Nd–Hf–Pb isotope compositions of MARID and PIC minerals. *Earth and Planetary Science Letters* **509**, 15–26. https://doi.org/10.1016/j.epsl.2018.12.013.

Fitzpayne, A., Giuliani, A., Hergt, J., Woodhead, J. D. & Mass, R. (2020). Isotopic analyses of clinopyroxenes demonstrate the effects of kimberlite melt metasomatism upon the lithospheric mantle. *Lithos* **370–371**, 105595. https://doi.org/10.1016/j.lithos.2020.105595.

Foley, S. (1992). Petrological characterization of the source components of potassic magmas: geochemical and experimental constraints. *Lithos* **28**, 187–204. https://doi.org/10.1016/0024-4937(92)90006-K.

Foley, S. (2008). Rejuvenation and erosion of the cratonic lithosphere. *Nature Geoscience* **1**, 503–510. https://doi.org/10.1038/ngeo261.

Fritschle, T., Prelević, D., Foley, S. F. & Jacob, D. E. (2013). Petrological characterization of the mantle source of Mediterranean lamproites: indications from major and trace elements of phlogopite. *Chemical Geology* **353**, 267–279. https://doi.org/10.1016/j.chemgeo.2012.09.006.

Frugis, G. L., Campos Neto, M. D. C. & Lima, R. B. (2018). Eastern Paranapanema and southern São Francisco orogenic margins: records of enduring Neoproterozoic oceanic convergence and collision in the southern Brasília Orogen. *Precambrian Research* **308**, 35–57. https://doi.org/10.1016/j.precamres.2018.02.005.

Fuck, R. A., Pimentel, M. M., Alvarenga, C. J. S. & Dantas, E. L. (2017) *The Northern Brasília Belt*. In: Heilbron M., Cordani U. & Alkmim F. (eds) *São Francisco Craton, Eastern Brazil*. Cham: Springer International Publishing.

Ganade, C. E., Weinberg, R. F., Caxito, F. A., Lopes, L. B., Tesser, L. R. & Costa, I. S. (2021). Decratonization by rifting enables orogenic reworking and transcurrent dispersal of old terranes in NE Brazil. *Scientific Reports* **11**, 5719. https://doi.org/10.1038/s41598-021-84703-x.

Ganguly, J. & Tirone, M. (1999). Diffusion closure temperature and age of a mineral with arbitrary extent of diffusion: theoretical formulation and applications. *Earth and Planetary Science Letters* **170**, 131–140. https://doi.org/10.1016/S0012-821X(99)00089-8.

Gervasoni, F., Klemme, S., Rohrbach, A., Grützner, T. & Berndt, J. (2017). Experimental constraints on mantle metasomatism caused by silicate and carbonate melts. *Lithos* **282–283**, 173–186. https://doi.org/10.1016/j.lithos.2017.03.004.

Gervasoni, F., Jalowitzki, T., Rocha, M. P., Weska, R. K., Novais-Rodrigues, E., Rodrigues, R. A. F., Bussweiler, Y., Barbosa, E. S. R., Berndt, J., Dantas, E. L., Souza, V. S. & Klemme, S. (2022). Recycling process and proto-kimberlite melt metasomatism in the lithosphere-asthenosphere boundary beneath the Amazonian

Craton recorded by garnet xenocrysts and mantle xenoliths from the Carolina kimberlite. *Geoscience Frontiers* **13**, 101429. https://doi.org/10.1016/j.gsf.2022.101429.

Gibson, S. A., Thompson, R. N., Leonardos, O. H., Dickin, A. P. & Mitchell, J. G. (1995). The late cretaceous impact of the Trindade mantle plume: evidence from large volume, mafic, postassic magmatism in SE Brazil. *Journal of Petrology* **36**, 189–229. https://doi.org/10.1093/petrology/36.1.189.

Gioia, S. M. C. L. & Pimentel, M. M. (2000). The Sm–Nd isotopic method in the geochronology laboratory of the University of Brasília. *Anais da Academia Brasileira de Ciências* **72**, 219–245. https://doi.org/10.1590/S0001-37652000000200009.

Giuliani, A., Kamenetsky, V. S., Kendrick, M. A., Phillips, D., Wyatt, B. A. & Maas, R. (2013). Oxide, sulphide and carbonate minerals in a mantle polymict breccia: metasomatism by proto-kimberlite magmas, and relationship to the kimberlite megacrystic suite. *Chemical Geology* **353**, 4–18. https://doi.org/10.1016/j.chemgeo.2012.09.025.

Giuliani, A., Phillips, D., Kamenetsky, V. S., Kendrick, M. A., Wyatt, B. A., Goemann, K. & Hutchinson, G. (2014). Petrogenesis of mantle polymict breccias: insights into mantle processes coeval with kimberlite magmatism. *Journal of Petrology* **55**, 831–858. https://doi.org/10.1093/petrology/egu008.

Giuliani, A., Phillips, D., Kamenetsky, V. S. & Goemann, K. (2016). Constraints on kimberlite ascent mechanisms revealed by phlogopite compositions in kimberlites and mantle xenoliths. *Lithos* **240-243**, 189–201. https://doi.org/10.1016/j.lithos.2015.11.013.

Giuliani, A., Phillips, D., Pearson, D. G., Sarkar, S., Müller, A. A., Weiss, Y., Preston, R., Seller, M. & Spetsius, Z. (2023). Diamond preservation in the lithospheric mantle recorded by olivine in kimberlites. *Nature Communications* **14**, 6999. https://doi.org/10.1038/s41467-023-42888-x.

Green, D. H. (2015). Experimental petrology of peridotites, including effects of water and carbon on melting in the Earth's upper mantle. *Physics and Chemistry of Minerals* **42**, 95–122. https://doi.org/10.1007/s00269-014-0729-2.

Grégoire, M., Bell, D. R. & le Roex, A. P. (2002). Trace element geochemistry of phlogopite-rich mafic mantle xenoliths: their classification and their relationship to phlogopite-bearing peridotites and kimberlites revisited. *Contributions to Mineralogy and Petrology* **142**, 603–625. https://doi.org/10.1007/s00410-001-0315-8.

Grégoire, M., Rabinowicz, M. & Janse, A. J. A. (2006). Mantle mush compaction: a key to understand the mechanisms of concentration of kimberlite melts and initiation of swarms of kimberlite dykes. *Journal of Petrology* **47**(3), 631–646. https://doi.org/10.1093/petrology/egi090.

Griffin, W. L., Shee, S. R., Ryan, C. G., Win, T. T. & Wyatt, B. A. (1999). Harzburgite to lherzolite and back again: metasomatic processes in ultramafic xenoliths from the Wesselton kimberlite, Kimberley, South Africa. *Contributions to Mineralogy and Petrology* **134**, 232–250. https://doi.org/10.1007/s004100050481.

Grütter, H. S. (2009). Pyroxene xenocryst geotherms: techniques and application. *Lithos* **112**, 1167–1178. https://doi.org/10.1016/j.lithos.2009.03.023.

Grütter, H. S., Gurney, J. J., Menzies, A. H. & Winter, F. (2004). An updated classification scheme for mantle-derived garnet, for use by diamond explorers. *Lithos* **77**, 841–857. https://doi.org/10.1016/j.lithos.2004.04.012.

Guarino, V., Wu, F.-Y., Lustrino, M., Melluso, L., Brotzu, P., Gomes, C., De, B., Ruberti, E., Tassinari, C. C. G. & Svisero, D. P. (2013). U–Pb ages, Sr–Nd- isotope geochemistry, and petrogenesis of kimberlites, kamafugites and phlogopite-picrites of the alto Paranaíba Igneous Province, Brazil. *Chemical Geology* **353**, 65–82. https://doi.org/10.1016/j.chemgeo.2012.06.016.

Guo, P., Ionov, D. A., Xu, W.-L., Wang, C.-G. & Luan, J.-P. (2020). Mantle and recycled oceanic crustal components in mantle xenoliths from northeastern China and their mantle sources. *Journal of Geophysical Research: Solid Earth* **125**, e2019JB018232. https://doi.org/10.1029/2019JB018232.

Hart, S. R., Hauri, E. H., Oschmann, L. A. & Whitehead, J. A. (1992). Mantle plumes and entrainment: isotopic evidence. *Science* **256**, 517–520. https://doi.org/10.1126/science.256.5056.517.

Harte, B. (1977). Rock nomenclature with particular relation to deformation and recrystallization textures in olivine-bearing xenoliths. *Journal of Geology* **85**, 279–288. https://doi.org/10.1086/628299.

Hasterok, D. & Chapman, D. S. (2011). Heat production and geotherms for the continental lithosphere. *Earth and Planetary Science Letters* **307**, 59–70. https://doi.org/10.1016/j.epsl.2011.04.034.

Henjes-Kunst, F. & Altherr, R. (1992). Metamorphic petrology of xenoliths from Kenya and Northern Tanzania and implications for geotherms and lithospheric structures. *Journal of Petrology* **33**(5), 1125–1156. https://doi.org/10.1093/petrology/33.5.1125.

Hunt, L., Stachel, T., Morton, R., Grutter, H. & Creaser, R. A. (2009). The Carolina kimberlite, Brazil—insights into an unconventional diamond deposit. *Lithos* **112**, 843–851. https://doi.org/10.1016/j.lithos.2009.04.018.

Ionov, D. A., Bodinier, J.-L., Mukasa, S. B. & Zanetti, A. (2002). Mechanisms and sources of mantle metasomatism: major and trace element compositions of peridotite xenoliths from Spitsbergen in the context of numerical modelling. *Journal of Petrology* **43**(12), 2219–2259. https://doi.org/10.1093/petrology/43.12.2219.

Ionov, D. A., Doucet, L. S. & Ashchepkov, I. V. (2010). Composition of the lithospheric mantle in the Siberian Craton: new constraints from fresh peridotites in the Udachnaya-East kimberlite. *Journal of Petrology* **51**(11), 2177–2210. https://doi.org/10.1093/petrology/egq053.

Jacob, D. E. (2004). Nature and origin of eclogite xenoliths from kimberlites. *Lithos* **77**(1–4), 295–316. https://doi.org/10.1016/j.lithos.2004.03.038.

Jochum, K., Nohl, U., Herwig, K., Lammel, E., Stoll, B. & Hofmann, A. W. (2005). GeoReM: a new geochemical database for reference materials and isotopic standards. *Geostandards and Geoanalytical Research* **29**(3), 333–338. https://doi.org/10.1111/j.1751-908X.2005.tb00904.x.

Kaeser, B., Kalt, A. & Pettke, T. (2006). Evolution of the lithospheric mantle beneath the Marsabit Volcanic Field (Northern Kenya): constraints from textural, P–T and geochemical studies on xenoliths. *Journal of Petrology* **47**(11), 2149–2184. https://doi.org/10.1093/petrology/egl040.

Kargin, A. V., Sazonova, L. V., Nosova, A. A. & Tretyachenko, V. V. (2016). Composition of garnet and clinopyroxene in peridotite xenoliths from the Grib kimberlite pipe, Arkhangelsk diamond province, Russia: evidence for mantle metasomatism. Associated with kimberlite melts Grib pipe. *Lithos* **262**, 442–455. https://doi.org/10.1016/j.lithos.2016.07.015.

Kargin, A. V., Sazonova, L. V., Nosova, A. A., Pervov, V. A., Minevrina, E. V., Khvostikov, V. A. & Burmii, Z. P. (2017). Sheared peridotite xenolith from the V. Grib kimberlite pipe, Arkhangelsk Diamond Province, Russia: texture, composition, and origin. *Geoscience Frontiers* **8**, 653–669.

Kargin, A. V., Sazonova, L. V., Nosova, A. A., Lebedeva, N. M., Kostitsyn, Y. A., Kovalchuk, E. V., Tretyachenko, V. V. & Tikhomirova, Y. S. (2019). Phlogopite in mantle xenoliths and kimberlite from the Grib pipe, Arkhangelsk, province, Russia: evidence for

multi-stage mantle metasomatism and origin of phlogopite in kimberlite. *Geoscience Frontiers*. **10**, 1941–1959. https://doi.org/10.1016/j.gsf.2018.12.006.

Kelemen, P. B., Dick, H. J. B. & Quick, J. E. (1992). Formation of harzburgite by pervasive melt-rock reaction in the upper mantle. *Nature* **358**, 635–641. https://doi.org/10.1038/358635a0.

Kennedy, L. A., Russell, J. K. & Kopylova, M. G. (2002). Mantle shear zones revisited: the connection between the cratons and mantle dynamics. *Geology* **30**, 419–422. https://doi.org/10.1130/0091-7613(2002)030<0419:MSZRTC>2.0.CO;2.

King, S. D. & Anderson, D. L. (1998). Edge-driven convection. *Earth and Planetary Science Letters* **160**, 289–296. https://doi.org/10.1016/S0012-821X(98)00089-2.

King, S. D. & Ritsema, J. (2000). African hot-spot volcanism: small-scale convection in the upper mantle beneath cratons. *Science* **290**, 1137–1140. https://doi.org/10.1126/science.290.5494.1137.

Konzett, J., Armstrong, R. A. & Günther, D. (2000). Modal metasomatism in the Kaapvaal craton lithosphere: constraints on timing and genesis from U-Pb zircon dating of metasomatized peridotites and MARID-type xenoliths. *Contributions to Mineralogy and Petrology* **139**, 704–719. https://doi.org/10.1007/s004100000160.

Konzett, J., Wirth, R., Hauzenberger, C. & Whitehouse, M. (2013). Two episodes of fluid migration in the Kaapvaal craton lithospheric mantle associated with cretaceous kimberlite activity: evidence from a harzburgite containing a unique assemblage of metasomatic zirconium-phases. *Lithos* **182-183**, 165–184. https://doi.org/10.1016/j.lithos.2013.10.005.

Koornneef, J. M., Davies, G. R., Döpp, S. P., Vukmanovic, Z., Nikogosian, I. K. & Mason, P. R. D. (2009). Nature and timing of multiple metasomatic events in the sub-cratonic lithosphere beneath Labait. *Tanzania. Lithos* **112**(2), 896–912. https://doi.org/10.1016/j.lithos.2009.04.039.

Kopylova, M. G., Tso, E., Ma, F., Liu, J. & Pearson, D. G. (2019). The Metasomatized mantle beneath the North Atlantic craton: insights from peridotite xenoliths of the Chidliak Kimberlite Province (NE Canada). *Journal of Petrology* **60**(10), 1991–2024. https://doi.org/10.1093/petrology/egz061.

Krogh, E. J. (1988). The garnet-clinopyroxene Fe–Mg–geothermometer—a reinterpretation of existing experimental data. *Contributions to Mineralogy and Petrology* **99**, 44–48. https://doi.org/10.1007/BF00399364.

Lee, C. T. A., Cheng, X. & Horodyskyj, U. (2006). The development and refinement of continental arcs by primary basaltic magmatism, garnet pyroxenite accumulation, basaltic recharge and delamination: insights from the Sierra Nevada, California. *Contributions to Mineralogy and Petrology* **151**, 222–242. https://doi.org/10.1007/s00410-005-0056-1.

Liao, J., Wang, Q., Gerya, T. & Ballmer, M. D. (2017). Modeling craton destruction by hydration-induced weakening of the upper mantle. *Journal of Geophysical Research: Solid Earth* **122**, 7449–7466. https://doi.org/10.1002/2017JB014157.

Lin, A.-B., Aulbach, S., Zheng, J.-P., Cai, R., Liu, J., Xiong, Q. & Pan, S.-K. (2022). Lithospheric mantle provinces and crust-mantle decoupling beneath northeastern China: insights from peridotite xenoliths. *Geological Society of America Bulletin* **135**(3–4), 990–1008. https://doi.org/10.1130/B36338.1.

Liu, M. & Li, Z. (2018). Dynamics of thinning and destruction of the continental cratonic lithosphere: numerical modeling. *Science China Earth Sciences* **61**, 823–852. https://doi.org/10.1007/s11430-017-9184-x.

Liu, J., Cai, R., Pearson, D. G. & Scott, J. M. (2019). Thinning and destruction of the lithospheric mantle root beneath the North China Craton: a review. *Earth-Science Reviews* **196**, 102873. https://doi.org/10.1016/j.earscirev.2019.05.017.

Liu, J., Pearson, D. G., Wang, L. H., Mather, K. A., Kjarsgaard, B. A., Schaeffer, A. J., Irvine, G. J., Kopylova, M. G. & Armstrong, J. P. (2021). Plume-driven recratonization of deep continental lithospheric mantle. *Nature* **592**, 732–736. https://doi.org/10.1038/s41586-021-03395-5.

Lu, J., Griffin, W. L., Tilhac, R., Xiong, Q., Zheng, J. & O'Reilly, S. Y. (2018). Tracking deep lithospheric events with garnet-websterite xenoliths from Southeastern Australia. *Journal of Petrology* **59**(5), 901–930. https://doi.org/10.1093/petrology/egy049.

Menzies, M., Rogers, N., Tindle, A. & Hawkesworth, C. (1987) Metasomatic and Enrichment Processes in the Lithospheric Peridotites, and Effect of Asthenosphere-Lithosphere Interaction. In: Menzies M. A. & Hawkesworth C. J. (eds) *Mantle Metasomatism*. London: Academic Press, pp.313–361.

Mercier, J. C. C. (1980). Single-pyroxene thermobarometry. *Tectonophysics* **70**, 1–37. https://doi.org/10.1016/0040-1951(80)90019-0.

Mitchell, R. H. (1995) *Kimberlites, Orangeites, and Related Rocks*. Boston, MA: Springer, p.410.

Müntener, O., Kelemen, P. B. & Grove, T. L. (2001). The role of H_2O during crystallization of primitive arc magmas under uppermost mantle conditions and genesis of igneous pyroxenites: an experimental study. *Contributions to Mineralogy and Petrology* **141**, 643–658. https://doi.org/10.1007/s004100100266.

Nannini, F. (2011) *Petrografia e química mineral de xenólitos mantélicos da intrusão kimberlítica Indaiá, Monte Carmelo,* MGMaster thesis. Brazil: Universidade de São Paulo, p.99 in Portuguese.

Nannini, F. (2016) *Geologia e petrologia de xenólitos mantélicos da Província Ígnea do Alto Paranaíba*PhD thesis. Brazil: Universidade de São Paulo, p.298 in Portuguese.

Neves, S. P. (2021). Comparative geological evolution of the Borborema Province and São Francisco Craton (eastern Brazil): decratonization and crustal reworking during West Gondwana assembly and implications for paleogeographic reconstructions. *Precambrian Research* **355**, 106119. https://doi.org/10.1016/j.precamres.2021.106119.

Nickel, K. G. & Green, D. H. (1985). Empirical geothermobarometry for garnet peridotites and implications for the nature of the lithosphere, kimberlites and diamonds. *Earth and Planetary Science Letters* **73**, 158–170. https://doi.org/10.1016/0012-821X(85)90043-3.

Nimis, P. & Taylor, W. R. (2000). Single clinopyroxene thermobarometry for garnet peridotites. Part I. Calibration and testing of a Cr-in-Cpx barometer and an enstatite-in-Cpx thermometer. *Contributions to Mineralogy and Petrology* **139**, 541–554. https://doi.org/10.1007/S004100000156.

Nimis, P., Preston, R., Perritt, S. H. & Chinn, I. L. (2020). Diamond's depth distribution systematics. *Lithos* **376-377**, 105729. https://doi.org/10.1016/j.lithos.2020.105729.

Nixon, P. H., Rogers, N. W., Gibson, I. L. & Grey, A. (1981). Depleted and fertile mantle xenoliths from southern African kimberlites. *Annual Review of Earth and Planetary Sciences* **9**, 285–309. https://doi.org/10.1146/annurev.ea.09.050181.001441.

Nowell, G. M., Pearson, D. G., Bell, D. R., Carlson, R. W., Smith, C. B., Kempton, P. D. & Noble, S. R. (2004). Hf isotope systematics of kimberlites and their Megacrysts: new constraints on their source regions. *Journal of Petrology* **45**(8), 1583–1612. https://doi.org/10.1093/petrology/egh024.

O'Reilly, S. Y. & Griffin, W. L. (2010). The continental lithosphere–asthenoshpere boundary: can we sample it? *Lithos* **120**, 1–13. https://doi.org/10.1016/j.lithos.2010.03.016.

Obata, M. & Ozawa, K. (2011). Topotaxic relationships between spinel and pyroxene in kelyphite after garnet in mantle-derived peridotites and their implications to reaction mechanism and kinetics. *Mineralogy and Petrology* **101**, 217–224. https://doi.org/10.1007/s00710-011-0145-y.

Pereira, R. S. & Fuck, R. A. (2005). Archean nucleii and the distribution of kimberlite and related rocks in the São Francisco Craton, Brazil. *Revista Brasileira de Geociencias* **35**, 93–104. https://doi.org/10.25249/0375-7536.200535S493104.

Pinto, L. G. R., Pádua, M. B., Ussami, N., Vitorello, I., Padilha, A. L. & Braitenberg, C. (2010). Magnetotelluric deep soundings, gravity and geoid in the South São Francisco craton: geophysical indicators of cratonic lithosphere rejuvenation and crustal underplating. *Earth and Planetary Science Letters* **297**, 423–434. https://doi.org/10.1016/j.epsl.2010.06.044.

Puziewicz, J., Aulbach, S., Kaczmarek, M.-A., Ntaflos, T., Gerdes, A., Mazurek, H., Kukuła, A., Matusiak-Małek, M., Tedonkenfack, S. S. T. & Ziobro-Mikrut, M. (2023). The origin and evolution of DMM-like lithospheric mantle beneath continents: mantle xenoliths from the Oku Volcanic Group in the Cameroon Volcanic Line, West Africa. *Journal of Petrology* **64**(7), 1–25. https://doi.org/10.1093/petrology/egad049.

Raczek, I., Peter Jochum, K. & Hofmann, A. W. (2003). Neodymium and strontium isotope data for USGS reference materials BCR-1, BCR-2, BHV O-1, BHVO-2, AGV-1, AGV-2, GSP-1, GSP-2 and eight MPI-DING reference glasses. *Geostandards Newsletter* **27**(2), 173–179. https://doi.org/10.1111/j.1751-908X.2003.tb00644.x.

Rader, E., Emry, E., Schmerr, N., Frost, D., Cheng, C., Menard, J., Yu, C.-Q. & Geist, D. (2015). Characterization and petrological constraints of the midlithospheric discontinuity. *Geochemistry, Geophysics, Geosystems* **16**(10), 3484–3504. https://doi.org/10.1002/2015GC005943.

Rapp, R. P., Shimizu, N., Norman, M. D. & Applegate, G. S. (1999). Reaction between slab-derived melts and peridotite in the mantle wedge: experimental constraints at 3.8 GPa. *Chemical Geology* **160**, 335–356. https://doi.org/10.1016/S0009-2541(99)00106-0.

Read, G., Grutter, H., Winter, S., Luckman, N., Gaunt, F. & Thomsen, F. (2004). Stratigraphic relations, kimberlite emplacement and lithospheric thermal evolution, Quiricó Basin, Minas Gerais State. *Brazil. Lithos* **77**(1–4), 803–818. https://doi.org/10.1016/j.lithos.2004.04.011.

Rehfeldt, T., Foley, S. F., Jacob, D. E., Carlson, R. W. & Lowry, D. (2008). Contrasting types of metasomatism in dunite, wehrlite and websterite xenoliths from Kimberley, South Africa. *Geochimica et Cosmochimica Acta* **72**(23), 5722–5756. https://doi.org/10.1016/j.gca.2008.08.020.

Rocha, M. P., Azevedo, P. A., Assumpção, M., Pedrosa-Soares, A. C., Fuck, R. & Von Huelsen, M. G. (2019a). Delimiting the Neoproterozoic São Francisco Paleocontinental Block with P-wave traveltime tomography. *Geophysical Journal International* **219**, 633–644. https://doi.org/10.1093/gji/ggz323.

Rocha, M. P., Assumpção, M., Affonso, G. M. P. C., Azevedo, P. A. & Bianchi, M. (2019b). Teleseismic P-wave tomography beneath the Pantanal, Paraná and Chaco-Paraná Basins, SE South America: delimiting lithospheric blocks of the SW Gondwana Assemblage. *Journal of Geophysical Research: Solid Earth* **124**, 7120–7137. https://doi.org/10.1029/2018JB016807.

Rodrigues, R. A. F., Gervasoni, F., Jalowitzki, T., Bussweiler, Y., Berndt, J., Botelho, N. F., Queiroga, G., de Castro, M. P., da Silva, S. W., Ciriaco, B. A., de Oliveira, I. L. & Klemme, S. (2023). Mantle metasomatism and refertilization beneath the SW margin of the São Francisco craton, Brazil. *Lithos* **448-449**, 107164. https://doi.org/10.1016/j.lithos.2023.107164.

Roduit, N. (2007). *JMicroVision: un logiciel d'analyse d'images p trographiques polyvalent*. PhD thesis. University of Genève, Switzerland, 116. https://doi.org/10.13097/archive-ouverte/unige:468.

le Roex, A., Tinguely, C. & Gregoire, M. (2020). Eclogite and garnet pyroxenite xenoliths from kimberlites emplaced along the southern margin of the Kaapvaal Craton, Southern Africa: mantle or lower crustal fragments? *Journal of Petrology* **61**, 1–32. https://doi.org/10.1093/petrology/egaa040.

Rudnick, R. L., McDonough, W. F. & Orpin, A. (1994) Northern Tanzanian peridotite xenoliths: a comparison with Kaapvaal peridotites and inferences on metasomatic interactions. In: Meyer H. O. A. & Leonardos O. H. (eds) *Proceedings of the 5th International Kimberlite Conference, vol. 1*. Rio de Janeiro: Companhia de Pesquisa de RecursosMinerais (CPRM), pp.336–353.

Sen, C. & Dunn, T. (1995). Experimental modal metasomatism of a spinel lherzolite and the production of amphibole-bearing peridotite. *Contributions to Mineralogy and Petrology* **119**, 422–432. https://doi.org/10.1007/BF00286939.

Sgarbi, P. B., Heaman, L. M. & Gaspar, J. C. (2004). U–Pb perovskite ages for Brazilian kamafugitic rocks: further support for a temporal link to a mantle plume hotspot track. *Journal of South American Earth Sciences* **16**(8), 715–724. https://doi.org/10.1016/j.jsames.2003.12.005.

Sharygin, I. S., Sobolev, K. A. & Golovin, A. V. (2023). Kelyphite around garnet in unaltered lherzolite xenolith from the Udachnaya pipe (Siberian Craton): formation exclusively via interaction with kimberlite melt. *Journal of Asian Earth Sciences* **256**, 105821. https://doi.org/10.1016/j.jseaes.2023.105821.

Shu, Q., Brey, G. P., Gerdes, A. & Hoefer, H. E. (2014). Mantle eclogites and garnet pyroxenites—the meaning of two-point isochrons, Sm–Nd and Lu–Hf closure temperatures and the cooling of the subcratonic mantle. *Earth and Planetary Science Letters* **389**, 143–154. https://doi.org/10.1016/j.epsl.2013.12.028.

Streckeisen, A. (1976). To each plutonic rock its proper name. *Earth-Science Reviews* **12**, 1–33. https://doi.org/10.1016/0012-8252(76)90052-0.

Sudholz, Z. J., Yaxley, G. M., Jaques, A. L. & Brey, G. P. (2021). Experimental recalibration of the Cr-in-clinopyroxene geobarometer: improved precision and reliability above 4.5 GPa. *Contributions to Mineralogy and Petrology* **176**(11), 1–20. https://doi.org/10.1007/s00410-020-01768-z.

Sudholz, Z. J., Green, D. H., Yaxley, G. M. & Jaques, A. L. (2022). Mantle geothermometry: experimental evaluation and recalibration of Fe–Mg geothermometers for garnet-clinopyroxene and garnet-orthopyroxene in peridotite, pyroxenite and eclogite systems. *Contributions to Mineralogy and Petrology* **177**, 77. https://doi.org/10.1007/s00410-022-01944-3.

Sun, C. & Liang, Y. (2015). A REE-in-garnet–clinopyroxene thermobarometer for eclogites, granulites and garnet peridotites. *Chemical Geology* **393-394**, 79–92. https://doi.org/10.1016/j.chemgeo.2014.11.014.

Sun, S. & McDonough, W. F. (1989). Chemical and isotopic systematics of oceanic basalts: implications for mantle composition and processes. *Geological Society, London, Special Publication* **42**, 313–345. https://doi.org/10.1144/GSL.SP.1989.042.01.19.

Tang, Y. J., Zhang, H. F., Ying, J. F. & Su, B. X. (2013). Widespread refertilization of cratonic and circum-cratonic lithospheric mantle. *Earth-Science Reviews* **118**, 45–68. https://doi.org/10.1016/j.earscirev.2013.01.004.

Tappe, S., Foley, S. F., Stracke, A., Romer, R. L., Kjarsgaard, B. A., Heaman, L. M. & Joyce, N. (2007). Craton reactivation on the Labrador Sea margins: $^{40}Ar/^{39}Ar$ age and Sr–Nd–Hf–Pb isotope

constraints from alkaline and carbonatite intrusives. *Earth and Planetary Science Letters* **256**, 433–454. https://doi.org/10.1016/j.epsl.2007.01.036.

Tappe, S., Romer, R. L., Stracke, A., Steenfelt, A., Smart, K. A., Muehlenbachs, K. & Torsvik, T. H. (2017). Sources and mobility of carbonate melts beneath cratons, with implications for deep carbon cycling, metasomatism and rift initiation. *Earth and Planetary Science Letters* **466**, 152–167. https://doi.org/10.1016/j.epsl.2017.03.011.

Tappe, S., Budde, G., Stracke, A., Wilson, A. & Kleine, T. (2020). The tungsten-182 record of kimberlites above the African superplume: exploring links to the core-mantle boundary. *Earth and Planetary Science Letters* **547**, 116473. https://doi.org/10.1016/j.epsl.2020.116473.

Tappe, S., Massuyeau, M., Smart, K. A., Woodland, A. B., Gussone, N., Milne, S. & Stracke, A. (2021). Sheared peridotite and megacryst formation beneath the Kaapvaal craton: a snapshot of tectonomagmatic processes across the lithosphere–asthenosphere transition. *Journal of Petrology* **62**(8), 1–39. https://doi.org/10.1093/petrology/egab046.

Tappe, S., Shaikh, A. M., Wilson, A. H. & Stracke, A. (2022). Evolution of ultrapotassic volcanism on the Kaapvaal craton: deepening the orangeite versus lamproite debate. *Geological Society, London, Special Publications* **513**, 17–44. https://doi.org/10.1144/SP513-2021-84.

Tappe, S., Ngwenya, N., Stracke, A., Romer, J. G. & Schmitt, A. K. (2023). Plume–lithosphere interactions and LIP-triggered climate crises constrained by the origin of Karoo lamproites. *Geochimica et Cosmochimica Acta* **350**, 87–105. https://doi.org/10.1016/j.gca.2023.04.008.

Taylor, W. R. (1998). An experimental test of some geothermometer and geobarometer formulations for upper mantle peridotites with application to the thermobarometry of fertile lherzolite and garnet websterite. *Neues Jahrbuch fur Mineralogie, Abhandlungen* **172**, 381–408. https://doi.org/10.1127/njma/172/1998/381.

Thirlwall, M. F. (1991). Long-term reproducibility of multicollector Sr and Nd isotope ratio analysis. *Chemical Geology: Isotope Geoscience Section* **94**(2), 85–104. https://doi.org/10.1016/0168-9622(91)90002-E.

Thomaz, L. V. (2009) *Estudo petrográfico e química mineral da intrusão kimberlítica Régis, no oeste de Minas Gerais*Master thesis. Brazil: Universidade de São Paulo, p.143 (in Portuguese).

Valeriano, C. M., Pimentel, M. M., Heilbron, M., Almeida, J. C. H. & Trouw, R. A. J. (2008). Tectonic evolution of the Brasília Belt, Central Brazil, and early assembly of Gondwana. *Geological Society, London, Special Publications* **294**, 197–210. https://doi.org/10.1144/SP294.11.

Van Orman, J. A., Grove, T. L. & Shimizu, N. (2001). Rare earth element diffusion in diopside: influence of temperature, pressure, and ionic radius, and an elastic model for diffusion in silicates. *Contributions to Mineralogy and Petrology* **141**, 687–703. https://doi.org/10.1007/s004100100269.

Van Orman, J. A., Grove, T. L., Shimizu, N. & Layne, G. D. (2002). Rare earth element diffusion in a natural pyrope single crystal at 2.8 GPa. *Contributions to Mineralogy and Petrology* **142**, 416–424. https://doi.org/10.1007/s004100100304.

Viljoen, K. S., Schulze, D. J. & Quadling, A. G. (2005). Contrasting Group I and Group II eclogite xenolith petrogenesis: petrological, trace element and isotopic evidence from eclogite, garnet-websterite and alkremite xenoliths in the Kaalvallei kimberlite, South Africa. *Journal of Petrology* **46**(10), 2059–2090. https://doi.org/10.1093/petrology/egi047.

Viljoen, F., Dobbe, R. & Smit, B. (2009). Geochemical processes in peridotite xenoliths from the premier diamond mine, South Africa: evidence for the depletion and refertilisation of subcratonic lithosphere. *Lithos* **112**, 1133–1142. https://doi.org/10.1016/j.lithos.2009.05.004.

White, W. M. & Klein, E. M. (2014) Composition of the Oceanic Crust. In: Holland H. D. & Turekian K. K. (eds) *Treatise on Geochemistry (Second Edition)*, 4. Oxford: Elsevier, pp.457–496.

Woodhead, J., Hergt, J., Giuliani, A., Maas, R., Phillips, D., Pearson, D. G. & Nowell, G. (2019). Kimberlites reveal 2.5-billion-year evolution of a deep, isolated mantle reservoir. *Nature* **573**(7775), 578–581. https://doi.org/10.1038/s41586-019-1574-8.

Wyatt, B. A., Baumgartner, M., Anckar, E. & Grutter, H. (2004). Compositional classification of "kimberlitic" and "non-kimberlitic" ilmenite. *Lithos* **77**(1–4), 819–840. https://doi.org/10.1016/j.lithos.2004.04.025.

Xiong, Q., Zheng, J.-P., Griffin, W. L., O'Reilly, S. Y. & Pearson, N. J. (2014). Pyroxenite dykes in orogenic peridotite from North Qaidam (NE Tibet, China) track metasomatism and segregation in the mantle wedge. *Journal of Petrology* **55**(12), 2347–2376. https://doi.org/10.1093/petrology/egu059.